69-8596

FRIDAY, Jr., Elbert Walter, 1939-
BEHAVIOR OF DISCRETE CONVECTIVE ELEMENTS IN A ROTATING FLUID.

The University of Oklahoma, Ph.D., 1969
Physics, meteorology

University Microfilms, Inc., Ann Arbor, Michigan

THE UNIVERSITY OF OKLAHOMA

GRADUATE COLLEGE

BEHAVIOR OF DISCRETE CONVECTIVE ELEMENTS

IN A ROTATING FLUID

A DISSERTATION

SUBMITTED TO THE GRADUATE FACULTY

in partial fulfillment of the requirements for the

degree of

DOCTOR OF PHILOSOPHY

BY

ELBERT WALTER FRIDAY, JR.

Norman, Oklahoma

1969

BEHAVIOR OF DISCRETE CONVECTIVE ELEMENTS

IN A ROTATING FLUID

A DISSERTATION

APPROVED FOR THE DEPARTMENT OF METEOROLOGY

BY

[illegible]

Arthur Bernhart

J. F. Harp

W J Saucier

Eugene M. Wilkins

ACKNOWLEDGEMENTS

I wish to express appreciation to the United States Air Force, the Air Force Institute of Technology for this assignment at the University of Oklahoma. I will ever be indebted to Dr. Yoshikazu Sasaki, Professor of Meteorology, whose assistance and guidance were instrumental to the completion of my course of study and the research represented by this paper. Appreciation is also extended to Dr. Eugene M. Wilkins, Adjunct Associate Professor of Meteorology and of Ling-Temco-Vaught, Dallas, Texas, for his valuable aid, discussion, and criticisms of this research. The assistance of Mrs. Marcia Rucker in typing this manuscript is greatly appreciated.

I am also indeed thankful to my wife, Karen, who not only aided materially in much of the data handling associated with this work, but also provided patience, understanding and encouragement without which this work could not have been accomplished.

This dissertation was done in connection with graduate study at the University of Oklahoma and was sponsored in part by the Atmospheric Sciences Section, National Science Foundation under research grant GA-1328.

TABLE OF CONTENTS

TABLE OF CONTENTS (cont'd)

LIST OF TABLES

LIST OF ILLUSTRATIONS

BEHAVIOR OF DISCRETE CONVECTIVE ELEMENTS IN A ROTATING FLUID

CHAPTER I

INTRODUCTION

During the past few years, time lapse films of radar observations of severe storms have demonstrated that many of the severe storms are rotating about some vertical axis. (For example Fujita, 1966). Such a rotational motion could provide an angular momentum source for the formation of a tornado vortex, but a more basic question should be answered relative to the storm's angular velocity. This question concerns the behavior of a convective element which is growing in the presence of a rotating field. In essence, does the presence of a rotational field enhance or suppress the convection?

Because of all the unknowns in the structure and description of a severe thunderstorm, it would be impossible to study the entire thunderstorm as it grows in a rotational field. Instead, a look at the essence of convective motion is indicated. Ludlum (1963), for example, has assumed as a tentative thunderstorm model a process involving a succession of individual convective elements growing in the updraft of a cumulonimbus cloud. Two forms of these individual convective elements considered in the past are mathemetical idealizations of a real situation, and yet still represent the physical essence of the real situation. The first, called a thermal, is idealized as that convective element which has its origin as an instantaneous point source of buoyancy. The thermal then grows and rises as an isolated bubble of buoyant material. The second idealized convective element is called a plume. It is a steady state process which is formed by a continuous point source of buoyant material. Figure 1 illustrates the differences between the plume and the thermal in this idealized fashion, and denotes some of the pertinent physical parameters of height, radius, etc. used to characterize these convective elements. The question posed in the introductory paragraph can now be restated so as to apply to behavior of the idealized convective elements, the plume and the thermal, when they are growing in a rotating field.

The growth of isolated thermals in nonrotating media has received considerable attention in the past few years, both experimentally and theoretically. Theoretical investigations were made by Batchelor (1954) in which the study of isolated convective elements relied heavily on dimensional analysis. This work was followed by the investigations of Morton, Taylor, and Turner (1956). They developed a set of simultaneous ordinary differential equations which represented the conservation of volume, momentum, and density deficit in isolated convective motion. Two separate sets of equations were developed. Characteristics of plumes were given as functions of height. The parameters representing thermals were described as functions of time.

Laboratory experiments have been conducted on thermal growth by injecting a light fluid into a tank of heavier fluid, or by dropping heavier masses from the upper surface of a lighter fluid. The growth of the **thermals** may then be observed photographically. Scorer (1957) used experimental data obtained from such photographs to determine the proportionality constants in the theoretical expressions derived by dimensional analysis. Woodward (1959) used such photographic analysis to study the motion field in and around the thermal element. This study was made using a suspension of discrete particles with a low terminal velocity. Richards (1961), with a heavy thermal in a light fluid, studied not only the motions of the descending thermal in that fluid but also its penetration through the interface between that fluid and a fluid of intermediate density over which it had been layered.

Another successful experimental approach developed by Turner (1963) has been the release of CO_2 gas from carbonated water by the injection of acid, charged with suitable nuclei for the formation of bubbles. In this way, myriads of tiny bubbles form a buoyant cloud in the carbonated water. By careful control of the procedures, clouds of increasing buoyancy may be released. Turner and Lilly (1963) developed and studied vortices in rotating tanks of carbonated water, and with the aid of dye tracers, were able to observe the motions in and around the vortices. Clouds in which a buoyancy-producing chemical reaction continues to take place is somewhat analogous to cumulus coulds in which the buoyancy production is caused by the release of the latent heat of condensing water. For the cases of constant buoyancy, the convective process is analogous to an adiabatic system. The adiabatic case was also represented in the experimental work of Turner and Lilly (1963) by bubbling air into the top of a tank of a rotating fluid, the buoyant plume being formed by the air bubbles rising through the water.

Many laboratory experiments have been conducted to study the vortex formation caused by the concentration of angular momentum in a rotating tank of fluid. Long (1956, 1958, 1961) has dealt both theoretically and experimentally with vortices formed and driven by a steady sink in a rotating fluid. In these experiments fluid was removed from the center of the rotating tank, resulting in a steady state vortex. Morton (1963) has simulated more closely the atmospheric conditions by injecting steadily a buoyant fluid into the center of a rotating tank. Turner and Lilly (1963) have created vortices by causing CO_2 bubbles to be released at the center of rotating tanks of carbonated water. The CO_2 bubbles released cause vertical motions whose compensating lateral convergence concentrates angular momentum, and creates the vortex if the tank is rotating at sufficient speed. They found that even when the bubbling was confined to the upper layers of fluid, a vortex still formed which extended itself the full length of the tank.

The most extensive experimental analysis of rotationally influenced thermal convection has been performed by McCarthy (1967), McIntyre (1967) and Wilkins et al (1967). These experiments were performed at the University of Oklahoma and are summarized and further analyzed by Sasaki, Friday and Wilkins (1968).

McIntyre studied the influence of the rotational field upon instantaneous thermals which were adiabatic in nature. The thermals were formed by injecting a small volume of detergent foam into a tank of water which was in solid rotation. These thermals were photographed by a motion picture camera mounted so as to rotate with the tank, and the resultant photographic record was analyzed to determine the time history of the various thermal properties. McIntyre's experiments indicated a suppression of the growth rate of the thermal by the rotational field. The amount of suppression increased with increasing rotation rate. The suppression of the growth was manifest in five parameters which were analyzed for the cloud. The rotational field resulted in a decrease in the equivalent radius, b, the height, h, the vertical velocity, w, of the cloud top and the entrainment rate, E, of the cloud. The parameters b and h are defined in Figure 1. The vertical velocity is given by

$$w = \frac{\delta z}{\delta t} \qquad (1)$$

which was evaluated by finite difference analysis of the motion picture record. The entrainment rate was defined as the time rate of change of the volume, V, of the thermal expressed as a percentage:

$$E = \frac{1}{V}\frac{\delta V}{\delta t} \qquad (2)$$

This parameter was likewise evaluated from the photographic record. The fifth parameter evaluated, the density deficit acceleration, Δ, was seen to increase in the presence of a rotational field. This term is defined by

$$\Delta = g\,\frac{(\rho_o - \rho)}{\rho_1} \qquad (3)$$

where g is the acceleration of gravity; ρ, ρ_o, and ρ_1, are the cloud density, the environmental density, and a standard reference density respectively. The decrease in E obviously results in an increase of Δ, since as the convective motion is suppressed, the entrainment process is reduced and the buoyant cloud material undergoes a lesser degree of dilution by the more dense environmental air. The increase in thermal volume by the entrainment of environmental fluid into a rising thermal has been found by Morton, Taylor, and Turner (1956) to have the general form

$$\frac{dV}{dt} = \alpha \ w \ (4\pi b^2) \tag{4}$$

where $4\pi b^2$ represents the surface area of the rising thermal and w is its vertical velocity. The proportionality constant α is termed the entrainment coefficient and is assumed to be a constant with time. Thus, the rate of change of volume should decrease with decreasing w and b as in McIntyre's studies.

McIntyre further observed that the shape of the thermal under rotating and nonrotating conditions was different. A cloud rising in a rotating field takes on a more nearly cylindrical shape than one in a nonrotating field. The visible radius of the rotating cloud is smaller than that of a nonrotating cloud. This visible radius in the case of a rotating cloud did not increase appreciably after the element had grown for a short period of time. A comparison of the rotating and nonrotating cloud structure is shown in Figure 2. Equation (4), however, when the definition of w is introduced, reduces to

$$b = \alpha h \tag{5}$$

which implies that the radius should grow as the thermal rises. This would imply that (4) could not be used to describe the thermal in a rotating environment. To circumvent this objection, McIntyre defined b to be the equivalent spherical radius for the thermal:

$$b = \left(\frac{3V}{4\pi}\right)^{1/3} \tag{6}$$

or, in other words, the radius the thermal element would have if its volume were considered to be a sphere. This was successful in obtaining a good agreement with the theoretical analysis which will be presented in Chapter II of this paper. Using this notation, a value of 0.21 was obtained for the entrainment coefficient α in both the rotating and non-rotating thermals.

McIntyre further observed that in each rotating thermal experiment a small scale vertical vortex was formed from the base of the cloud extending to the bottom of the tank. The vortex as formed was frequently destroyed when portions of the lower part of the cloud were observed to descend around it.

Using a technique similar to Turner (1963), non-adiabatic thermal elements were analyzed by McCarthy (1967). The experimental tank was filled with partially carbonated water. A small volume of hydrochloric acid solution was injected into the tank. The HCl reduces the solubility of CO_2 in the water and therefore a large number of small CO_2 bubbles are released. This cloud, which now contains CO_2 bubbles and HCl, continues to rise and in doing so entrains carbonated water from the environment. This reacts with the cloud releasing still more CO_2

simulating a process by which the buoyancy is increased as the cloud grows. McCarthy found that rotation of the environment enhanced the convective activity for his non-adiabatic thermal. McCarthy observed an increase in each of the five parameters discussed in reference to the adiabatic thermal. Again, the equivalent spherical radius was used in this analysis of the data, and a value of 0.17 for the entrainment coefficient, α, was observed for the nonrotating case while a value of 0.19 was observed for the rotating case. Here, as in the adiabatic case the value of α can be considered a constant for various rotation rates when an equivalent spherical radius is used in the evaluation.

As in the case of McIntyre's adiabatic experiments, a small scale vertical vortex was produced by each non-adiabatic thermal injected into a rotating tank. The apparent intensity of the vortex increased with increasing rotation, but in all cases the vortex demise appeared to follow the same pattern as for the adiabatic thermals: a downflow of cloud material around the vortex and a divergence pattern which spread the vortex laterally. At higher rotation rates (30 rpm) the vortex would sometimes reform after this occurred, but always in a much weaker state than initially.

Numerical modelling of the growth of convective elements has been conducted by Ogura and Phillips (1962), Ogura (1963), and Lilly (1962, 1964). The results of these numerical experiments agree well with the results of both the theoretical studies based on dimensional analysis and the laboratory experiments. These studies were, however, dealing with fluids which were not rotating. Inman (1966) applied the equations developed by Ogura (1963) to model numerically a buoyant mass rising in a rotating fluid.

The objective of this study is to examine in detail the effect of rotation on the growth of a discrete convective element. Both adiabatic and non-adiabatic convection are studied. Adiabatic in this case is taken to mean that all buoyancy is provided to the convective element at the source. This corresponds to the dry convective processes. Inclusion of a buoyancy production function is important in the study of sustained convection in the atmosphere. Thus, the non-adiabatic case would correspond to moist convective process. Since experimental evidence has been found for both enhancement and suppression of convection, it becomes necessary to explain these results on the basis of theory. Two approaches will be used in this paper. The first, discussed in Chapter II, will consist of the development of a simple physical model which describes the gross features of the convection processes in a rotating medium. This model is unable to describe the vortex structure generated by the rising convective motion and the subsequent demise of the vertical vortex. The second approach is a numerical modelling of the hydrodynamic equations governing the convective motion. The results of this study are observed to agree quite well with the behavior of the experimental models.

CHAPTER II

THEORETICAL STUDIES, CONSERVATION EQUATIONS

The model presented here is not intended to answer all of the questions arising in the study of point source convection. It is instead a simple physical model designed to explain the gross properties of convective growth under the influence of rotation.

Angular Momentum, Energy, and Pressure in Plumes and Thermals

First consider a fluid in solid rotation which is not disturbed by convective motion. In the model, the fluid is considered to be inviscid, consequently, the dissipation of energy by viscous forces will be ignored. The tangential velocity at any distance R from the vertical axis of rotation is thus given by

$$V_\theta = R\Omega \tag{7}$$

where Ω is the angular velocity of the rotating medium. Thus the conservation of angular momentum for a fluid particle displaced from position R to a new position r can be described by

$$v_\theta r = RV_\theta = R^2\Omega \tag{8}$$

Along any streamline in this fluid, the conservation of total energy for this displacement may be written

$$\frac{v_\theta^2 + v_r^2}{2} + \frac{p}{\rho} = \frac{R^2\Omega^2}{2} + \frac{P}{\rho} \tag{9}$$

where the left side of the equation describes the tangential and radial velocities, pressure, and density of the particle located at the new position r, and the right hand side represents the total energy at the original radial position R. In writing (9) in this form it is assumed that the internal energy of the particle does not change, i.e., that there is no temperature change in such a displacement. It should also be noted that this simple relation is applicable only along an individual streamline.

Experiments by Wilkins (1964) indicate that the radial and tangential velocity components differ by only a small constant factor K. This is particularly true in the region of vortex flow where angular momentum is conserved in the radial inflow. Using such a relationship as

$$v_r = Kv_\theta \tag{10}$$

one can combine (8) and (9) and therefore solve for p.

$$\frac{p}{\rho} = \frac{P}{\rho} + \frac{R^2\Omega^2}{2}\left[1 - (1 + K^2)\,\frac{R^2}{r^2}\right] \tag{11}$$

Equation (11) shows that convergence within a rotating fluid will cause a lower pressure to exist within the area of convergence than in the ambient fluid. This pressure reduction vanishes at some limiting value of r beyond which ambient conditions are assumed to hold.

Equation (11) also implies that a 'critical radius' must exist. This critical radius becomes necessary to prevent negative pressures which would otherwise occur if the fluid particle was transported to very small radial distances. The value for the critical radius may be determined from (11) by solving this equation for the value of r when $p = 0$:

$$r_c = R[(1 + K^2) / (1 + 2P/\rho \, R^2\Omega^2)]^{\frac{1}{2}} \tag{12}$$

In the real situation, such a critical radius does not actually occur because of the viscous forces which act to dissipate the energy of the vortex. The condition arises in our simple model because of the neglect of the viscous forces.

It should be noted at this time that two additional physical processes are neglected in the derivation which follows. The neglect of these processes can only be justified by the fact that the simple model presented here agrees remarkably well with the experimental results described by McCarthy (1967) and McIntyre (1967). This would therefore give a strong indication of the importance of these processes relative to those considered in this theory. The two processes which are neglected are:

(1) the turbulent exchange of fluid at the boundary of the convective element, which causes drag due to shearing stress and tangential accelerations caused by the angular momentum transfer; and

(2) the dynamic pressure effects due to the convective motion. This effect is probably negligible unless the fluid undergoes considerable compression.

It is assumed that the mechanism causing the displacement from the original position R to the new location r is the entrainment of the environmental fluid by a convective element rising in the rotating fluid. The average pressure within the boundaries of the convective element can be found by integrating the expression for p as given in (11) from the radius of the thermal element to the critical radius and dividing by the total area contained within these limits. Thus

$$\frac{\bar{p}}{\rho} = \frac{1}{\pi(b^2 - r_c^2)} \int_{r_c}^{b} \frac{p}{\rho} \cdot 2\pi r dr, \tag{13}$$

where b is the radius of the convective element. The density of the fluid is assumed to be independent of r in this calculation. The average pressure can be represented as follows:

$$\frac{\bar{p}}{\rho} = \frac{P}{\rho} + \frac{R^2\Omega^2}{2} - \frac{1 + K^2}{b^2 - r_c^2} R^4\Omega^2 \ln \frac{b}{r_c} \tag{14}$$

The vertical gradient of this average pressure must now be computed, since it is this pressure gradient which acts as an upward force on the thermal element. The vertical gradient of the average internal pressure is given by

$$\frac{1}{\rho}\frac{\partial \bar{p}}{\partial z} = \frac{1}{\rho}\frac{\partial P}{\partial z} +$$

$$+ R\Omega^2 \left[\frac{\partial R}{\partial z}\left(\frac{4R^2}{b^2}\ln\frac{b}{r_c} - \frac{1}{1+K^2}\right) - \frac{\partial b}{\partial z}\frac{R^3}{b^3}\left(2\ln\frac{b}{r_c} - 1\right)\right](1+K^2) \tag{15}$$

The conventional form of the buoyancy force is written as

$$B = \frac{1}{\rho_1}\frac{\partial p}{\partial z} - \frac{\rho g}{\rho_1} \tag{16}$$

where ρ_1 is a reference density for the system under consideration. The hydrostatic equation defines the vertical gradient of the environmental pressure as

$$\frac{\partial P}{\partial z} = -\rho_o g \tag{17}$$

If (15), (16), and (17) are combined, the total buoyancy force per unit mass is given by

$$B = \frac{(\rho_o - \rho)}{\rho_1} g$$

$$+ R\Omega^2 \left[\frac{\partial R}{\partial z}\left(\frac{4R^2}{b^2}\ln\frac{b}{r_c} - \frac{1}{1+K^2}\right) - \frac{\partial b}{\partial z}\frac{R^3}{b^3}\left(2\ln\frac{b}{r_c} - 1\right)\right](1+K^2) \tag{18}$$

This expression represents the 'effective' buoyancy force acting on the convective material rising in a rotating fluid. The variable R can now be equated to an effective radius of entrainment, that is, the effective distance from which the plume or thermal entrains material inward.

The effective buoyancy expression given by (18) can be seen to be composed of what may be termed as the static buoyancy,

$$\frac{\rho_o - \rho}{\rho_1} g,$$

and a departure from the static conditions which is clearly dependent upon the angular velocity of the medium. It is apparent that the effective buoyancy reduces to the static buoyancy as the angular velocity of the fluid vanishes. In addition to the rotational dependence, the effective buoyancy is also dependent upon the effective radius of entrainment and the radius of the convective element as well as on the rate of change of both these parameters with height.

It is informative at this point to look at some simplifications of (18) which can be used later to obtain some complete solutions to the convective system. First, the critical radius r_c will be neglected with comparison to b. These two radii must differ by at least a factor of ten, thus the squares of these terms differ by at least two orders of magnitude. The term $\ln\frac{b}{r_c}$ will be replaced by β. In the further use of these equations, β will be considered a constant. The ratio b/r_c is at most a slowly varying function of b, and, becuase this ratio enters the subsequent equations as its logarithm, treating it as a constant will not introduce appreciable error.

The first special case of (18) which can be examined, may be derived from simple dimensional analysis relating the effective radius of entrainment R to the physical radius of the thermal. The simplest dimensional relationship would require that

$$R = \gamma b \tag{19}$$

where γ is a constant of proportionality. When this relation is used in addition to the assumptions mentioned above, (18) becomes

$$B = \left(\frac{\rho_o - \rho}{\rho_1} \right) g + [\gamma^2 (1+K^2) \; (1+2\beta) - 1] \; \gamma^2 \Omega^2 b \frac{\partial b}{\partial z} \tag{20}$$

An examination of (20) will show that the resultant buoyancy will either be increased or decreased depending on the relative magnitudes of β, K, and γ. It should also be noted that since the angular velocity of the environmental fluid enters the expression only as a squared term, it is the magnitude of the angular velocity and not the direction of rotation which controls the degree of suppression or enhancement of the buoyant motion. It should be remarked at this time that both rotational supression and rotational enhancement of thermal growth has been observed under differing laboratory conditions (McCarthy, 1967, McIntyre, 1967).

Two further simplifications of (20) are possible. Common to both of these is the assumption that K = 0. This implies that the radial velocity is small in comparison to the tangential velocity. This assumption would appear to be justified for the case of a free vortex where K may be on the order of 0.36 (Wilkins, 1964). However, when investigating the formative stage of the vortex and the interaction of the rotational motion with the thermal growth, the importance of convergence suggests that v_r may be as large as v_θ. In this case, K would not be negligible.

These two cases arise from considering two extreme conditions for the effective radius of entrainment. The first of these is based on the assumption that the effective radius of entrainment is equal to the radius of the convective element itself. This would require physically that material from the environment would be drawn inward by the entrainment process and transported inward to the center of the element. Such a condition would not be expected to occur in nature unless there existed a very strong circulation within the convective element. This condition does, however, represent one extreme for the behavior of the effective radius and is therefore of some theoretical interest. The relation R = b can thus be combined with (20) and the following expression for the effective buoyancy is obtained:

$$B = \left(\frac{\rho_o - \rho}{\rho_1}\right) g + 2b\Omega^2\beta \frac{\partial b}{\partial z} \tag{21}$$

In this case the effective buoyancy will be greater in a rotating field than the static buoyancy as long as the radius of the convective element increases with height. Necessarily, (21) reduces to the static buoyancy when the angular velocity vanishes.

A second special case of (20) may be constructed assuming that the effective radius of entrainment is constant with height. As in the previous case, this condition may rarely if ever be found in nature, but it does provide an interesting extreme value for the behavior of the radius of entrainment. If the expression R = constant is combined with (20), (again neglecting K), the following expression for the effective buoyancy is obtained:

$$B = \left(\frac{\rho_o - \rho}{\rho_1}\right) g - \frac{R^4\Omega^2}{b^3} (2\beta - 1) \frac{\partial b}{\partial z} \tag{22}$$

As opposed to (21), this relation indicates a reduction of the effective buoyancy forces under the influence of rotation and consequently a suppression of convection by the rotational field.

Although the generalized buoyancy term as given by (20) is somewhat difficult to visualize, the limiting cases as given by (21) and (22) lend themselves to a clear graphical representation. Figure 3a represents the internal pressure distribution for a convective element in which the effective buoyancy is given by (21). The heavy solid curves represent the pressure surfaces as seen in a vertical cross section taken through the axis of rotation. The dashed, sloping lines represent the boundary of the convective element and, in this case, also represent the effective radius of entrainment. The hyperbolic pressure surfaces are shown at two levels, and the horizontal average of the internal pressure is also shown. It is quite apparent that the average pressure surfaces within the convective element are more compressed than those in the environmental fluid. This would give rise to an increased vertical acceleration or a greater buoyancy. The structure of the pressure in a convective element governed by (22) is given by Figure 3b. The pressure surfaces and the element boundary are given in the same manner as in Figure 3a, however, in this case the effective radius of entrainment is indicated by the vertical lines, since in the development of (22) it was assumed that R = constant. The horizontal lines represent the average pressure acting on a horizontal cross section of the convective element. It is apparent that the gradient of pressure within the plume is less than that in the environment. Consequently this would indicate a reduced vertical acceleration or a reduced buoyancy.

Before examining the behavior of convective elements which are subjected to the effective buoyancy forces, it is instructive to examine

(18) in more detail. The coefficient of the bracketed term in (18) is always positive. Therefore the expression in brackets will determine the direction of departure from the static buoyancy when the fluid is subject to rotation. The critical condition can thus be represented by

$$\frac{\partial R}{\partial z}\left[\, 4R^2 \frac{(1+K^2)}{b^2 - r_c^{\,2}} \ln\frac{b}{r_c} - 1\right] \gtreqless \frac{\partial b}{\partial z} \frac{(1+K^2)}{b^2 - r_c^{\,2}} R^3\left(\frac{2b}{b^2 - r_c^{\,2}} \ln\frac{b}{r_c} - \frac{1}{b}\right) \tag{23}$$

Again, assuming $r_c^{\,2} \ll b^2$ and that $\ln(b/r_c)$ may be represented by the constant β, the preceding expression reduces to

$$\frac{\partial R}{\partial z}\left[\, 4\frac{R^2}{b^2}(1+K^2)\,\beta - 1\right] \gtreqless \frac{\partial b}{\partial z}(1+K^2)\frac{R^3}{b^3}(2\beta - 1) \tag{24}$$

The conditions indicated by >, =, and < are respectively those of buoyancy increasing with rotation, buoyancy unchanged with rotation, and buoyancy decreasing with rotation. The relation (24) shows how the effect of rotation on the thermal is governed by the growth rate of the cloud and its entrainment radius, in addition to the K factor of the induced vortex.

If the case first described in this chapter is considered, the inequality in (24) may be used to specify those values of γ for which the convection is either suppressed or enhanced by rotational effects. If the substitution $R = \gamma b$ is made, the inequality reduces to

$$\gamma^2 \gtreqless \frac{1}{(1 + K^2)\ (2\beta + 1)} \tag{25}$$

A map of γ vs K and β is shown in Figure 4. The values of γ shown are those for which the rotational effects will cause no change in the strength of the convection, i.e., where the equality in (25) holds. Any value of γ greater than the indicated value will cause rotational enhancement of convection at that value of K and β.

Several conclusions may be drawn from this chart. The first is a verification of the validity of using the constant β to replace $\ln(b/r_c)$. As can be seen, the variation of γ_{crit} is small as β is changed, and, since β is a logarithm, a relatively large change in the ratio b/r_c represents a small change in β.

It can also be seen that as the value of K increases, a smaller value of γ can yield rotational enhancement of convection. The value of K in effect represents a convergence term, i.e., a measure of the inward radial motion relative to tangential motion. This would imply, therefore, that both convergence and rotation tend to enhance convection.

The special cases mentioned previously are readily seen to be extreme cases when the chart in Figure 4 is examined. The special case where $\gamma = 1$, $K = 0$ is clearly a case of enhancement of convection. The case where the effective radius of entrainment is a constant ($\gamma = 0$) and $K = 0$ is conversely a clear case of suppression of convection, (unless the value of K or β approaches infinity, which is obviously another extreme case).

Maintained Adiabatic Plumes (in a rotating medium)

The convective plume resulting from a sustained source of buoyancy will be considered in this section. No attempt will be made to describe the internal velocity or density structure of the plume; rather a simple steady state condition will be used, based on the work of Morton, Taylor, and Turner (1956).

Three major assumptions must be included in this discussion. The first of these is a direct consequence of the desire for a uniform, steady state model. The velocity and density distributions will be considered uniform across the plume. This yields what has been referred to as a "top hat profile" in which the velocity is zero outside the plume and has a constant value inside its boundaries.

The second assumption is that the rate of entrainment at the edge of the plume is proportional to some characteristic vertical velocity at that height. This assumption may be open to some criticism; however the experimental verification of the nonrotating cases of convection by Morton, Taylor, and Turner and others tends to support this type of steady state model. The rotating cases studied by McCarthy, McIntyre and others also support this assumption. The assumption can also be supported by consideration of the mutual entrainment of the two fluids. If this mutual entrainment is indeed turbulent, then the determining quantity is the relative velocity of the two fluids, since the shear stress at the interface between the fluids is responsible for generating the turbulence.

The third assumption has already been used in the discussion of the buoyancy forces. The fluid is assumed to be Boussinesq, i.e., the density changes are small and thus can be referenced to some characteristic density in the system. This assumption simplifies the calculations considerably without significantly restricting the physical application of the model.

The plume may be described with a set of three equations which are referred to as the conservation equations. These are representations of the conservation of volume, momentum, and density deficit. The density deficit is used in this analysis in place of the standard thermodynamic formulation. As a consequence of the Boussinesq approximation, the density deficit can replace the temperature excess, since

$$\frac{\rho_o - \rho}{\rho_1} = \frac{T - T_o}{T_1} \tag{26}$$

where T, T_o, and T_1 are the plume temperature, environmental temperature and reference temperature, respectively, and ρ, ρ_o, and ρ_1 are the corresponding densities.

Consider a plane at location z perpendicular to the axis of the plume. The amount of volume passing through the plane in unit time is $\pi b^2 w$, where w is the vertical velocity of the plume at height z. At a plane δz above the first, the volume is $\pi b^2 w + \delta(\pi b^2 w)$. The increase in volume, $\delta(\pi b^2 w)$ is attributed to the entrainment taking place between z and $z+\delta z$. This can be written as $2\pi b w \alpha \delta z$, where α is the coefficient of entrainment. By equating these terms, and reducing them to derivative form, the equation of volume conservation may be obtained.

$$\frac{d}{dz}\ (\pi b^2 w) = 2\alpha w\pi b \tag{27}$$

The momentum equations can be easily developed from consideration of Newton's second law. The change in momentum over the distance δz can be represented by $\delta[(\pi b^2 w)\ (w)\ (\rho)]$. To balance this with the buoyancy term derived in the previous section one must recall that this term represented the buoyant force per unit mass. Thus the total force acting on the plume between z and $z+\delta z$ is $\pi b^2 z\rho B$, where B is the effective buoyancy force. Equating these terms and reducing them to derivative form in the momentum equation

$$\frac{d}{dz}\ (\pi b^2 w^2 \rho) = \pi b^2 \rho B \tag{28'}$$

Or, since density differences in the vertical are assumed small, this equation can be reduced to

$$\frac{d}{dz}\ (\pi b^2 w^2) = \pi b^2 B \tag{28}$$

Equation (27) represents the change of volume with height as a result of entrainment of additional volume from the environment. The same analysis applied to density deficit yields the equation

$$\frac{d}{dz}[\pi bw(\rho_1 - \rho)] = 2\pi b\alpha w(\rho_1 - \rho_o) \tag{29'}$$

By using (27) and simplifying, (29') can be reduced to

$$\frac{d}{dz}[\pi b^2 w(\rho_o - \rho)] = \pi b^2 w\ \frac{d\rho_o}{dz} \tag{29}$$

These equations may be reduced to slightly simpler forms by eliminating the constant π and by dividing (29) by the reference density ρ_1. These reduced forms below will be the basic model for the analysis of the effects of rotation.

$$\frac{d}{dz}(b^2 w) = 2\alpha wb \tag{30}$$

$$\frac{d}{dz}(b^2 w^2) = b^2 B \tag{31}$$

$$\frac{d}{dz}\left(b^2 \, wg \, \frac{\rho_o - \rho}{\rho_1}\right) = b^2 w \, \frac{g}{\rho_1} \, \frac{d\rho_o}{dz} \tag{32}$$

These three equations represent the Morton, Taylor, and Turner model with a generalized buoyancy term in the momentum equation. It is through this term that the effects of rotation can be introduced in the plume growth.

Instantaneous Adiabatic Thermals

The discussion of thermals growing in a rotating field may be conducted in a way similar to the discussion for plumes. The thermal is assumed to maintain a spherical shape. This assumption simplifies computation considerably and should not detract appreciably from the conclusions drawn from the study.

In the case of the plume, the structure of the motion was steady state, thus the conservation equations were derived with reference to the rate of change of the conserved quantities with height. The thermal is not a steady state process, however, and the equations will be derived with respect to the rate of change of the conserved quantities with time.

Morton, Taylor, and Turner (1956) assumed that the entrainment was a function of an 'effective' vertical velocity which was equal to a constant times the actual velocity. For simplicity in this study of the effects of rotation, this constant will be assumed to be one, i.e., the entrainment will be assumed proportional to the vertical velocity of the thermal.

The conservation equation for volume equates the rate of change of volume per unit time with the rate of addition of volume through entrainment:

$$\frac{d}{dt}\left(\frac{4}{3}\pi b^3\right) = 4\pi b^2 \alpha w \tag{33}$$

The conservation equation for momentum is simply the equivalent of Newton's second law for the thermal. The rate of change of momentum is equal to the applied force, which is in this case the buoyant force.

$$\frac{d}{dt}\left(\frac{4}{3}\pi b^3 w\rho\right) = \frac{4}{3}\pi b^3 \rho B \tag{34}$$

The density deficit equation can be derived by considering the densities associated with the volume changes in (33). Referencing all densities to ρ_1, the equation can be written

$$\frac{d}{dt}\left[\frac{4}{3}\pi b^3(\rho_1-\rho)\right] = 4\pi b^2 \alpha w(\rho_1-\rho_o) \tag{35}$$

Eqs. (33) and (35) can be combined to yield the more conventional form for the density deficit equation.

$$\frac{d}{dt}\left[\frac{4}{3}\pi b^3 g \frac{\rho_o-\rho}{\rho_1}\right] = \frac{4}{3}\pi b^3 w \frac{g}{\rho_1}\frac{d\rho_o}{dz} \tag{36}$$

Eq. (33) can be examined more closely to reveal a restriction inherent in this simple model. This expression reduces to

$$b = \alpha h \tag{37}$$

This relationship is verified experimentally by the results of <u>McCarthy</u> (1967), and <u>McIntyre</u> (1967), for the rotating thermals, and has been found to be valid for nonrotating thermals by <u>Woodward</u> (1959), <u>Morton, Taylor, and Turner</u> (1956), and <u>Turner</u> (1963).

The set of conservation equations can be reduced to their simpler form which will then be used for the individual case studies. The assumption of small density variation with height permits the elimination of ρ in (34). The reduced equations represent the Morton, Taylor, and Turner model with a generalized buoyancy term, incorporating the buoyancy flux B:

$$\frac{1}{3}\frac{d}{dt}(b^3) = \alpha b^2 w \tag{38}$$

$$\frac{d}{dt}(b^3 w) = b^3 B \tag{39}$$

$$\frac{d}{dt}\left(b^3 g \frac{\rho_o-\rho}{\rho_1}\right) = b^3 w \frac{g}{\rho_1}\frac{d\rho_o}{dz} \tag{40}$$

$$\frac{dz}{dt} = w \tag{41}$$

Maintained Non-Adiabatic Plumes

In describing the non-adiabatic maintained convective plume, the "top hat" profile of vertical velocity and density will again be assumed. In addition, the rate of production of buoyancy will also be assumed to be constant over the cross-sectional area of the plume.

If the rate of buoyancy production is defined as the volume produced per unit time per unit vertical distance and represented by θ, the equation of conservation of volume may be deduced by reasoning similar to that used in the discussion of adiabatic plumes.

$$\frac{d}{dz}(\pi b^2 w) = 2\alpha w\pi b + \theta \tag{42}$$

The momentum equation is no different for the non-adiabatic plume than for the adiabatic plume and thus can be written as

$$\frac{d}{dz}(\pi b^2 w^2 \rho) = \pi b^2 \rho B \tag{43}$$

where B is the generalized buoyancy term. At first it might appear strange that the vertical momentum equation would not be changed for the non-adiabatic case. The expression remains the same, but the generalized buoyancy term must now include the total buoyancy forces as determined by the third conservation equation which considers the density deficit of the plume.

The density deficit conservation equation may now be derived by considering the densities associated with each of the volume terms in (42). If the densities of the thermal, the environment, and the new buoyant material are represented by ρ, ρ_1 and ρ_g respectively, the equation may be written in the form

$$\frac{d}{dz}[\pi b^2 w(\rho_1-\rho)] = 2\pi b\alpha w(\rho_1-\rho_o) + \theta(\rho_1-\rho_g) \tag{44}$$

This expression may be combined with (42) to yield

$$\frac{d}{dz}\left(\pi b^2 wg \frac{\rho_o-\rho}{\rho_1}\right) = \pi b^2 w \frac{g}{\rho_1}\frac{d\rho_o}{dz} + \theta g \frac{\rho_o-\rho_g}{\rho_1} \tag{45}$$

In this form, the hydrostatic buoyancy forces of the plume and the newly created material are given by $g\frac{\rho_o-\rho}{\rho_1}$ and $g\frac{\rho_o-\rho_g}{\rho_1}$ respectively. These terms will be represented by Δ with appropriate subscripts. The expression $-\frac{g}{\rho_1}\frac{d\rho_o}{dz}$ is generally referred to as the static stability and will be denoted by S. Thus, (45) becomes

$$\frac{d}{dz}(\pi b^2 w\Delta) = -\pi b^2 wS + \theta\Delta_g \tag{46}$$

A more complete discussion of Δ_g and the production term is included in the section on non-adiabatic thermals.

Instantaneous Non-Adiabatic Thermals

In considering the case where the total buoyancy force changes during the growth and development of a convective element, one must modify the conservation equations which were developed for the adiabatic case. In the adiabatic case, the only change in volume of the original buoyant mass was that growth due to entrainment processes. The volume may also increase due to the addition of new buoyant material which is generated during the thermal growth. If this rate of change of volume growth due to production is denoted by φ, then the volume conservation equation becomes

$$\frac{d}{dt}\left(\frac{4}{3}\pi b^3\right) = 4\pi b^2 \alpha w + \varphi \tag{47}$$

In the case of thermal growth in the atmosphere, this would represent the expansion of the cloud element due to latent heat release. In the experimental analogy discussed by McCarthy (1967), and McIntyre (1967), however, it is merely the additional CO_2 volume due to CO_2 bubbles which formed as the thermal element continues to rise and as the dilute HCl continues to react with the entrained environmental carbonated water.

The conservation of momentum equation will not be changed in form although the momentum of the thermal will definitely increase with increasing buoyancy production. The value of B, the generalized buoyancy term, will grow at a faster rate, but it enters into the momentum equation in precisely the same form as in the adiabatic case. Thus the second equation to be considered becomes

$$\frac{d}{dt}\left(\frac{4}{3}\pi b^3 w\rho\right) = \frac{4}{3}\pi b^3 \rho B \tag{48}$$

The third equation, the conservation of density deficit, may be developed by studying the density changes associated with each term in (47). If all densities are compared to some reference density ρ_1, the equation may be written as

$$\frac{d}{dt}\left[\frac{4}{3}\pi b^3(\rho_1-\rho)\right] = 4\pi b^2\alpha w(\rho_1-\rho_o) + \varphi(\rho_1-\rho_g) \tag{49}$$

where ρ represents the mean density in the thermal, ρ_o the environmental density and ρ_g the density of the additionally produced volume.

The density deficit conservation equation may be reduced to a more simple form by combining it with the volume conservation equation (47). This final form may be written

$$\frac{d}{dt}\left[\frac{4}{3}\pi b^3\, g\frac{\rho_o-\rho}{\rho_1}\right] = \frac{4}{3}\pi b^3 w\,\frac{g}{\rho_1}\frac{d\rho_o}{dz} + \varphi g\,\frac{\rho_o-\rho_g}{\rho_1} \tag{50}$$

Furthermore, $g\frac{\rho_o-\rho}{\rho_1}$ is the hydrostatic buoyancy force per unit volume, Δ, and $-\frac{g}{\rho_1}\frac{d\rho_o}{dz}$ is one representation of the static stability of the environment, S, and

$$\frac{d}{dt}\left[\frac{4}{3}\pi b^3\Delta\right] = -\frac{4}{3}\pi b^3 wS + \varphi\Delta_g \tag{51}$$

where Δ_g is the buoyancy force per unit volume of the new material produced as the thermal rises.

In the atmosphere Δ_g would equal Δ because the cloud could be considered homogeneous. The term φ would be determined from the equation of state for the cloud material and the amount of latent heat release would be determined from another conservation equation accounting for the total moisture contained in both vapor and liquid phase. Such considerations, however, are beyond the scope of this paper; instead these equations will be modified so as to best model the experimental thermals produced by the acid-carbonated water reaction used by McCarthy and McIntyre. In this case, the environmental fluid is water and the density of the new material produced is assumed to be negligible (CO_2 gas compared to water). With a proper choice of ρ_1, the reference density, the ratio $(\rho_o - \rho_g)/\rho_1$ may be assumed to be near unity and thus

$$\Delta_g \doteqdot g \tag{52}$$

<u>Production of Buoyancy</u>

The production of buoyant material for the thermal, φ, and the plume, θ, has been included in the development of the general conservation equations for the convective elements. These terms could represent any type of buoyancy production. However the only form which will be analyzed here will be that which will describe the processes occurring in the acid-carbonated water reaction.

Carbon dioxide is released from solution whenever the acid lowers the solubility of CO_2 in the carbonated water. Thus as the convective element rises in the thermal tank, the rate of production of CO_2 should be proportional to the surface area of the acidic cloud exposed to the carbonated water. The CO_2 production rate should also be proportional to the acid concentration within the cloud. By neglecting the volume of the CO_2 bubbles when compared to the total cloud volume, an expression for the thermal buoyancy production rate may be written as

$$\varphi = D(4\pi b^2)\ v\ (\frac{4}{3}\pi b^3)^{-1} = \frac{3vD}{b} \tag{53}$$

where v is the initial volume of the acid injection. The term $v(\frac{4}{3}\pi b^3)^{-1}$ is simply the acid concentration after the thermal has grown to radius b. The surface area is $4\pi b^2$ and the term D is a proportionality constant which has the units of velocity. This experimentally determined constant is generally called a diffusion velocity; as a first approximation D can be considered as equivalent to the average rate of radial growth of the cloud.

By exactly the same reasoning, the expression for buoyancy production in the sustained plume may be developed. This would take the form

$$\begin{aligned}\theta &= D(2\pi bw)\ u\ (\pi b^2 w)^{-1} \\ &= \frac{2uD}{b}\end{aligned} \tag{54}$$

where u is the acid volume injected per unit length of the plume. The volume passing a horizontal plane per unit time is $\pi b^2 w$ and associated with this volume is a surface area of $2\pi bw$.

Note that by the proper definitions of the terms φ, θ, u, and v, it is possible to obtain the same general type of dependency on b, w, and D. This inverse radius formulation has quite satisfactorily explained McCarthy's experimentally observed production rates, and is based physically on our laboratory measurements on the quantities of CO_2 evolved from known quantities of one normal HCl into water carbonated to a standardized solution.

Solutions of the Conservation Equations for Sustained Plumes

The conservation equations for both adiabatic and non-adiabatic plumes may be written in their most general form as follows:

$$\frac{d}{dz}(b^2 w) = 2\alpha wb + \frac{\theta}{\pi} \tag{55}$$

$$\frac{d}{dz}(b^2 w^2) = b^2 B \tag{56}$$

$$\frac{d}{dz}(b^2 w\Delta) = -b^2 wS + \frac{\theta\Delta g}{\pi} \tag{57}$$

where

$$B = \Delta + R\Omega^2\left[\frac{dR}{dz}\left(\frac{4R^2(1+K^2)}{b^2-r_c^2}\ln\frac{b}{r_c} - 1\right) - \frac{db}{dz}\frac{(1+K^2)}{b^2-r_c^2}R^3\left(\frac{2b}{b^2-r_c^2}\ln\frac{b}{r_c} - \frac{1}{b}\right)\right] \tag{58}$$

$$S = -\frac{g}{\rho_1}\frac{d\rho o}{dz} \tag{59}$$

$$\Delta = g\left(\frac{\rho_o-\rho}{\rho_1}\right) \; ; \; \Delta_g = g\left(\frac{\rho_o-\rho_g}{\rho_1}\right) \tag{60}$$

where equation (58) is derived in the first portion of this chapter and, under the conditions for the experimental model,

$$\theta = \frac{2uD}{b} . \tag{61}$$

One can immediately see the difficulty in obtaining any type of meaningful solution to these equations. The system of equations may be simplified by making the same assumptions as were discussed in deriving (20). Because this model essentially is attempting to explain the processes taking place in the experimental apparatus, the density of the new buoyant material will be neglected when compared to water, and therefore the hydrostatic buoyancy term Δ_g is nothing more than the acceleration of gravity, g. (This assumes a choice of the reference density ρ_1, equal to the environmental density, ρ_o which is strictly possible only when dealing with a neutral environment.)

With these assumptions, the conservation equations now become:

Volume:

$$\frac{d}{dz}(b^2 w) = 2\alpha wb + \frac{2uD}{\pi b} \tag{62}$$

Vertical momentum:

$$\frac{d}{dz}(b^2 w^2) = b^2\Delta + b^3 \Lambda^2 \frac{db}{dz} \tag{63}$$

Density deficit:

$$\frac{d}{dz}(b^2 w\Delta) = -b^2 wS + \frac{2uDg}{\pi b} \tag{64}$$

where

$$\Lambda^2 = [\gamma^2(1+K^2)\ (1+2\beta)\ -1]\ \gamma^2\Omega^2 \tag{65}$$

represents the collection of constants in the generalized buoyancy expression, the symbols having the same meaning as in (20).

The vertical change in radius may be obtained from (62) and (63):

$$\frac{db}{dz} = \frac{4\alpha w^2 + \dfrac{4uwD}{\pi b^2} - b\Delta}{b^2\Lambda^2 + 2w^2} \tag{66}$$

An analysis of (66) shows that the right hand side of the equation need not be positive. Indeed, if the buoyancy is too large, the high degree of vertical stretching will cause the cross section of the plume to remain constant or even decrease with height. As can be seen by examining the numerator of the expression, the entrainment process and the volume production terms tend to cause the radius to increase with height while the hydrostatic buoyancy term tends to cause a decrease of the radius.

When (66) is combined with (63) the vertical momentum equation may be written

$$\frac{d}{dz}(b^2w^2) = \frac{2w^2b^2\Delta + 4\alpha b^3w^2\Lambda^2 + \frac{4buwD\Lambda^2}{\pi}}{b^2\Lambda^2 + 2w^2} \tag{67}$$

Thus, ideally (62), (67), and (64) provide a complete set of three equations in three unknowns - which could at least in theory be solved for the parameters which describe the growth of the plume. Practically speaking, however, the solution of these equations is impossible in closed form.

Two approaches to their solutions are possible. The first was accomplished for the adiabatic case by <u>Sasaki and Friday</u> (1967). This consisted of first non-dimensionalizing the equation set and then finding a series solution asymtotically approaching the true solution near the origin. These series solutions were derived for the case when $\gamma = 1$ and $K = 0$. The results for the non-dimensional radius, vertical velocity, and buoyancy were found to be

$$r_b = 0.6\alpha h - 0.0066\alpha^{7/3}(0.96\alpha^2\lambda^2 - S)h^{11/3} + \ldots \tag{68}$$

$$v = 1.0138\alpha^{-2/3}h^{-1/3} + 0.0293\alpha^{7/3}(0.96\alpha^2\lambda^2 - S)h^{7/3} + \ldots \tag{69}$$

$$d = 2.7407\alpha^{-4/3}h^{-5/3} - 0.375sh - 0.0195(0.96\alpha^2\lambda^2 - S)h + \ldots \tag{70}$$

where r_b, v, d, h, s, and λ are the non-dimensional radius, vertical velocity, buoyancy, height, stability, and rotation rate respectively.

One of the most striking results of this series solution was the existence of the term $(0.96\alpha^2\lambda^2-S)$ which actually plays the role of an effective stability term. Thus the series solution implies that the major effect of rotation is to change the effective stratification of the environmental fluid, and that in this case, (γ=1,K=0) rotation tends to make the stratification more unstable.

This asymtotic series expansion is useful for this simple case, but it would be exceedingly tedious to apply to the conservation equations in (62), (67), and (64). Instead, these equations are solved for the height derivatives of b, w, and Δ and are numerically integrated. The height derivative of the plume radius is given by (66). In addition, the equations for w and Δ may be written

$$\frac{dw}{dz} = \frac{(b^2\Lambda^2 - 2w^2)\ (2\alpha\pi wb^2 + 2uD) + 2w\Delta}{\pi b^3\ (b^2\Lambda^2 + 2w^2)} \tag{71}$$

$$\frac{d\Delta}{dz} = -S - \frac{2\alpha\Delta}{b} + \frac{2uD}{\pi b^3 w}\ (g-\Delta) \tag{72}$$

These equations have been numerically integrated for solutions of the basic parameters. However, since the experimental studies have thus far concerned themselves only with thermals, the plume solutions will not be included in this paper.

Instantaneous Thermals

The solution of the instantaneous thermals will be demonstrated by the use of the buoyancy expression given by (20). In this expression, the effective radius of entrainment is assumed to be proportional to the visible radius of the plume. The buoyancy production term given by (53) will be employed and the assumption that the density of the generated CO_2 gas may be neglected when compared to water will also be used. After these substitutions have been made the equations may be written as follows:

Volume:

$$\frac{1}{3}\frac{d}{dt}(b^3) = b^2\alpha w + \frac{3vD}{4\pi b} \tag{73}$$

Momentum:

$$\frac{d}{dt}(b^3 w) = b^3\Delta + \Lambda^2 b^4 \frac{db}{dz} \tag{74}$$

Density deficit:

$$\frac{d}{dt}(b^3\Delta) = -b^3 wS + \frac{9}{4}\frac{vDg}{\pi b} \tag{75}$$

The expression for momentum conservation may be further simplified by noting that

$$\frac{db}{dz} = \frac{1}{w}\frac{db}{dt}$$

and from (73)

$$\frac{db}{dt} = \alpha w + \frac{3vD}{4\pi b^3} \qquad (76)$$

The expression above provides an easy means of evaluating the relative effect of entrainment vs buoyancy production, the last term in (76) is simply the diffusion velocity multiplied by the ratio of the initial volume of the injected acid solution to the volume of the thermal at any time later. Thus, after the cloud begins to grow, this term decreases rapidly in importance. Experimental results indicate that this term can be neglected in the volume conservation equation with no noticeable loss of accuracy. Thus (73) becomes

$$\frac{1}{3}\frac{d}{dt} b^3 = b^2 \alpha w \qquad (77)$$

and (76) becomes

$$\frac{db}{dt} = \alpha w \qquad (78)$$

Therefore, the momemtum equation now becomes

$$\frac{d}{dt} b^3 w = b^3 \Delta + \Lambda^2 b^4 \alpha \qquad (79)$$

Equations (75), (77), and (79) then provide the necessary relationships which can be examined for a solution. For manipulative purposes, it is useful to make the following substitutions:

$$V = b^3$$
$$M = b^3 w \qquad (80)$$
$$F = b^3 \Delta$$

These substitutions correspond to the volume, momentum, and total buoyancy of the thermal. The equations after substitution may be written

$$\frac{dV^{4/3}}{dt} = 4\alpha M \qquad (81)$$

$$\frac{dM}{dt} = F + \Lambda^2 \alpha V^{4/3} \qquad (82)$$

$$\frac{dF}{dt} = -MS + CV^{-1/3} \qquad (83)$$

where

$$C = \frac{9vDg}{4\pi} \qquad (84)$$

These equations are still non-linear but are of a much simpler form than those before substitution. At this point, the solution techniques of Morton, Taylor, and Turner will be modified. Morton, Taylor, and Turner first non-dimensionalized the equations and then solved them. This step is not necessary and in some cases may actually be misleading. If the environmental stability is used to non-dimensionalize the equation set, the effect of stability is masked in the resulting solutions. When dealing with a neutral environment, the solutions may not be valid. For these reasons, the equations will be solved in their dimensional form.

By differentiating (82) with respect to time and substituting

(81) and (83) into the resulting equation, the following relationship is obtained:

$$\frac{d^2M}{dt^2} = M(4\Lambda^2\alpha^2 - S) + CV^{-1/3} \tag{85}$$

Clearly, the problem would be quite easily solved if the second term on the right were not present. This term arises becasue of the production of additional buoyancy during the lifetime of the thermal. In an adiabatic thermal (one in which all buoyancy changes resulted from entrainment from the environment) this term would be zero and the resultant solutions for M would be

$$M = \frac{F_o}{s_*} \begin{cases} \sinh\ (s_* t) & ; \quad s_*^2 > 0 \\ \sin\ (s_* t) & ; \quad s_*^2 < 0 \end{cases} \tag{86}$$

where F_o is the initial (t=0) value of the buoyancy flux, and

$$s_*^2 = (4\Lambda^2\alpha^2 - S) \tag{87}$$

This expression permits a clear-cut evaluation of the rotational effect. With no rotation, the effective stability, s_*^2, would be equal to the environmental stability. The rotation term, Λ^2, causes the stratification to become more unstable (s_*^2 becomes positive). It is possible, therefore, for a stable environment, S positive, to behave as a stable environment, s_*^2 negative; as a neutral environment, s_*^2 zero; or as an unstable environment, s_*^2 positive; depending upon the value of the rotational term Λ^2. The effects of these various stabilities are shown in (86). The stable environment is characterized by an oscillatory solution and the unstable environment by an exponential growth of momentum.

It must be remembered, however, that the previous discussion assumed that Λ^2 is positive. In the discussion of the generalized buoyancy term it was seen that this term could be negative under realistic conditions. In this case, the rotation would have the tendency of stabilizing an unstable environment.

The adiabatic solutions for the stable environmental behavior ($s_*^2<0$) are given as follows.

$$M = \frac{F_o}{s_*} \sin (s*t)$$

$$V = [4\alpha F_o \ / \ s_*^2]^{3/4} \ [\ 1-\cos(s_* t)]^{3/4} \qquad (88)$$

$$F = F_o \quad \frac{s}{s_*^2} [\cos(s_* t) \ -1] + 1$$

where s_*^2 is the absolute value of $(4\Lambda^2\alpha^2-S)$. From the basic solutions, the substitutions given in (80) may be used to solve for r, w, and Δ.

In the case where the environment behaves effectively neutral, $s_*^2 = 0$, the solutions are given simply by

$$M = F_o \ t$$

$$V = (2\alpha F_o)^{3/4} t^{3/2} \qquad (89)$$

$$F = F_o(1- \frac{St^2}{2})$$

In this case, the original variables are easily given by

$$b = (2\alpha F_o)^{1/4} t^{1/2}$$

$$w = F_o^{1/4} (2\alpha)^{-3/4} t^{-1/2} \tag{90}$$

$$\Delta = F/V$$

When the effective environmental stratification is unstable, the solutions take on the characteristic exponential growth as follows.

$$M = \frac{F_o}{s_*} \sinh (s_* t)$$

$$V = (4\alpha F_o / s_*)^{3/4} (\cosh s_* t - 1)^{3/4} \tag{91}$$

$$F = F_o \left(1 + \frac{S}{s_*^2} [1 - \cosh(s_* t)]\right)$$

These solutions given by (88), (89), (90) and (91) represent the adiabatic thermal. They were obtained by ignoring the production term in (85). If the thermal radius is not changing at a rapid rate, the term $CV^{-1/3}$ (which is C/b) can be considered nearly constant, C' say. This assumption may be valid at some distance from the origin. In a stable environment, the solutions to such a system would be

$$M = \frac{F_o}{s_*} \sin(s_* t) + \frac{C'}{s_*^2}$$

$$V = \left\{ \frac{4\alpha F_o}{s_*^2} [1 - \cos(s_* t)] + \frac{4\alpha C'}{s_*^2} t \right\}^{3/4} \tag{92}$$

$$F = F_o\left\{\frac{S}{s_*^2}[\cos(s_* t) - 1] + 1\right\} + C'(1 - \frac{S}{s_*^2})\,t$$

Solutions similar to (89), (90), and (91) may be obtained under this assumption, but they will not be given here.

Although the above solutions are interesting in their own right, they still do not consider the combined effects of rotation and non-adiabatic buoyancy production. Unfortunately, only approximate forms of these complete solutions can be obtained. Both numerical solutions and asymtotic expansions about $t = 0$ have been generated for the conservation equations.

The series solutions technique (Sasaki and Friday, 1967) yields the following results for the first three terms in the expansion for the radius b, the vertical velocity w, and the buoyancy acceleration Δ.

$$\begin{aligned} b &= Bt^{3/5} + 0.00165ABt^{13/5} + 0.000287BA^2t^{23/5} + \ldots \\ w &= \frac{3}{5\alpha}Bt^{-2/5} + \frac{0.0429AB}{\alpha}t^{8/5} + \frac{0.00132}{\alpha}BA^2t^{18/5} + \ldots \\ \Delta &= \frac{21B}{25\alpha}t^{-7/5} + \left[\frac{0.0612AB}{\alpha} - \Lambda^2\alpha B\right]t^{3/5} + \\ &\quad \left[0.0087\frac{BA^2}{\alpha} - 0.00165\,\Lambda^2AB\right]t^{13/5} + \ldots \end{aligned} \tag{93}$$

where

$$\begin{aligned} A &= 4\Lambda^2\alpha^2 - S \\ B &= \left[\frac{375\ v\ Dg\alpha}{56\pi}\right]^{1/5} \end{aligned} \tag{94}$$

Examination of these solutions shows the alternating sign effect that the value of the effective stability, A, will have. This term enters increasing ordered terms in increasing degrees. Therefore, if the term is negative (stable) the solution takes on the appearance of an alternating series or sine series. If the value of A is positive, however, then all terms in the series for b and w are positive and the series indicates growth without bounds. Although these series solutions are true only at time very near zero, they do illustrate the effects of the various physical parameters in the thermal growth much more clearly than a series of numerical solutions might do. The numerical solutions, however, are still needed for the analysis of the thermal element growth as one becomes removed from the initial portion of thermal growth.

Numerical Integration of the Conservation Equations

Both adiabatic and non-adiabatic thermals have been examined numerically. In the adiabatic case, the system of equations was programmed to allow initial conditions to be specified as to initial cloud volume, initial vertical velocity and initial cloud density. Environmental parameters of stability and rotation were also specified as input parameters to the computer program. The thermal parameters γ, K, and α were also varied from run to run to determine the effects of these parameters on thermal growth. A complete list of the input parameters for 32 adiabatic runs is given in Table I.

The effect of initial vertical velocity was studied in runs 1, 2, and 3. Initial vertical velocities of 0, 10, and 20 cm/sec. were tried with a thermal representing the approximate conditions for a nonrotating tank experiment. It was felt that this investigation was crucial to determine if the finite vertical velocity of injection had any appreciable effect on the experimental studies. As is easily seen in Figure 5, the only apparent difference in the curves is in the initial half second of the velocity curves. Certainly, the shapes of the curves are not affected, and one has difficulty determining any difference in the time vs radius, time vs height, or time vs volume curves. Thus, the effect of the initial vertical velocity is quickly lost as the thermal grows. Turner (1963) reported essentially this effect in his experiments with injected thermals when he said that the growing thermal quickly "forgets" how it originated. It can be concluded, therefore, that the finite injection speed will not invalidate any of the tank experiments.

Runs 1, 2, and 3 were made using an entrainment coefficient α = 0.10. Runs number 4 and 5 were made to study the effect of this entrainment coefficient on the nonrotating thermal growth. The value of $\alpha = 0.22$ was used for run 5 as compared to a value of $\alpha = 0.10$ in run 4. All other parameters were held the same. An examination of Figure 6 clearly reveals the effect of the variation of α. The vertical velocity is considerably reduced for $\alpha = 0.22$ as compared to $\alpha = 0.10$. Consequently, the height vs time curves and the time vs radius curves show considerable suppression for the larger entrainment coefficient. The volume increases faster with the higher entrainment coefficient. These graphs are clear evidence of the physical processes taking place. With the higher entrainment coefficient, more material is being drawn into the thermal element, consequently the volume is increasing faster than a convective element with a lower value of α. This increase in the amount of environmental fluid brought into the thermal causes a dilution of the buoyant materials, and, even though the total buoyancy force remains constant in the adiabatic case, the buoyancy per unit volume of the thermal is reduced. This results in a reduction in the buoyant acceleration of the thermal and a consequent reduction in vertical velocity. The reduction in height of rise of the thermal is a direct result of the decrease in vertical velocity. A limiting case for α would be illustrated by an air bubble rising in water or a mass of fluid rising in another fluid with which it is immiscible, kerosene in water, for example. In this case, α would have a value of zero, and the bubble would continue to accelerate, being limited in its vertical velocity only by the drag forces on its surfaces.

The value of $\alpha = 0.22$ was more representative of the experimental results obtained with the tank apparatus and this was used throughout the remainder of the numerical calculations.

The next parameter which was investigated numerically was γ, the ratio of the effective radius of the entrainment to the radius of the thermal element. The theory simplifies considerably if the value of γ can be set equal to one, but there is no compelling argument for such a simplification at this time. Runs 6 - 9 (Fig 7) were made for a rotating thermal environment, and values of γ equal to 1.00, 0.75, 0.50, and 0.25 respectively. In run number 6 the enhancement of thermal growth by rotation is clearly apparent. The vertical velocity first begins to drop and then after the first 1.5 seconds begins to increase as the entrainment process causes a compression of the pressure surfaces and a consequent acceleration in the vertical. The vertical velocity graph for run 7 (γ = 0.75) shows only a minor acceleration after about 3 seconds of thermal growth. The entrainment process is still acting over a great enough lateral extent to cause a contraction of the average pressure surface internal to the thermal. As the value of γ is reduced to 0.5, as in run 8, this rotational enhancement is further reduced. In the case of γ = 0.25, run 9, there is no apparent enhancement by rotation. The results actually indicated a slight suppression by the rotational environment when run 9 is compared with run 5, for example. These effects of the change in vertical velocity carry over quite naturally to the other parameters. The time vs height curves show a suppression in thermal growth as the value of γ is reduced from 1.00 to 0.25. Similarly, since the entrainment is proportional to vertical velocity, the volume is reduced as the value of γ is lowered. The curves for momentum vs time show the same tendency for the intensity of the thermal to be reduced as the value of γ is reduced. The value of γ may be related descriptively to the vigor of the thermal element. It is reasonable to assume that a vigorous convective element, due to its own internal motions, would entrain environment fluid from a greater distance than one which had a less active internal circulation. Thus it appears from this numerical model that the more vigorous the thermal element, the more enhancement it will receive by a rotational field. Runs 10 through 14 show little change as the parameter K is varied from zero to one. This is primarily because of the overriding effect of the value of γ used during these runs. The value of $\gamma = 0.25$ caused the effect of rotation to be minimized, as was seen in run 9. Consequently, the value of K, which affects the rotation term only, had little effect.

The effect of varying the rotation of the environment alone is shown in Figure 8 which represents runs 5, 6, 15 and 16. All runs were made with a value of $\gamma = 1.00$ which, as has been mentioned earlier, provides a clear demonstration of the rotational enhancement. Run 5 is the nonrotating case, and the vertical velocity rises immediately and then begins to decay exponentially as the thermal is diluted by environmental entrainment. The case illustrated by run 6, a 10-rpm experiment, shows an increase in vertical velocity after about 1.5 seconds. In this case we have the entrainment dilution taking place as well as the vertical acceleration caused by a compression of the average pressure surfaces. In run 15 the vertical acceleration is stronger and the vertical velocity begins to increase after 0.7 seconds. Run 16 with $\Omega = 30$ rpm has the minimum in vertical velocity occurring at about 0.5 seconds. The other parameters vary as would be expected from the variation in vertical velocity. The time vs height curves show a rapid increase of height with time as the rotation rate increases. Because the vertical velocity increases with increasing rotation, one would expect both the volume and the total momentum of the thermal to increase with rotation. This is verified by the curves of time vs volume and time vs momentum.

Since the size of the thermal released into the experimental tank could be varied, runs 15 and 17 were made to determine the effect of initial thermal size on the growth process. Only the volume of the initial thermal was varied. An examination of Figure 9 reveals that the effect of thermal size is essentially to change the ordinate of the curves, but not their general shape. The velocity minimum occurs at the same time in both cases, at about 0.7 seconds. The velocities are smaller for the smaller thermal, but the shape of the curves of velocity, height, etc. is unchanged.

Computer runs 18 and 19 illustrate the effect of an unstable environment (Fig 10). As would be expected there is some enhancement of convection by the entrainment from an unstable environemnt. These two runs were made with $\gamma = 1.0$ and thus show the maximum rotational enhancement effects. Runs 27 and 28 are cases of unstable environment with $\gamma = 0.50$. At this value of γ the rotational enhancement is still there, although quite small (Fig 11).

Runs 20 through 23 (Fig 12) illustrate the effect of rotation on a thermal rising in a stable environment. There is convectional enhancement with rotation as in the other cases with $\gamma = 1.0$. Runs 29 through 32 show the same stable case with $\gamma = 0.50$. Clearly, the rotational enhancement of convection is much less in this case (Fig 13).

The non-adiabatic cases were studied using 4 sets of numerical experiments consisting of varying the rotation rate in four steps from 0 to 30 rpm. The first three of these sets were made using the same parameters with the exception of the value of γ. This was chosen as $\gamma = 1.0$ for the first series, $\gamma = 0.5$ for the second and $\gamma = 0.25$ for the third. The last series was run with $\gamma = 1.0$ and the diffusion velocity D set equal to 10.0 cm/sec as compared to the experimentally determined value of 5.5 cm/sec. The values of the input parameters for the 12 non-adiabatic runs are given in Table II.

Figure 14 deals with the first set of experiments, runs 1 through 4. The vertical velocity, height, and momentum graphs all clearly show enhancement by rotation. The graph of time vs bouyancy production, however, shows a decrease with increasing rotation. This result may be somewhat misleading since it might be interpreted as rotational suppression. However, the buoyancy production term φ has been shown to be an inverse function of the thermal radius. Physically this is related to the increased rate of thermal growth causing an increased dilution of the acid which causes the production of the CO_2 bubbles.

Runs 5 through 8 in Figure 15 show the same sense of variation with rotation. However for the value of $\gamma = 0.50$ used in this set of experiments the rotational enhancement is considerably reduced.

Figure 16 illustrates the effect of $\gamma = 0.25$ on thermal behavior. Although graphically there is no discernible difference, the numerical values did show a slight suppression of the convection by rotation.

Figure 17 represents the final series of numerical experiments which have been conducted in this study of non-adiabatic thermal growth. With the exception of the value of the diffusion velocity, D, all parameters are the same as in the first 4 runs illustrated in Figure 14. The effect of an increased diffusion velocity is to increase the rate of buoyancy production and thus accelerate the thermal growth. This is clearly evidenced by comparison of height, vertical velocity and momentum curves for the two figures. An interesting effect of this process however, is the more rapid dilution of the acid and the consequent more rapid decrease in the buoyancy production. This can be seen by a comparison of the buoyancy production vs time graphs for these two cases.

CHAPTER III

NUMERICAL MODELLING OF ROTATING CONVECTIVE ELEMENTS

A numerical model was developed which represented the solutions to the equations of motion and the thermodynamic equation which define the basic properties of shallow convection. (Shallow convection is used in this sense as in Ogura and Phillips (1962), i.e., convection through depths considerably less than the depth of a dry adiabatic atmosphere.) The numerical model used is described fully in Appendix A.

First examined was the truncation error caused by the numerical scheme, grid size, and boundary conditions employed in the experiments. Several preliminary computer runs were made for this purpose. The boundaries of the domain considered are solid, i.e., no flow is allowed to cross the boundaries. It is essential then to assure that the results of the experiments are dependent on the physics of the problem and not on the solid boundaries. Several runs were made with the same size and strength of the convective element, but with different grid sizes. It was observed that the lateral boundaries had the least effect upon the growth of the convective element. The fields of meteorological parameters were essentially unchanged under conditions of various radial grid sizes. This fact, coupled with the result that the rate of convergence of the vorticity equation is increased radically for small radial distances, dictated the choice of a small radial distance. The radial dimension of 10 grid units was chosen for the remainder of the numerical experiments.

This initial series of experiments illustrated the strong influence of the top boundary on the convective motion. It was desired to study the first three km of the thermal growth, consistent with the validity of the shallow convection model used in this study. It was observed that the shape of the thermal element became strongly influenced by the top boundary when it was within one km of that surface. It was therefore necessary to choose the vertical distance of four km or more for the purpose of this study. This prevented the top boundary from having any appreciable effect on the shape or rate of growth of the thermal for the first three kilometers of its growth.

The choice of a grid spacing of 200 meters and a time interval of three seconds resulted from an analysis of experimental results which illustrated no significant differences when the computer model was run with smaller space and time intervals. These values were chosen on the basis of an economical computer program, both in terms of core storage and run time. With the choice of space and time intervals mentioned above, the system is computationally stable for the 15-minute time period of thermal growth studies in these experiments. This can be verified by observing the energy budget considerations presented later in the discussion.

Adiabatic Experiments

A total of six adiabatic experiments were conducted. These are included in Table III which gives the pertinent parameters associated with each experiment. These were all made with the same thermal configuration. The thermal was initially 300 meters above the center of the cylinder of air and is described by A.29 having a maximum temperature excess of $3^{o}C$. Results were printed out for all grid points every minute. The numerical forecast was run for 15 minutes for all runs except run 2 which was carried out for 20 minutes. The parameter which was varied in these numerical experiments is the environmental rotation. Angular velocities of 0, 0.001, 0.0025, 0.005, 0.01, and 0.02 rad sec^{-1} were used. These runs will be denoted as runs 1 through 6 respectively for the remainder of this discussion. Runs 1, 3, 4, and 5 were analyzed in detail. Runs 2 and 6 were made to study the vortex which is generated by a convective element rising in a rotating medium.

The general structure of the convective elements can be observed by referring to Figures 18 through 22. These figures represent the temperature, streamfunction, and velocity fields at different times during the thermal growth. The most striking contrast can be seen in the shape of the thermal. This can be best shown in Figure 18 which shows the temperature excess at various times after thermal rise and for various rotation rates. The nonrotating case, run 1, has the typical thermal cap shape throughout its growth, although the buoyant mass accentuates this cap effect more and more as it grows. The other runs illustrated show the effect of rotation causing the convective element to become more and more cylindrical as the rotation rate increases. This cylindricity is evidenced in the laboratory as well (see for example Figure 2 which contrasts the rotating and nonrotating laboratory models).

Figure 19 shows the streamfunction at five, ten and fifteen minutes after thermal release for angular velocities of 0.0, 0.0025, 0.005, and 0.01 rad sec^{-1}. In the nonrotating case, the streamfunction pattern does not change appreciably with time. This can be contrasted with the case for 0.0025 rad sec^{-1}. At five minutes after release, the streamfunction pattern has the same shape as the nonrotating case; the center value is reduced, however. After 10 minutes, the pattern is elongated in the vertical and a region of weak counterflow begins to develop at some distance from the axis of rotation. After 15 minutes, the main center is still elongated but is much weaker. The region of counterflow has now extended inward to the axis of rotation. This counterflow is responsible in part for the vertical stretching of the thermal structure for the rotating case. It can also explain some of the experimental observations of McCarthy (1967) and McIntyre (1967). In studying laboratory models of rotation convection, they frequently observed a portion of the cloud material being drawn downward around the central vortex shortly after the thermal was released. The elongation of the streamfunction pattern also helps explain the cylindrical shape of the rotation cloud.

The suppression of the circulation, the elongation of the stream pattern and the counterflow described above is even more evident in the 0.005 and 0.01 rad sec^{-1} cases. In these, alternate cells of positive and negative meridional vorticity are seen to be generated. This would tend to be confirmed by the observations of Turner (1963) who experimentally discovered adjacent regions of updrafts and downdrafts around a buoyant driven vortex. McCarthy and McIntyre also observed what they termed a "cylindrical stratification" to exist after their experimental thermals were released in a rotating field.

An examination of Figure 21, which shows the inflow, outflow, structure in the vicinity of the thermal, and Figure 20, the vertical velocity, serves to illustrate the Proudman-Taylor theorem (Chandrasekhar, 1961). This theorem states that the effect of a rotational field is to restrict the motion to a plane perpendicular to the axis of rotation. Thus, we would expect the greater rotational velocities to restrict the vertical velocities and consequently the inflow-outflow in the vicinity of the thermal. This is indeed the case in these numerical experiments.

Figures 23 through 29 show time histories of various meteorological parameters associated with the internal circulation of the thermal element. It is, in some respects, a measure of the strength of the toroidal circulation of the convective element. This parameter clearly shows the suppression which the environmental vorticity exerts on the convective process. It is interesting to note that the maximum streamfunction for run 3 does not depart significantly from the nonrotating run until about five minutes after thermal release. The departure is then quite pronounced. As the rotation rate increases, this drastic departure occurs at times nearer the release time; three minutes for run 4 and two for run 5.

Figure 24, which illustrates the maximum vertical velocity within the convective mass, again shows suppression of convection as the rotational velocity increases. Here, too, the values of vertical velocities for the rotating runs are the same as for the nonrotating runs for the first few minutes of the thermal growth. The vertical velocities begin to depart radically from the nonrotating run at about the same times that this departure was observed for the maximum value of streamfunction. This is to be expected, since the streamfunction defines both the vertical and radial velocities.

Figures 25 and 26 represent time histories of the maximum inflow and outflow in the vicinity of the thermals. As in the case of both the streamfunction and vertical velocities, the increase in the environmental vorticity causes a suppression of these measures of convection.

Figure 27 shows how the maximum temperature excess within the thermal varies as the convective element rises. For all runs, the value of the maximum temperature excess decreases with time, but the amount of decrease is smaller for the rotating runs than for the nonrotating run. This is a direct consequence of the reduced horizontal spreading of the convective element under the increased environmental angular velocities. In this adiabatic case, the total heat is conserved, and consequently the smaller thermal would result in larger values of potential temperature excess.

One of the most interesting features of this series of adiabatic numerical experiments is the behavior of the small scale vortex which is created by the convective element rising in the rotating fluid. The internal circulation generated by the rising element causes an inflow to occur below the thermal, and the conservation of angular momentum in the fluid drawn inward toward the axis of the thermal causes an increase in tangential velocity, thereby creating a small scale, vertical vortex. Figure 28 shows the time history of the tangential velocity excess of the five rotating runs. This velocity excess is found by subtracting the initial tangential velocity due to the solid rotational field from the total tangential velocity resulting from the concentrating of vorticity in the process of thermal growth. This figure depicts the maximum tangential excess observed in the sub-thermal vortex region. In all cases this value increases with time until a maximum value is reached and then either levels off or decreases. The maximum value of tangential excess is generally reached at an earlier time as the rotation rate increases. <u>This could be interpreted as a tendency for the rotational field to dominate the thermal growth</u>. Of the numerical experiments performed, run 3 with a value of angular velocity equal to 0.0025 rad sec^{-1} shows the maximum value of tangential excess occurring approximately 12 minutes after thermal release. Run 2, with Ω = 0.001 rad sec^{-1} and run 4, with Ω = 0.005 rad sec^{-1} both showed lower values of the peak tangential excess obtained during the forecast period. (Even though computational instability was becoming a problem, run 2 was extended for a 20 minute forecast in order to verify that a peak in tangential excess had occurred.) Runs 5 and 6 showed a continued suppression of tangential excess as the ambient angular velocity was increased. This amplification of the tangential velocity is a function of the radial distance through which the environmental air is entrained. As the rotation increases in the ambient fluid and the internal circulation of the thermal is suppressed, the inflow decreases and therefore the ability for the thermal to create a strong vortex is reduced. This leads to the speculation that there may be combinations of buoyancy and ambient vorticity which maximize the probability of vortex formation. This is indeed an area which deserves further investigation, but which is beyond the scope of this paper.

Figure 29 compares the vertically averaged tangential velocity excess for the small-scale vertical vortex that exists below the thermals in runs 4 and 5. The profiles shown are for 5, 10 and 15 minutes after thermal release. The 5-minute profiles show the effect of the initial entrainment of environmental air and the consequent increase in tangential velocity for distance out to 800 to 1000 meters from the axis of rotation. As the process of thermal growth continues until 10 minutes from thermal release, the velocity excess at the grid point closest to the axis of rotation increases in both cases. However, the increase is most evident in the profile for run 4 which represents the lower rotation of the two cases illustrated. At 15 minutes after thermal release, the profile for run 4 has begun to decrease, consistent with the maximum tangential velocity excess behavior exhibited in Figure 28. The velocity excess for run 5 increases slightly in the period from 10 to 15 minutes at a distance of 200 meters from the axis of rotation, but generally decreases further out from the origin. In both cases, the velocity profiles tend to approach the characteristic free vortex hyperbolic profile. This figure, therefore, graphically illustrates the ability of a convective element to concentrate the vorticity which is present in a fluid in solid rotation.

In summary it can be seen that for the case of adiabatic thermals the presence of a rotating environment causes a suppression of the convective process. This is evidenced by a reduction of the strength of the toroidal circulation within the thermal. This suppression by rotation is manifest by a reduction in the maximum value of the streamfunction, along with the attendant reduction in vertical and radial velocities.

In addition to the change in the strength of convection, the shape of the thermal is also influenced strongly by the ambient rotational field. As the ambient vorticity increases, the thermal structure becomes more and more cylindrical in shape. A region of counterflow develops near the lower portion of the rotating thermal element which results in pulling the lower portion of the cloud downward and outward. The rotating thermal is capable of generating a vortex structure below the cloud element. The vortex strength is not, apparently, a monotonic increasing function of the ambient vorticity, but instead seems maximized at some combination of buoyancy strength and ambient vorticity.

Non-Adiabatic Experiments

Two series of non-adiabatic numerical experiments were conducted. These series differed by the amount of buoyancy production; the first having a buoyancy production rate of five percent per minute, the second 10 percent per minute. In each series, experimental runs were made for several different values of rotation rate. The individual runs are identified by run number, rotation rate, and buoyancy production in Table III.

For the five percent per minute production rate, Figure 30 illustrates the temperature structure of the convective element at times of 5, 10 and 15 minutes after thermal release. This figure can be compared with Figure 18 which represents the same parameter for the adiabatic case. The primary result of this comparison is the conclusion that the non-adiabatic system is more vigorous and results in a faster growing thermal element. In addition, the tendency toward cylindricity of the thermal structure as rotation increases, although evident in the non-adiabatic case, is not as strong as this same tendency in the adiabatic case. The 'thermal cap' structure is still quite evident for the nonrotating run, and, although partially masked by the cylindrical effects of rotation, does become noticeable here for the rotating runs. The effect of buoyancy production in changing the shape of the thermal pattern is evidenced by a consideration of the spread of the thermal with height, equivalent to the entrainment coefficient α discussed in the previous chapters. The values of this coefficient (essentially the tangent of the half-angle swept out by the rising thermal) are given in Table III along with the rest of the pertinent experimental parameters. These values were computed from the observed spread of the thermal element as it rises. In run 7, the nonrotating case, the value of α was observed to be 0.28. As the rotation increased, α became 0.25 for run 8, 0.2 for run 9 and was near zero for run 10. The value of 0.2 for α is consistent with the results of previous researches dealing with nonrotating convective elements (Woodward 1959, Turner 1963).

Figure 31, the time history of the maximum value of streamfunction in the vicinity of the thermal, again shows a definite suppression of the internal circulation of the convective element as the rotation of the ambient fluid is increased. When contrasted with the adiabatic case, Figure 23, two interesting differences were noted. In the adiabatic case, those experiments with angular velocity 0.005 and 0.01 rad sec^{-1} were definitely dominated by the rotational field. The maximum value of the streamfuction initially increased and then leveled off without subsequent growth. For these same ambient angular velocity fields, the streamfunction in the non-adiabatic case continued to increase throughout the forecast period although not at the initial growth rate. The second major difference in these two figures is the degree of suppression for the same angular velocities. When the values of streamfunction at 15 minutes after thermal release are used as an indication of the degree of suppression, a rotational speed of 0.0025 rad sec^{-1} results in reduction of Ψ_m (maximum value of streamfunction) to 51 percent of its value in the nonrotating adiabatic case. The value of Ψ_m for the non-adiabatic case is reduced only to 65 percent of its nonrotating value. This lesser degree of suppression is further evidenced for angular velocities of 0.005 and 0.01 rad sec^{-1}. In the former case the maximum value of Ψ_m is reduced to 24 percent of its nonrotating value for the adiabatic experiment and only 29 percent for the non-adiabatic case. The latter case shows a reduction to 16 percent for the adiabatic run as compared to 19 percent for the non-adiabatic experiment.

Figures 32, 33, and 34, which show the time histories of vertical velocity, inflow and outflow, respectively, again show the increased suppression of convection as the angular velocity of the environmental air increases. The general increase in values of these parameters as the thermal grows is a characteristic of the buoyancy production in these non-adiabatic experiments, and is emphasized for the case of zero ambient rotation.

Figure 35 shows the time history of the maximum value of potential temperature excess within the thermal element. Again, as in the case of the adiabatic experiments, the maximum temperature excess is greater in the rotating cases than in those with no rotation. This is attributed to the concentration of buoyant material in a cylindrical column in a rotating medium as opposed to the spread and dilution encountered in the nonrotating case. One contrast between the adiabatic and the non-adiabatic case, however, is the increase in value of the maximum temperature excess after the first eight or nine minutes for the rotating non-adiabatic cases. It is apparent in these cases that the buoyancy production is causing the temperature to increase at a faster rate than the horizontal and vertical spreading causes a reduction in temperature.

The maximum tangential velocity excess is shown as a function of time in Figure 36. These non-adiabatic results have essentially the same characteristics as in the adiabatic experiments. The major exception is the behavior of the curve for run 10. In this run the tangential excess continues to increase during the forecast period, although after seven minutes the rate of growth is quite suppressed. (Recall that in the adiabatic run 5, the value of tangential excess remained essentially constant after seven minutes.) The maximum tangential excess for runs 8 and 9 occur at the same time after thermal release as for the corresponding angular velocities in the adiabatic cases. Figure 37 depicts the profile of tangential velocity excess which has been averaged vertically over the depth of the sub-thermal vortex. These profiles, shown for runs 9 and 10, demonstrate the concentration of ambient vorticity into a small high-vorticity region surrounded by a larger region whose velocity profile approaches that of an irrotational, or free, vortex. Although these average velocity profiles are essentially the same as those for the adiabatic case, the intensity of the vortex is greater. This is an expected consequence of the increased buoyancy of the non-adiabatic case.

Only three experiments were performed with the higher production rate of 10 percent per minute. These are designated as runs 11, 12 and 13 and correspond to angular velocities 0, 0.005 and 0.01 rad sec^{-1}, respectively. The structure of the temperature fields associated with these runs is shown in Figure 38. The values of α associated with these thermals were found to be 0.33, 0.25 and 0.2 for runs 11 through 13 respectively. Thus, with this higher buoyancy production rate, even the high rotation rate of 0.01 rad sec^{-1} exhibited a fair degree of horizontal spreading as the thermal rose. As the rotation rate increased, however, there was a definite suppression of the radial growth of the convective element.

Two additional results of the 10 percent per minute buoyancy production rate are presented in Figures 39 and 40. The maximum value of the streamfunction in the vicinity of the thermal (Fig. 39) is seen to increase with time for all angular velocities considered. Although the increased angular velocity does cause a decrease in the convectively generated circulation, the degree of suppression is not as great in this case as for either the case of 5 percent per minute production or the adiabatic situations.

Figure 40 depicts the maximum tangential excess obtained for runs 12 and 13. The shape of these curves is essentially the same as the corresponding curves for the lesser rate of buoyancy production. The local maximum attained for run 12 occurs at the same time after thermal release as do the maximum values of tangential excess for the corresponding value of angular velocity in the other two series of experiments. Similarly, the same timing of the change in rate of increase for run 13 is observed for both other series of experiments.

In summary, then, it can be seen that the principal effect of a rotational environment is the suppression of the growth of the non-adiabatic thermal elements studied in this series of experiments. The same conclusions concerning the behavior of the thermals may be drawn for either the adiabatic or non-adiabatic systems. There is one major exception to this statement, however, and that concerns the degree of suppression. As further evidenced in the next section which discusses the kinetic energy structure of the thermal, the degree of suppression is reduced as the buoyancy production increases.

This is confirmed by the experimental studies of McCarthy and McIntyre discussed in Chapter I. McIntyre's results for adiabatic thermals showed rotational suppression of the convective growth. McCarthy's non-adiabatic results demonstrated a definite rotational enhancement. It should be remarked that McCarthy's non-adiabatic thermals correspond to a buoyancy production rate of about 300 percent per minute, considerably higher than would be possible in the numerical model.

The lower degree of suppression for the non-adiabatic experiments can be related to the effective radius of entrainment discussed in Chapter II. Because of the greater radial growth experienced by the non-adiabatic thermals, one would expect the radius of entrainment to increase more rapidly with height for these thermals than for the adiabatic thermals. According to the model developed in Chapter II, the more the effective radius increases with height, the less suppression of convection by rotation is expected. In order to evaluate this effective radius of entrainment, trajectories were computed to determine the radial location of environmental fluid which was subsequently drawn into the thermal. The locus of the origins of these trajectories can then be used to define the vertical structure of the radius of entrainment. Some of the trajectory results are shown in Figure 41. It can be noted that in both the adiabatic and non-adiabatic cases, the effective radius of entrainment is considerably reduced when the thermal is growing in a rotating field. In the adiabatic example, the effective radius for the rotating fluid is constant with height. The increased buoyancy production in the rotating, non-adiabatic example shows a slight increase of the effective radius with height. Recall that the simple physical model in Chapter II predicted that an increase in the rate of growth of this effective radius would result in a lesser degree of suppression or a stronger enhancement of convection. This lesser degree of convective suppression is illustrated when the results of the adiabatic and non-adiabatic numerical models are compared. Thus there is a basic degree of consistency in the two theoretical approaches employed in this paper.

Energy Considerations

Studies of the energy transitions were made for some of the numerical experiments. These results are summarized in Figures 42 through 45. The transitions of potential to kinetic energy for runs 1, 3, 4, and 5 are shown in Figure 42. The only variable parameter among these runs was the angular velocity of the environmental fluid. Thus, the main conclusion is that the rate at which the potential energy of a buoyant mass is converted to the kinetic energy of motion is suppressed as the rotation rate increases. A graphical illustration of the exact degree of this suppression is given in Figure 43, which shows the degree of suppression of kinetic energy production as a function of both the angular velocity of the environmental fluid and buoyancy production rate. The curves for the adiabatic cases are presented as a percentage suppression of the kinetic energy using the nonrotating adiabatic runs as the standard. The non-adiabatic cases illustrated use the nonrotating run as a basis for the precentage suppression calculations. The non-adiabatic suppression curves are presented only for the 5 percent per minute buoyancy production rate. The percentage suppression is clearly seen to increase with increasing rotation rate. After 15 minutes, run 5 (0.01 rad sec^{-1}) is suppressed by 82 percent; run 4 (0.005 rad sec^{-1}) by 59 percent and run 3 (0.0025 rad sec^{-1}) is suppressed 29 percent. The corresponding non-adiabatic runs exhibit a 67 percent, 45 percent, and 20 percent suppression, markedly less than in the adiabatic case. The relative shapes of the curves appear to be quite similar, however.

For three of the four adiabatic runs illustrated in Figure 43, detailed energy budget studies have been made. In these, the total kinetic energy at each minute of the numerical computation was divided into three different portions. These consisted of the kinetic energy due to vertical velocities, radial velocities, and in the case of the rotating studies, the tangential velocities. In the rotating cases, the initial kinetic energy of the rotating field was subtracted from the final results, therefore indicating changes in the energy budget, as opposed to absolute values. These three fractions were then plotted in terms of the percentage of the total kinetic energy within the numerical grid and are depicted in Figures 44 and 45.

The results of nonrotating cases are demonstrated by the solid lines in Figures 44 and 45. These have been repeated in both figures for an ease in comparison. One minute after thermal release the vertical velocity accounts for 57 percent of the kinetic energy, and the remaining 43 percent is due to the radial velocities. As the thermal continues to grow, that portion of the kinetic energy due to the vertical velocity increases smoothly and monotonically until it amounts to 80 percent of the total.

A remarkable contrast is shown in run 4, 0.005 rad sec^{-1}. At one minute after thermal release, the distribution is the same as for the nonrotating case. The rotational energy is still negligible. Although the percentage of kinetic energy which is present in the tangential velocity is essentially negligible for the first three or four minutes, the rotational field has a marked effect on the energy distribution between the vertical and radial velocity components. At two and three minutes after thermal release, the vertical velocity is seen to account for a greater percentage of the kinetic energy than it did in the nonrotating case. This can be attributed to the suppression of the radial motion by the rotational field as evidenced by Figure 19. By five minutes after release, the percentage of kinetic energy contained in the tangential field is seen to be increasing at a rapid rate. This increase is at the expense of both the vertical and radial components. The vertical component lags a little behind the radial component in the decrease shown after five minutes, but the general shape of the two curves is similar. These two curves are out of phase with the tangential component. After the maximum is reached by the tangential component, it begins to drop, allowing the share of the kinetic energy contained in the vertical and radial velocity components to increase slightly. The last five minutes of the thermal growth gives the general impression of a damped oscillatory pattern with the radial component of kinetic energy approaching the same share of the kinetic energy as it had for the nonrotating case. The percentages of kinetic energy contained in the vertical and tangential components appear to approach each other. After 15 minutes, therefore, the percentage of energy contained in the radial component is approximately the same as in the nonrotating case. The percentage of energy contained in the nonrotating vertical component appears to be equally divided between the vertical and tangential components for the rotating case.

Figure 45 presents the energy budget for run 5, 0.01 rad sec^{-1}.

At this higher rotation rate, the conclusions tentatively drawn from Figure 44 become more apparent. Initially the vertical and radial components are the same as in the nonrotating case. At two and three minutes after release, the vertical component exceeds the nonrotating case. The tangential component begins to become important at an earlier time for this higher rotation rate, a strong increase being apparent at three and four minutes after thermal release. The tangential component has reached a maximum after five minutes and then begins a damped oscillatory motion. This maximum occurs at an earlier time than for the lower rotation rate shown in Figure 44. The value of the maximum is lower for this higher rotation rate. This result is consistent with those for the maximum tangential excess as shown in Figure 28. As in the 0.005 rad sec^{-1} case, the curves for the vertical and radial components are quite similar, and the tangential component is out of phase with the other components. The radial component approaches the nonrotating radial curve and is identical with it from 13 to 15 minutes after thermal release. The vertical and tangential components are quite nearly equal in magnitude.

CHAPTER IV

CONCLUSIONS

This paper attacks in detail the interaction between the toroidal circulation of the rising convective element and the environmental rotating field. This interaction has been investigated by using both simple physical models and complex numerical studies.

In a rotating field the consideration of angular momentum and energy conservation in fluid entrained into a rising convective element has led to a generalized buoyancy term. This effective buoyancy is seen to be a function of what is termed the static buoyancy (that buoyancy which would exist without the effects of rotation), the square of the angular velocity, the effective radius of entrainment, and the vertical variations of both the radius of the convective element and the effective radius of entrainment. The effective radius of entrainment may itself be a fuction of total buoyancy strength, angular velocity, and the stability of the environmental fluid. Since the square of the angular velocity enters the equation for effective buoyancy, it is the magnitude and not the direction of rotation which affects the growth of the convective elements.

The vertical profile of the radius of entrainment is still in question; however, the numerical model has given some insight into its behavior. In this theroetical study, several cases were examined. These are discussed in detail in the text of the paper (Chapter II).

The model which was developed by Morton, Taylor and Turner (1956) was modified to incorporate the general buoyancy term. The modification affected only the equations for the conservation of momentum, leaving the conservation equations for volume and density deficit unchanged. Through this method, the effect of rotation on both plumes and thermals could be investigated.

In satisfying the requirements of the simple physical model discussed in Chapter II, one of the most critical parameters is the effective radius of entrainment. If it increases rapidly while the thermal is growing, then the model predicts an enhancement of the convection by the rotational field. One expects from this model that the more vigorous the the toroidal circulation of the thermal, the greater is the effective radius of entrainment and consequently the greater the degree of rotational enhancement. In the laboratory studies of McCarthy and McIntyre, the non-adiabatic thermals appeared visually to have a much greater toroidal circulation than that observed in the adiabatic thermals. And, consistent with these observed differences in "vigor" of the convection and the arguments above, the non-adiabatic thermals were observed to be enhanced by rotational motion. The numerical model also tended to support this same finding. Even though all of the numerical experiments showed a suppression of the convective motion by rotation, the degree of suppression was less in the non-adiabatic thermals, which did show a more vigorous circula- when compared to the adiabatic thermals.

An analysis of the numerical results also explained other features of rotating convective elements as observed by McCarthy and McIntyre. In addition to the general cylindrical shape exhibited by the rotating thermals and the suppression of the convective motion, there developed shortly after thermal release a counter circulation below the main toroidal vortex. This counterflow caused lower portions of the thermal to be drawn down and around the central vortex which had formed. Divergence developed below the thermal and resulted in weakening the vertical vortex. This tendency for counterflow and associated vortex destruction was increased with increasing environmental rotation. The tendency for generating initially a strong vertical vortex is increased with increasing environmental rotation. The delicate balance between these two effects seems to account for the observed vortex strength maximizing at some intermediate rotation rate.

Attempts are now in progress to extend these concepts developed here to the atmospheric prototype. It is at best a complex task, involving meso- and micro-scale analysis of the environmental conditions of convective elements in the atmosphere. The natural extension of this work would be its application to the rotating severe storms. The limited work thus far in applying this type of analysis to severe storms (Giles, 1967) does lend some support to the idea of rotational enhancement of severe storms. However, a definite conclusion concerning the atmospheric prototype is not possible at this time.

BIBLIOGRAPHY

Barcilon, A., 1967 : Phase Space Solutions for Buoyant Jets. General Electric Space Science Lab., R 675D8, 34 pp.

Batchelor, G.K., 1954 : Heat convection and buoyancy effects in fluids. Quart. J. R. Meteor. Soc., 80, 339-358.

Chandrasekhar, S., 1961 : Hydrodynamic and hydromagnetic stability. Oxford at the Clarendon Press, 654 pp.

Friday, E.W. Jr., 1967 : Thermal Convection from Maintained and Instantaneous Sources of Buoyancy in a Rotating Field. Master's Thesis, University of Oklahoma, 66 pp.

Giles, J.D., 1967 : An Investigation of the Mesoscale Pattern Associated with Severe Storms. Master's Thesis, University of Oklahoma, 40 pp.

Inman, R.L., 1966 : The Evolution of Convective Motions in a Rotating Fluid. Doctoral Dissertation, Texas A and M University, 90 pp.

Kuo, H.L., 1966 : On the dynamics of convective atmospheric vortices. J. Atmos. Sci., 23, 25-42.

Lapidus, L., 1962 : Digital Computation for Chemical Engineers. McGraw-Hill, New York, 407 pp.

Levine, J., 1959 : Spherical vortex theory of bubble-like motion in cumulus clouds. J. Meteor., 16, 653-662.

Lilly, D.K., 1962 : On the numerical simulation of buoyant convection. Tellus, 14, 148-172.

__________, 1963 : Experimental generation of convectively driven vortices. Geofisica Internacional, 5, 43-48.

__________, 1964 : Numerical solutions for the shape-preserving two-dimensional thermal convection element. J. Atmos. Sci., 21, 83-98.

Long, R.R., 1956 : Sources and sinks at the axis of a rotating liquid. Quart. J. Mech. and Appl. Math., 9, 385-393.

__________, 1958 : Vortex motion in a viscous fluid. J. Meteor., 15, 108-112.

__________, 1961 : A vortex in an infinite viscous fluid. J. Fluid Mech., 11, 611-623.

Ludlum, F.H., 1963 : Severe local storms : A review. Meteor. Monographs, Vol. 8, Amer. Meteor. Soc., Boston, pp 1-30.

McCarthy, J., 1967 : Experiments with Simulated Penetrative Convection Elements in a Rotating Medium. Master's Thesis, University of Oklahoma, 45 pp.

McIntyre, J.R., 1967 : An Experimental Study of Adiabatic Thermals Rising in a Rotating Field. Masters Thesis, Univ. of Okla., 57 pp.

Morton, B.R., G.I. Taylor and J.S. Turner, 1956 : Turbulent gravitational convection from maintained and instantaneous sources. Proc. Roy. Soc., A, 234, 151.

Morton, B.R., 1957 : Buoyant plumes in a moist atmosphere. J. Fluid Mech., 2, 127.

____________, 1959 : The ascent of turbulent forced plumes in a calm atmosphere. Int. J. Air. Poll., 1, 184-197.

____________, 1963 : Model experiments for vortex columns in the atmosphere. Nature, 197, 840-842.

Ogura, Y., and N.A. Phillips, 1962 : Scale analysis of deep and shallow convection in the atmosphere. J. Atmos. Sci., 19, 173-179.

_________, 1962 : Convection of isolated masses of a buoyant fluid : A numerical calculation. J. Atmos. Sci., 19, 492-502.

_________, 1963 : The evolution of a moist convective element in a shallow conditionally unstable atmosphere: A numerical calculation. J. Atmos. Sci., 20, 407-424.

Richards, J.M., 1961 : Experiments on the penetration of an interface by buoyant thermals. J. Fluid Mech., 11, 369-384.

Sasaki, Y., and E.W. Friday Jr., 1967 : Thermal Convection from Maintained and Instantaneous Sources of Buoyancy in a Rotating Field. Univ. of Okla. Research Institute Report ARL-1515-1, 66 pp.

Sasaki, Y., E.M. Wilkins, E.W. Friday Jr., 1968 : Behavior of convective elements in a rotating medium, Final Report on NSF Grant GP-1561. Univ. of Okla. Atmos. Res. Lab. Report ARL-1524-5, January, 1968, 117 pp.

Scorer, R.S., and F.H. Ludlum, 1953 : Bubble theory of penetrative convection. Quart. J.R. Meteor. Soc., 79, 94.

Scorer, R.S., and C. Ronne, 1956 : Experiments with convection bubbles. Weather, 11, 151.

Scorer, R.S., 1957 : Experiments on convection of isolated masses of buoyant fluid. J. Fluid Mech., 2, 583-594.

Squires, P., and J.S. Turner, 1962 : An entraining jet model for cumulonimbus updraughts. Tellus, 14, 422-434.

Telford, J.W., 1966 : The convective mechanism in clear air. J. Atmos. Sci., 23, 652-666.

Telford, J.W. and J. Warner, 1967 : Convection below cloud base. J.Atmos. Sci., 24, 374-382.

Thompson, P.D., 1961 : Numerical Weather Analysis and Prediction, Macmillan, New York.

Turner, J.S., 1963 : Model experiments relating to thermals with increasing buoyancy. Quart. J.R. Meteor. Soc., 89, 62-74.

Turner, J.S., 1964 : The dynamics of spheroidal masses of buoyant fluid. J. Fluid Mech., 19, 481-490.

Turner, J.S. and D.K. Lilly, 1963 : The carbonated water tornado vortex. J. Atmos. Sci., 20, 468-471.

Wilkins, E.M., 1964 : The role of electrical phenomena associated with tornadoes. J. Geophys. Research, 69, 2435-2447.

Wilkins, E.M., 1967 : Interactions of Successive Buoyant Elements with a Rotating Medium, Univ. of Okla. Atmos. Research Lab. ARL-1524-6, 11 pp.

Wilkins, E.M., Y. Sasaki, E.W. Friday, J. McCarthy, and J.R. McIntyre, 1967, Properties of Simulated Thermals in a Rotating Fluid. Univ. of Oklahoma Atmos. Res. Lab. Report ARL-1524-2, 28 pp.

Wilkins, E.M., Y. Sasaki, R.L. Inman, and J. McCarthy, 1966 : Laboratory Investigations of Vortex Formation by Simulated Thermals. Univ. of Okla. Res. Inst. Report ARL-1524-1 (NSF Grant GP-5161) October, 1966, 20 pp.

Woodward, B., 1959 : The motion in and around isolated thermals. Quart. J.R. Meteor. Soc., 85, 144-155.

APPENDIX A

THE NUMERICAL MODEL FOR SHALLOW CONVECTION

The Basic Equations

A set of equations suitable for the study of shallow convection has been developed by Ogura and Phillips (1962). This set of equations with modifications to take into account the tangential velocity field caused by the environmental rotation is utilized for the following numerical model. The equations described below are valid for dry, inviscid, shallow convection. Although moist convection is not analyzed explicitly, a modification of the numerical model to allow for buoyancy production permits the study of a buoyancy production term. This will be discussed later in this Appendix.

For axially-symmetric motion, the basic equations defining the motion may be written in cylindrical coordinates as follows:

$$\frac{\partial u}{\partial t} = -u\frac{\partial u}{\partial r} - w\frac{\partial u}{\partial r} - c_p \Theta \frac{\partial \pi'}{\partial r} + \underline{\underline{\frac{v^2}{r}}} \qquad \text{A.1}$$

$$\underline{\underline{\frac{\partial v}{\partial t} = -u\frac{\partial v}{\partial r} - w\frac{\partial v}{\partial z} - \frac{uv}{r}}} \qquad \text{A.2}$$

$$\frac{\partial w}{\partial t} = -u\frac{\partial w}{\partial r} + w\frac{\partial w}{\partial z} - c_p \Theta \frac{\partial \pi'}{\partial z} + g\frac{\theta}{\Theta} \qquad \text{A.3}$$

The underlined terms have been added to the Ogura and Phillip's equations to allow for the effects of the tangential motion. The thermodynamic equation may be written:

$$\frac{\partial\theta}{\partial t} = -u\frac{\partial\theta}{\partial r} - w\frac{\partial\theta}{\partial z} \qquad \text{A.4}$$

And the continuity equation becomes:

$$\frac{\partial ru}{\partial r} + \frac{\partial rw}{\partial z} = 0 \qquad \text{A.5}$$

In the above equations, u, v, and w are the radial, tangential, and vertical components of velocity respectively. The specific heat at constant pressure is denoted by c_p, θ is the potential temperature anomaly from a dry adiabatic atmosphere, with a reference potential temperature, Θ, and the acceleration of gravity is denoted by g. The pressure p enters the equations through the non-dimensional variable π such that

$$\pi = \left(\frac{p}{P}\right)^{R/c_p} \qquad \text{A.6}$$

where R is the gas constant for dry air and P is a constant reference pressure. The term π' represents the deviation of π from that of a dry adiabatic atmosphere with constant potential temperature.

The r-z grid to be employed in this study consists of a vertical slice through the axis of symmetry and extending from r = 0 to r = L and from z = 0 to z = H. Thus the model that is being developed represents a cylinder of air of radius L and height H.

The boundary conditions to be used at the top and bottom surfaces for the purposes of this finite difference model are

$$w = 0,\ \frac{\partial u}{\partial z} = 0,\ \frac{\partial v}{\partial z} = 0 \quad \text{at } z = 0 \text{ and } H \qquad \text{A.7}$$

For the vertical boundary at $r = L$, the condition becomes

$$u = 0,\ \frac{\partial w}{\partial r} = 0 \quad \text{at } r = L \qquad \text{A.8}$$

At the center of the convective element, $r = 0$, the appropriate boundary conditions are

$$\frac{\partial u}{\partial r} = 0,\ u = 0,\ v = 0 \quad \text{at } r = 0 \qquad \text{A.9}$$

Also, since axial symmetry is being assumed, the first derivative with respect to r at $r = 0$ of all variables will be zero at all time. The potential temperature derivation θ is required to be constant at $r = L$, $z = 0$, and $z = H$.

For the purpose of numerical computations, it is useful to introduce the streamfunction, Ψ, defined by

$$u = -\frac{1}{r}\frac{\partial \Psi}{\partial z}\ ;\ w = \frac{1}{r}\frac{\partial \Psi}{\partial r} \qquad \text{A.10}$$

This automatically satisfies the continuity equation (A.5).

The pressure deviation π' may be eliminated from A.1 and A.3 by cross differentiating and introducing the horizontal vorticity, η. Thus, the vorticity equation becomes:

$$\frac{\partial \eta}{\partial t} = -u\frac{\partial \eta}{\partial r} - w\frac{\partial \eta}{\partial z} + \eta\frac{u}{r} - \frac{1}{r}\frac{\partial v^2}{\partial z} + \frac{g}{\Theta}\frac{\partial \theta}{\partial r} \qquad \text{A.11}$$

where

$$\eta \equiv \frac{\partial w}{\partial r} - \frac{\partial u}{\partial z} = \frac{1}{r}\left[\frac{\partial^2 \Psi}{\partial r^2} - \frac{1}{r}\frac{\partial \Psi}{\partial r} + \frac{\partial^2 \Psi}{\partial z^2} \right] \qquad \text{A.12}$$

The boundary conditions may now be restated in terms of Ψ and η.

$$\Psi = 0 \; ; \; \eta = 0 \text{ at } r = 0, L \text{ and } z = 0, H \qquad \text{A.13}$$

The model consists of a complete set of equations in Ψ, η, θ and v. Initial fields of Ψ, θ, and r are specified. The initial vorticity η can be determined from A.12. The prognostic variables for time extrapolation are η, θ, and v. The equation set comprised of (A.2), (A.4), and (A.11) is used to predict values of v, θ, and η at a later time, $t + \Delta t$. The diagnostic variable Ψ is then computed by relaxing the vorticity field using (A.12). The relaxation techniques employed for this equation are discussed in a later section. This completes one step of the computation procedure. The process is then repeated. The finite difference equations employed for the time extrapolation are indicated below.

The Finite Difference Equations

The r - z plane under consideration for this model has the dimensions L by H. For ease of computation, the grid is constructed by dividing this plane into 200 meter squares. Thus $\Delta r = \Delta z = d = 200$ meters. The value of the radius and height for any grid point is

$$\begin{aligned} r &= (i-1)d \; ; \; i = 1,2,\ldots,I \\ z &= (k-1)d \; ; \; k = 1,2,\ldots,K \\ L &= (I-1)d \\ H &= (K-1)d \end{aligned} \qquad \text{A.14}$$

Thus I and K represent the upper limits of grid index numbers in the r and z directions respectively. The variables are defined at each grid point in this model.

A two-step Lax-Wendroff intregration scheme (Richtmyer, 1963) is used for this study. For the purpose of illustration, consider the following simple equation

$$\frac{\partial U}{\partial t} = - \frac{\partial G(U)}{\partial r}$$

where U is a function of r and t and G(U) is some function of U. Standard finite difference notation will be used, thus U(r,t) will be written as U_i^n where $t = n\Delta t$. The Lax-Wendroff scheme consists of two difference equations which are applied at alternate time steps. The finite difference forms for the equation above becomes

$$U_i^{n+1} = \frac{U_{i+1}^n + U_{i-1}^n}{2} - \frac{\Delta t}{2d} (G_{i+1}^n - G_{i-1}^n)$$

$$U_i^{n+2} = U_i^n - \frac{\Delta t}{d} (G_{i+1}^{n+1} - G_{i-1}^{n+1})$$

Thus, in essence, the finite difference equation for step one of the L - W scheme is a forward time difference, centered space difference formulation of the equation. This formulation generates a preliminary estimate of the prognostic field which is then used for the "leap-frog" scheme which is represented by the second equation in the L - W method. Notice that in the first step equation, the initial value of the variable is estimated by the average of the surrounding values, whereas in the second time step, the actual parameter value at the grid point is utilized.

In the following discussion, both of the finite difference equations will be generated and the variables will be non-dimensionalized at the same time. Thus the arbitrary U may be written $U = U^* U'$ where U^* is the characteristic value of U and carries its dimensions. The variable U' is now non-dimensional and of the order of 1. The primes will not be used in the following equations for simplicity of notation. It should be remembered that the prognostic and diagnostic variables appearing in the following finite difference equations are non-dimensional.

The advection terms in the prognostic equations may, with the use of the continuity equation, be rewritten in flux form as follows:

$$\frac{1}{r}\left[\frac{\partial}{\partial r}\left(u\frac{\partial \Psi}{\partial z}\right) - \frac{\partial}{\partial z}\left(u\frac{\partial \Psi}{\partial r}\right)\right]$$

If the finite difference form of this term is denoted by $A(U)_{ik}$, then

$$\begin{aligned} A(U)_{i,k} = \frac{\Psi^*}{4(i-1)d^3} [&U_{i+1,k} (\Psi_{i+1,k+1} - \Psi_{i+1,k-1}) \\ &-U_{i-1,k} (\Psi_{i-1,k+1} - \Psi_{i-1,k-1}) \\ &-U_{i,k+1} (\Psi_{i+1,k+1} - \Psi_{i-1,k+1}) \\ &+U_{i,k-1} (\Psi_{i+1,k-1} - \Psi_{i-1,k-1} \end{aligned} \qquad \text{A.15}$$

The average value of the surrounding points is given by

$$\overline{U}_{i,k} = \frac{1}{4} (U_{i+1,k} + U_{i-1,k} + U_{i,k+1} + U_{i,k-1}) \qquad \text{A.16}$$

Using these definitions, the first step equations of the L - W formulation become

$$v_{i,k}^{n+1} = \bar{v}_{i,k}^{n} + \Delta t\ A(v)_{i,k}^{n} + \frac{\Delta t\Psi^{*}}{2(i-1)^{2}d^{3}}\ v_{i,k}^{n}\ (\Psi_{i,k+1}^{n} - \Psi_{i,k-1}^{n}) \qquad \text{A.17}$$

$$\theta_{i,k}^{n+1} = \bar{\theta}_{i,k}^{n} + \Delta t\ A(\theta)_{i,k}^{n} \qquad \text{A.18}$$

$$\eta_{i,k}^{n+1} = \bar{\eta}_{i,k}^{n} + \Delta t\ A(\eta)_{i,k}^{n} - \frac{\Delta t\Psi^{*}}{2(i-1)^{2}d^{3}}\ \eta_{i,k}^{n}\ (\Psi_{i,k+1}^{n} - \Psi_{i,k-1}^{n}) - \frac{\Delta t v^{*2}}{2d^{2}\eta^{*}(i-1)}\ [(v_{i,k+1}^{n})^{2} - (v_{i,k-1}^{n})^{2}] + \frac{\Delta t g}{2d\eta^{*}\Theta}\ (\theta_{i+1,k}^{n} - \theta_{i-1,k}^{n}) \qquad \text{A.19}$$

These equations are valid only at the internal grid points and not on the boundary. Thus the (i-1) term in the denominator of several terms does not pose a problem.

The difference equations for the second time step of the Lax-Wendroff method can now be written as

$$v_{i,k}^{n+2} = v_{i,k}^{n} + 2\Delta t\ A(v)_{i,k}^{n+1} + \frac{\Delta t\Psi^{*}}{(i-1)^{2}d^{3}}\ v_{i,k}^{n+1}\ (\Psi_{i,k+1}^{n+1} - \Psi_{i,k-1}^{n+1}) \qquad \text{A.20}$$

$$\theta_{i,k}^{n+2} = \theta_{i,k}^{n} + 2\Delta t A(\theta)_{i,k}^{n+1} \qquad \text{A.21}$$

$$\eta_{i,k}^{n+2} = \eta_{i,k}^{n} + 2\Delta t A(\theta)_{i,k}^{n+1} - \frac{\Delta t\Psi^{*}}{(i-1)^{2}d^{3}}\ \eta_{i,k}^{n+1}\ (\Psi_{i,k+1}^{n+1} -$$

$$\Psi^{n+1}_{i,k-1}) - \frac{\Delta t v^{*2}}{d^2 \eta^*(i+1)} [(v^{n+1}_{i,k+1})^2 - (v^{n+1}_{i,k-1})^2] +$$

A.22

$$\frac{\Delta t g}{d\eta^* \Theta} (\theta^{n+1}_{i+1,k} - \theta^{n+1}_{i-1,k})$$

Boundary Conditions

Only two parameters offer any real difficulty in establishing the boundary conditions; θ and v. The vertical boundary at r = L is the simplest in this model since all the parameters are held constant at all times. The value of the streamfunction Ψ is held constant on all boundaries. The vertical boundary at r = 0 must be handled in a manner to permit the value of potential temperature to change with time. At this position, the thermodynamic equation reduces to

$$\frac{\partial \theta}{\partial t} = -w \frac{\partial \theta}{\partial z} \qquad \text{A.23}$$

since $\frac{\partial \theta}{\partial r} = 0$ at r = 0. The vertical velocity, w, is evaluated by

$$w = \frac{1}{r} \frac{\partial \Psi}{\partial r}$$

which is indererminate at r = 0 since $\frac{\partial \Psi}{\partial r} = 0$ at r = 0. Therefore, in the limit,

$$w = \frac{\partial^2 \Psi}{\partial r^2} \text{ at } r = 0 \qquad \text{A.24}$$

On this boundary, therefore, the first step of the L - W method is

$$\theta^{n+1}_{1,k} = \frac{1}{2} (\theta^n_{1,k+1} + \theta^n_{1,k-1}) - \frac{\Delta t \Psi^*}{d^3} \Psi^n_{2,k} (\theta^n_{1,k+1} - \theta^n_{1,k-1}) \qquad \text{A.25}$$

Step 2 becomes

$$\theta^{n+2}_{1,k} = \theta^{n}_{1,k} + \frac{2\Delta t\Psi^{*}}{d^{3}} \Psi^{n+1}_{2,k} (\theta^{n+1}_{1,k+1} - \theta^{n+1}_{1,k-1})$$

The value of θ is held constant on the top and bottom surfaces, but the tangential motion must be allowed to vary. The equation for the tangential motion at the boundaries reduces to

$$\frac{\partial v}{\partial t} = -u\frac{\partial v}{\partial r} - \frac{uv}{r} \qquad \text{A.26}$$

since $w = 0$ at $z = 0$ and H. At the lower boundary, the appropriate L - W finite difference equation becomes

$$v^{n+1}_{i,1} = \frac{1}{2} (v^{n}_{i+1,1} + v^{n}_{i-1,1}) + \frac{\Delta t\Psi^{*}}{2d^{3}(i-1)} \Psi^{n}_{i,2} (v^{n}_{1+1,1} - v^{n}_{i-1,1} + \frac{2}{i-1} v^{n}_{i,1}) \qquad \text{A.27}$$

At $Z = H$, we have

$$v^{n+1}_{i,K} = \frac{1}{2} (v^{n}_{i+1,K} + v^{n}_{i-1,K}) - \frac{\Delta t\Psi^{*}}{2d^{3}(i-1)} \Psi^{n}_{i,K-1}(v^{n}_{i+1,K} - v^{n}_{i-1,K} + \frac{2}{i-1} v^{n}_{i,K}) \qquad \text{A.28}$$

The finite difference equations for the second step in the L - W scheme follow directly from A.27 and A.28.

Initial Conditions

The initial conditions used in the first series of experiments essentially simulated the release of a small mass buoyant air near the bottom of a cylinder of fluid which was either stationary, or in solid rotation. Following Ogura (1963), the temperature was given by

$$\theta(r,z) = \theta_o \sin\left(\frac{\pi z}{600}\right) \exp\left\{-\left(\frac{r}{320}\right)^2\right\}$$

$$0 \leq z \leq 600 \qquad \text{A.29}$$

$$0 \leq r \leq 300$$

$$\theta(r,z) = 0 \text{ elsewhere}$$

In this expression, θ_o is the maximum temperature excess at the center of the buoyant element, and z and r are given in meters. The potential temperatures were truncated to zero if the computed value was less than 10^{-4} °C. This was done to minimize the possibility of floating point underflow during the numerical integration.

Initially, all motion in the r - z plane was zero. This was easily achieved by setting the streamfunction Ψ and the horizontal vorticity η equal to zero at all points in the finite difference grid. When the thermal was to be released in a nonrotating field, the value of the tangential velocity, v, was set equal to zero at all mesh points. The rotational effects were studied in a cylinder which was considered in solid rotation. In this case then,

$$v_\theta(r) = \Omega r$$

where Ω is the angular velocity and r is the distance from the origin. Thus the finite difference form for the initialization of the tangential velocity field is simply

$$v_{i,k} = \Omega d(i-1) \text{ for all } k \qquad \text{A.30}$$

These conditions are established and the time extrapolation starts at $t = 0$. This causes the motion field to be generated by the rising buoyant element, and, as discussed in Chapter I represents a point source thermal. The model used for this study was generalized to allow any initial temperature field to be introduced at $t = 0$. This permitted a large variety of thermal shapes to be studied. In addition, however, it allowed the introduction of a continuous heat source. The temperature at the lower boundary, $z = 0$, is not changed as the time extrapolation progresses. Thus, this boundary can serve as a source of heat for a plume-like model.

The production of buoyancy during the cloud growth is permitted in this model. This production is not a direct simulation of latent heat, as occurs in the atmosphere, but rather a simple buoyancy production which is proportional to the potential temperature excess at the time. In essence, after a forecast of θ has been made, it is modified by

$$\theta^n_{i,k} = \theta^n_{i,k} \, (1 + \varphi) \qquad \text{A.31}$$

where φ is a small value by which the potential temperature is increased. This modelling of the buoyancy production was chosen for its simplicity since the rotational effects, and not the latent heat release mechanism, was under investigation in this model.

An additional feature of this model permits the release of a second model into the wake of the first. The provision is made, that at any time after the initial thermal has been released, a thermal with any general configuration can be introduced into the model. This was done to investigate the nature of a thermal rising in the vortex pattern that had been established by the initial buoyant element. Such a study was indicated by the simple physical model proposed by Wilkins (1967) for successive thermal releases.

Relaxation Techniques for the Vorticity Equation In Cylindrical Coordinate System

The horizontal component of vorticity as used in this model is given by

$$\eta = \frac{1}{r}\left[\frac{\partial^2\Psi}{\partial r^2} - \frac{1}{r}\frac{\partial\Psi}{\partial r} + \frac{\partial^2\Psi}{\partial z^2}\right] \qquad \text{A.32}$$

The r-z plane is a vertical cross section through the axis of symmetry of the convective element, z being the height above the surface and r being the distance from the vertical axis of symmetry.

Using differencing notation of $O(h^2)$ this can be written in finite difference form as

$$\eta_{i,j} = \frac{1}{r_i}\left[\frac{\Psi_{i+1,j} + \Psi_{i-1,j} - 2\Psi_{i,j}}{(\Delta r)^2} - \right.$$

$$\left.\frac{1}{r_i}\left(\frac{\Psi_{i+1,j} - \Psi_{i-1,j}}{2\Delta r}\right) + \frac{\Psi_{i,j+1} + \Psi_{i,j-1} - 2\Psi_{ij}}{(\Delta h)^2}\right] \qquad \text{A.33}$$

Now let $\Delta r = \Delta h = d$. Therefore

$$r_i = d(i-1) \qquad \text{A.34}$$

When A.33 is simplified for this even grid spacing, it becomes

$$\eta_{i,j} = \frac{1}{d^3 i}\left[(1-\frac{1}{2i})\Psi_{i+1,j} + (1+\frac{1}{2i})\,\Psi_{i-1,j} + \right. \qquad \text{A.35}$$

$$\left. \Psi_{i,j+1} + \Psi_{i,j-1} - 4\Psi_{i,j}\right]$$

It can be noted here, that when i becomes large, $\frac{1}{2i} < 1$, and the expression within the brackets approaches the standard cartesian coordinate form of the finite difference form of vorticity. It would therefore appear logical that standard relaxation techniques would be appropriate for the solution of this equation for large values of i.

Equation A.35 may be solved for $\Psi_{i,j}$ as follows

$$\Psi^{(n+1)}_{i,j} = \{d^3 i\eta_{i,j} - [(1-\frac{1}{2i})\,\Psi^{(n)}_{i+1,j} + (1+\frac{1}{2i})\,\Psi^{(n+1)}_{i-1,j} + \qquad \text{A.36}$$

$$\Psi^{(n)}_{i,j+1} + \Psi^{(n+1)}_{i,j-1}]\} \;/\; 4$$

and this formulation would represent the Gauss Seidel relaxation formula. However, because of the success and efficiency experienced in the use of the Liebmann relaxation or successive over-relaxation (SOR) routines for cartesian coordinates, it was decided to perform a series of experiments with this technique.

Here

$$\Psi^{(n+1)}_{i,j} = \Psi^{(n)}_{i,j} + \{(1-\frac{1}{2i})\,\Psi^{(n)}_{i+1,j} + (1+\frac{1}{2i})\,\Psi^{(n+1)}_{i-1,j} + \qquad \text{A.37}$$

$$\Psi^{(n)}_{i,j+1} + \Psi^{(n+1)}_{i,j-1} - 4\Psi^{(n)}_{i,j} - d^3 i\eta_{i,j}\}\,\frac{\omega}{4}$$

where ω is the over-relaxation parameter and has been shown to be equal to 1.73 for a square grid in cartesian coordinates.

A series of numerical tests was run to determine the optimum over-relaxation parameter for A.37 as a function of grid size and shape. Initially square grids were used of size (5x5), (10x10), (15x15), (20x20) and (25x25). A maximum of 50 iterations was permitted for convergence. An arbitrary vorticity field was generated and the algorithm indicated by A.37 was used to calculate the associated streamfunction.

Note (Table IV) that for the 5x5 grid the best results were obtained with $\omega = 1$, or no over-relaxation. This corresponds to the Gauss Seidel formulation given by (A.36) and shows that there is no advantage in the SOR algorithm (in fact, a disadvantage, due to increased execution time). As the grid size increases, the value of the optimum over-relaxation parameter increases steadily until the 25x25 grid, the value of ω optimum is essentially that for a cartesian coordinate system, 1.73. This is what one would expect as the 1/2i terms become small in comparison to 1.

An additional experiment was run with 25 grid points in the z direction and 10 grid points in the r direction. There was a slight shift of the optimum ω from 1.5 in the 10x10 case to 1.55 in the 10x25 case. This would support the idea that it is the span of r which is important for determining ω optimum as opposed to the total number of grid points involved. Compare, for example 250 grid points in the 10x25 case with its ω optimum equal to 1.55 with the 225 grid points in the 15x15 case with its optimum over-relaxation parameter equal to 1.65

The data for all experimental runs is given in Table IV, and a graph of the number of iterations required for convergence is graphed in Figure 46. Figure 47 shows the optimum over-relaxation parameter as a function of number of grid points for a square grid.

TABLE I

ADIABATIC THERMALS, INPUT PARAMETERS

CONSERVATION EQUATIONS

Run Number	Initial Volume	Initial Vertical Velocity	Initial Buoyant Acceleration	Stability	$\gamma(=\frac{R}{b})$	$K(=V_r/V_\theta)$	Angular Velocity	Entrainment Coefficient, α
1	300	0	750	.00	1.00	.00	0	.10
2	300	10	750	.00	1.00	.00	0	.10
3	300	20	750	.00	1.00	.00	0	.10
4	300	0	750	.00	1.00	.00	0	.10
5	300	0	750	.00	1.00	.00	0	.22
6	300	0	750	.00	1.00	.00	10	.22
7	300	0	750	.00	.75	.00	10	.22
8	300	0	750	.00	.50	.00	10	.22
9	300	0	750	.00	.25	.00	10	.22
10	300	0	750	.00	.25	.25	10	.22
11	300	0	750	.00	.25	.50	10	.22
12	300	0	750	.00	.25	1.00	10	.22
13	300	0	750	.00	.25	1.00	20	.22
14	300	0	750	.00	.25	1.00	30	.22
15	300	0	750	.00	1.00	.00	20	.22
16	300	0	750	.00	1.00	.00	30	.22
17	150	0	375	.00	1.00	.00	20	.22
18	300	0	750	-.10	1.00	.00	10	.22
19	300	0	750	-.10	1.00	.00	0	.22
20	300	0	750	.10	1.00	.00	0	.22
21	300	0	750	.10	1.00	.00	10	.22
22	300	0	750	.10	1.00	.00	20	.22
23	300	0	750	.10	1.00	.00	30	.22
24	300	0	750	.00	.50	.00	20	.22
25	300	0	750	.00	.50	.00	30	.22
26	150	0	375	.00	.50	.00	20	.22
27	300	0	750	-.10	.50	.00	10	.22
28	300	0	750	-.10	.50	.00	0	.22
29	300	0	750	.10	.50	.00	0	.22
30	300	0	750	.10	.50	.00	10	.22
31	300	0	750	.10	.50	.00	20	.22
32	300	0	750	.10	.50	.00	30	.22

TABLE II

NON-ADIABATIC THERMALS, INPUT PARAMETERS

CONSERVATION EQUATIONS

Run Number	Initial Volume	Initial Vertical Velocity	Initial Buoyancy	Stability	$\gamma(=\frac{R}{b})$	$K(=V_r/V_\theta)$	Angular Velocity	Entrainment Coefficient, α	Diffusion Velocity
1	100	10	0	0	1.00	0	0	.22	5.5
2	100	10	0	0	1.00	0	10	.22	5.5
3	100	10	0	0	1.00	0	20	.22	5.5
4	100	10	0	0	1.00	0	30	.22	5.5
5	100	10	0	0	.50	0	0	.22	5.5
6	100	10	0	0	.50	0	10	.22	5.5
7	100	10	0	0	.50	0	20	.22	5.5
8	100	10	0	0	.50	0	30	.22	5.5
9	100	10	0	0	.25	0	0	.22	5.5
10	100	10	0	0	.25	0	10	.22	5.5
11	100	10	0	0	.25	0	20	.22	5.5
12	100	10	0	0	.25	0	30	.22	5.5
13	100	10	0	0	1.00	0	0	.22	10.0
14	100	10	0	0	1.00	0	10	.22	10.0
15	100	10	0	0	1.00	0	20	.22	10.0
16	100	10	0	0	1.00	0	30	.22	10.0

TABLE III

NUMERICAL EXPERIMENTS FOR SOLUTIONS OF THE HYDRODYNAMIC MODEL

Run #	Angular Velocity	Buoyancy Production Rate	Computed Entrainment Coefficient
1	0.00	0	.25
2	.001	0	.25
3	.0025	0	.20
4	.005	0	0.00
5	.01	0	0.00
6	.02	0	0.00
7	0.00	5%	.28
8	.0025	5%	.25
9	.005	5%	.20
10	.01	5%	0.00
11	0.00	10%	.33
12	.005	10%	.25
13	.01	10%	.20

All experiments were performed with a 20 x 40 grid, a 200 meter grid spacing and a 3 second time increment. The initial thermal was described in Appendix A, with a value of $T_o = 3^oK$.

TABLE IV

VORTICITY EQUATION CONVERGENCE DATA

NUMBER OF ITERATIONS

Over-relaxation Parameter	Grid Size (R x H) 5x5	10x10	15x15	20x20	25x25	10x25
1.00	4	35	*	*	*	*
1.05	5	32	*	*	*	48
1.10	5	30	*	*	*	44
1.15	5	27	*	*	*	41
1.20	6	25	*	*	*	38
1.25	6	23	*	*	*	34
1.30	7	20	47	*	*	31
1.35	7	18	42	*	*	29
1.40	7	16	38	*	*	26
1.45	8	14	34	*	*	23
1.50	9	16	30	*	*	21
1.55	11					19
1.60	12	18	21	42	*	20
1.65	14					22
1.70	17	20	28	30	48	26
1.75	21					36
1.80	27	35	33	40	47	42
1.85	36					47
1.90	*	*	*	*	*	*
1.95	*					*
2.00						

* Did not converge with 50 iterations.

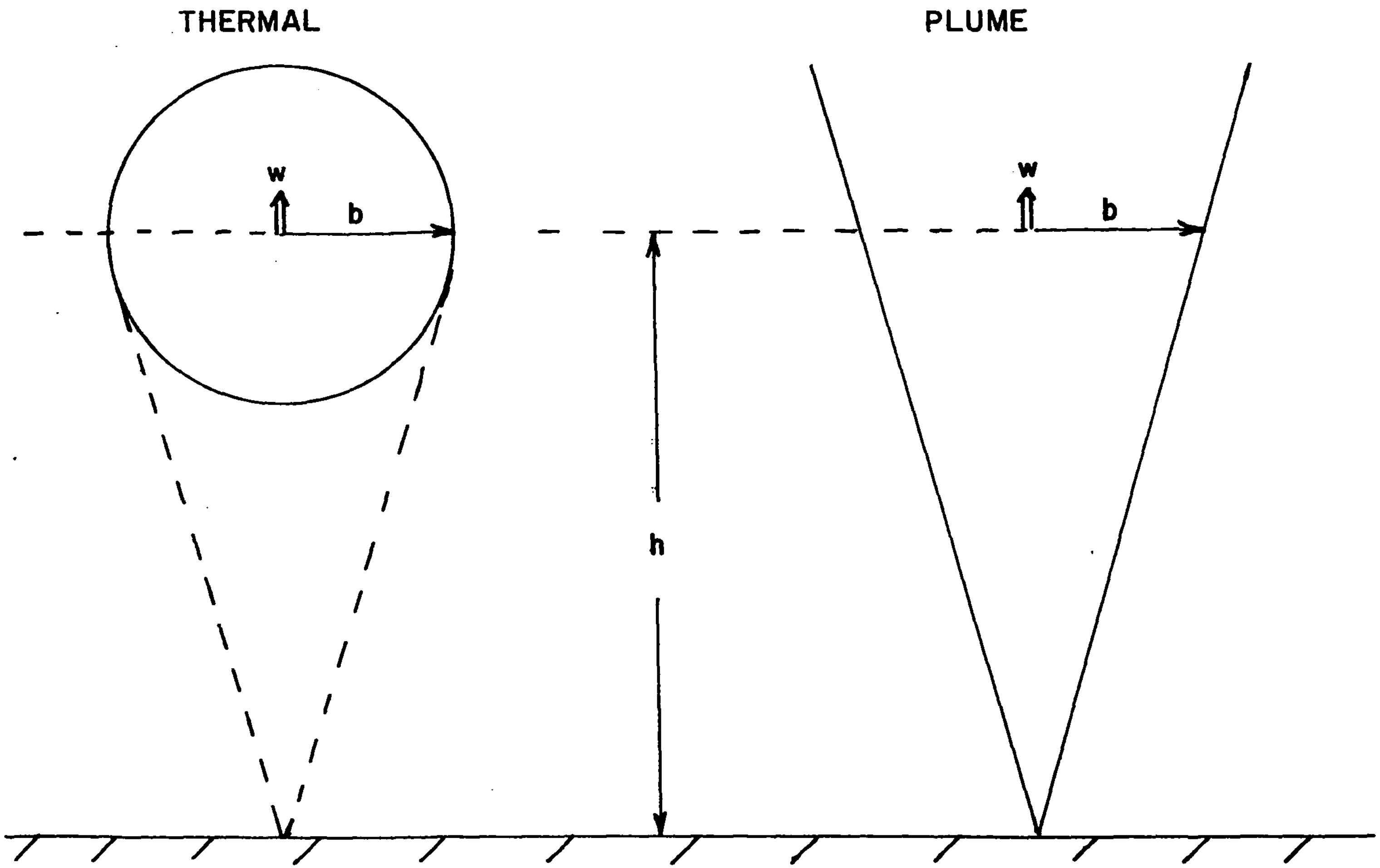

Figure 1. Schematic representation of the thermal and plume forms of convective elements.

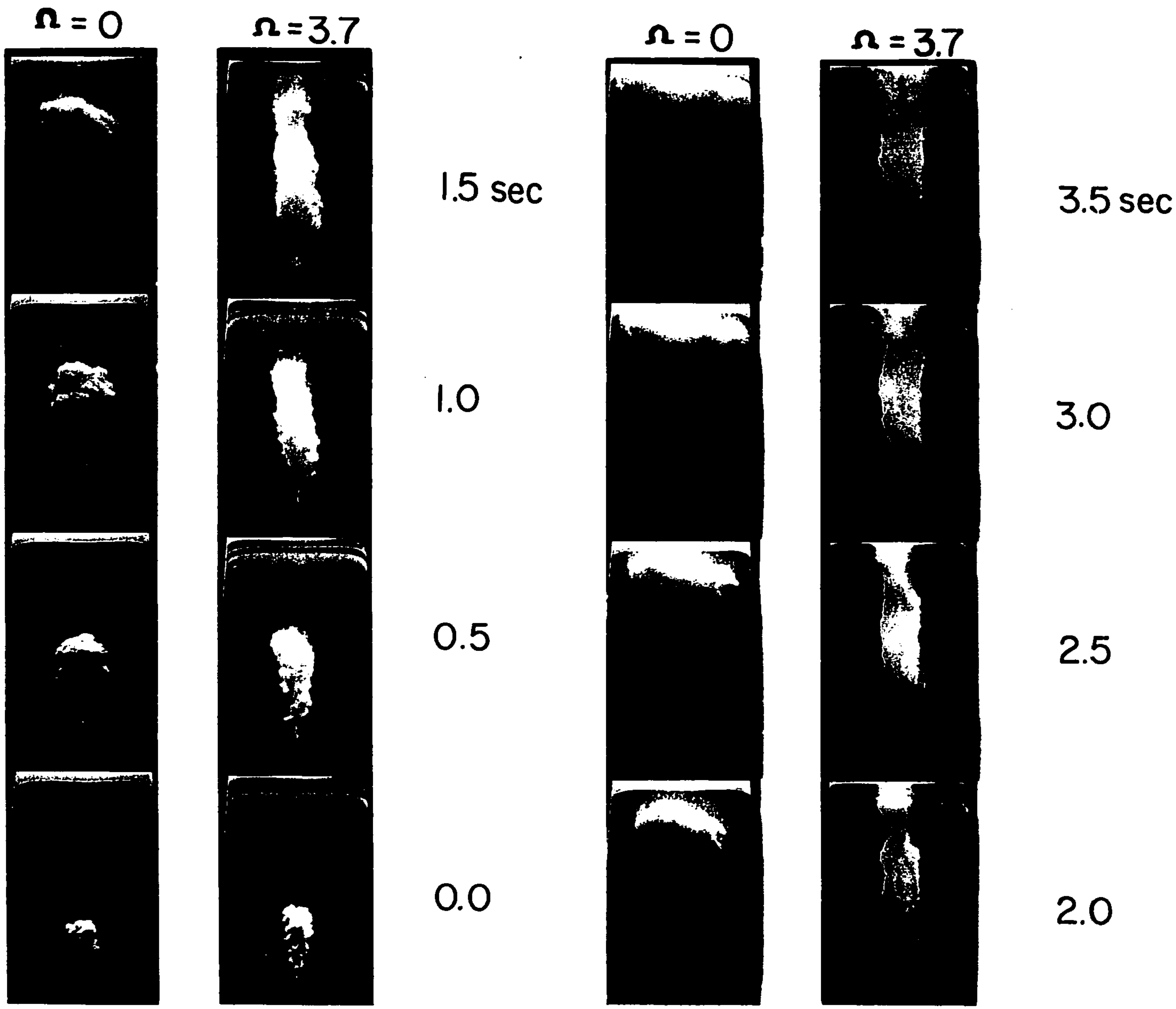

Figure 2. Sequential photographs of rotating and nonrotating thermal elements.

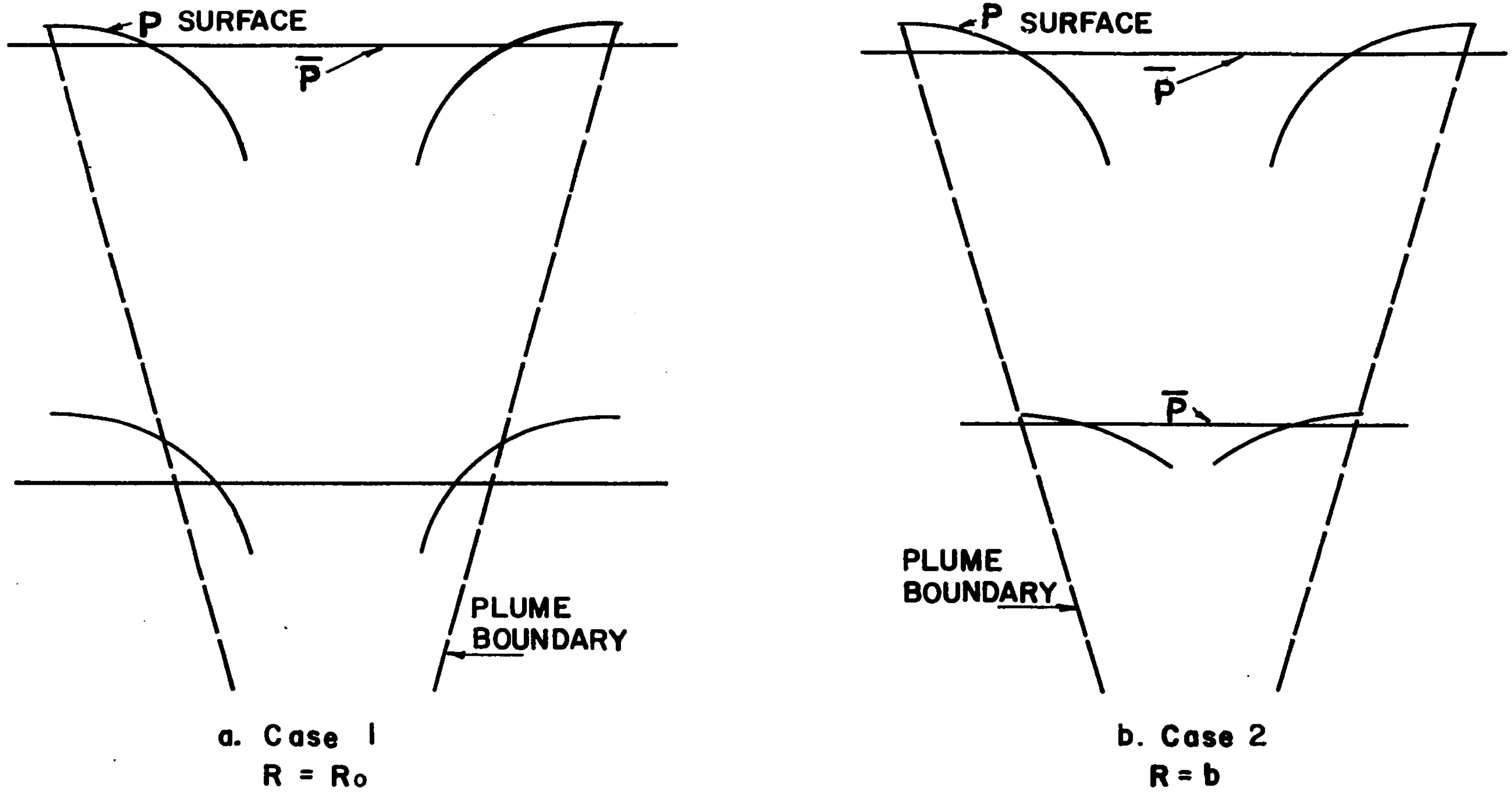

Figure 3. Average pressure surfaces within a rotating plume.

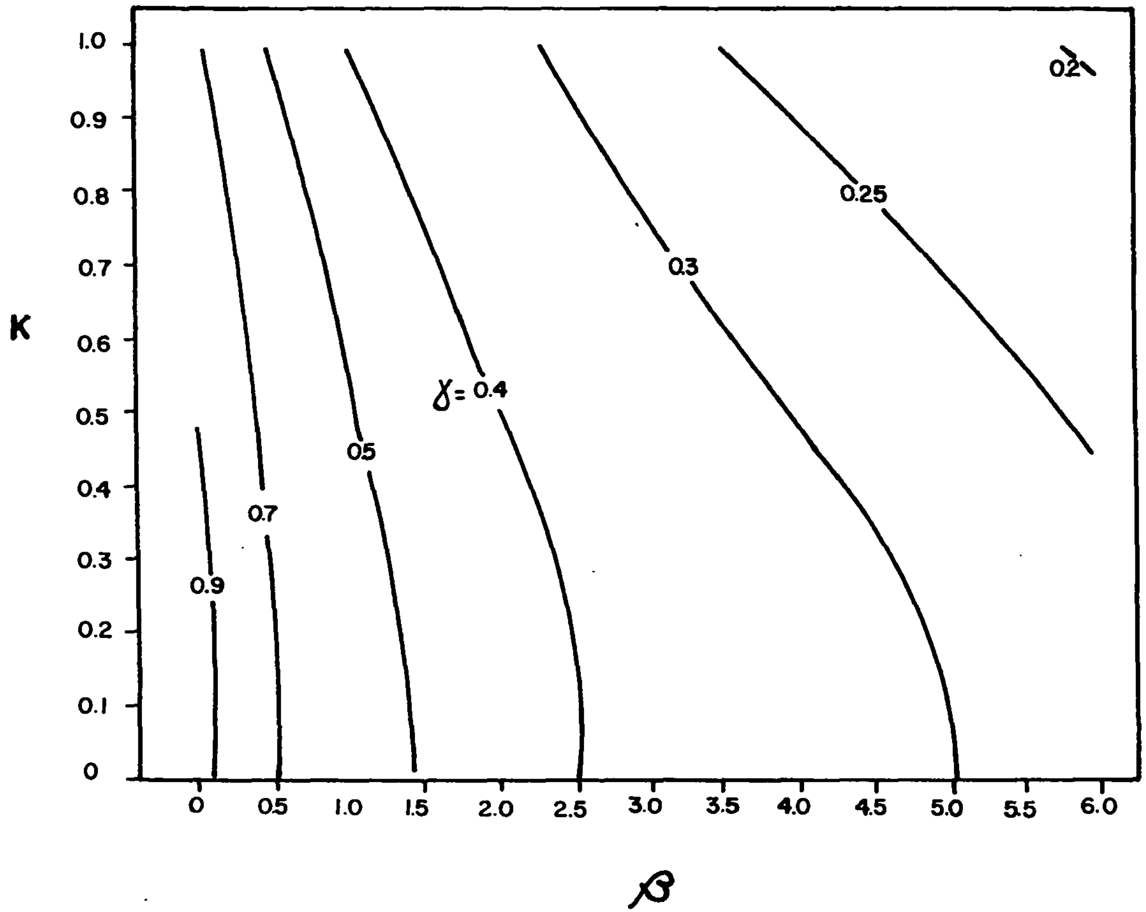

Figure 4. Parameter space for rotational modification of buoyancy force.

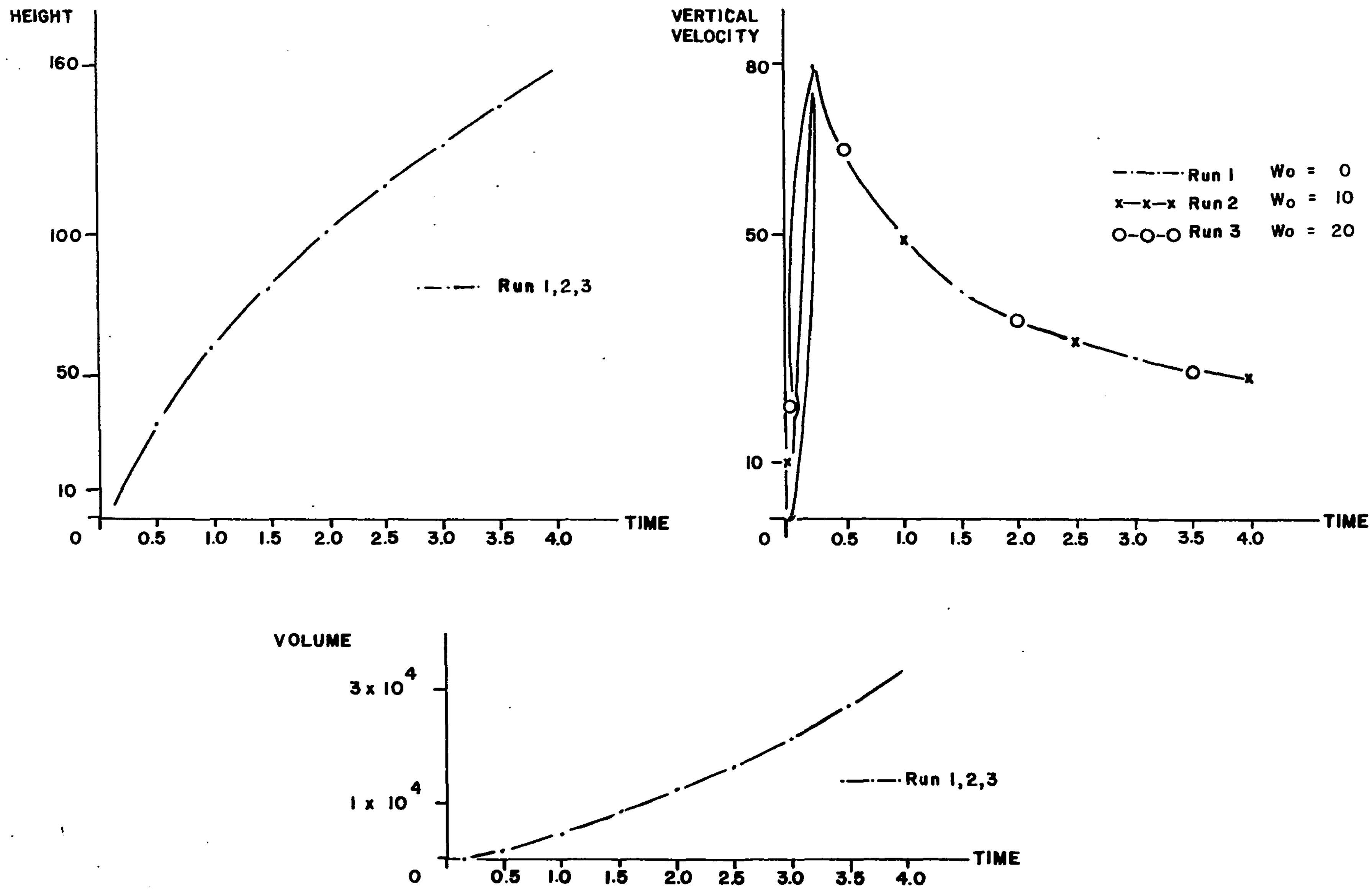

Figure 5. Adiabatic conservation equation model. Run 1, 2, and 3.

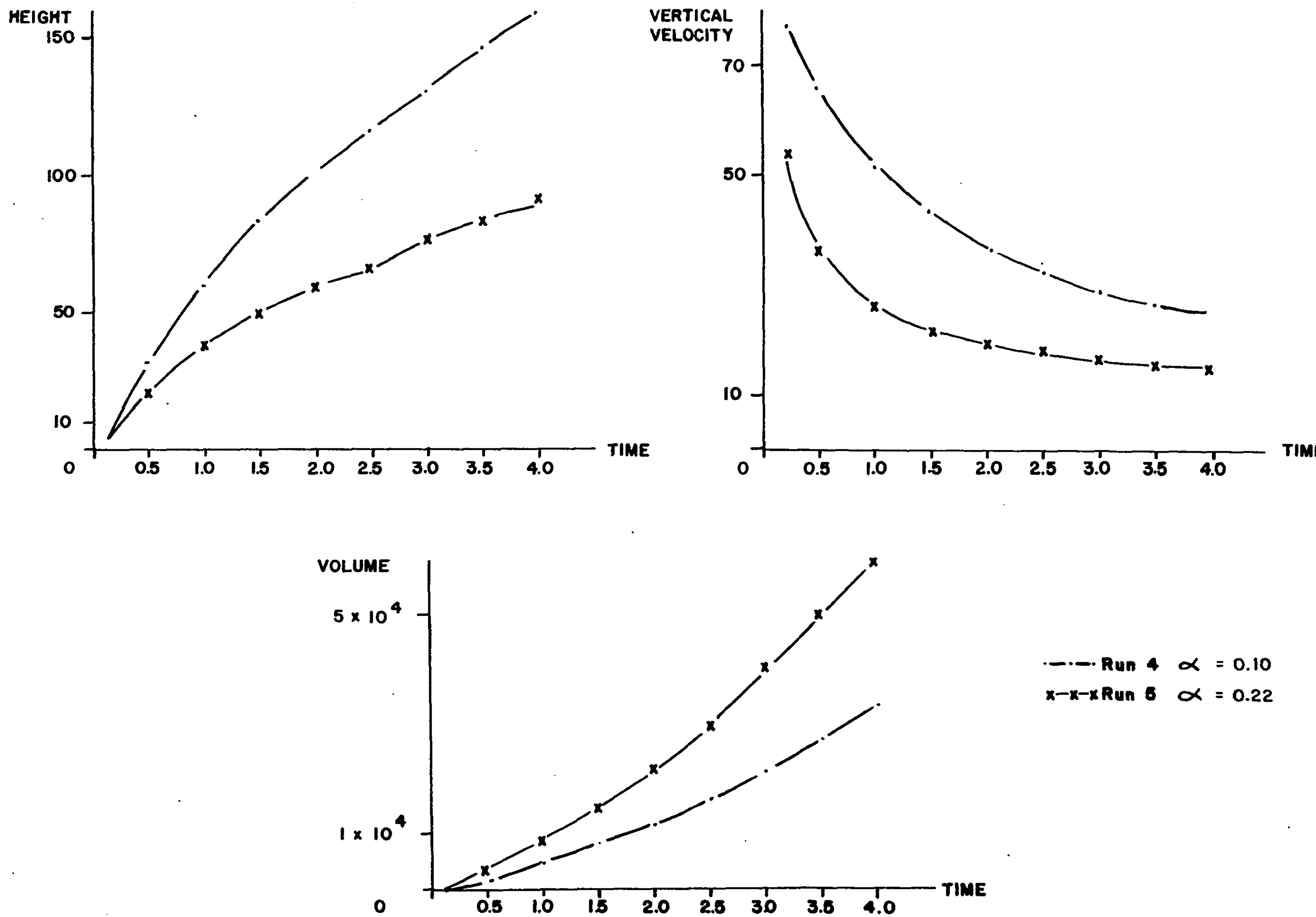

Figure 6. Adiabatic conservation equation model. Runs 4-5.

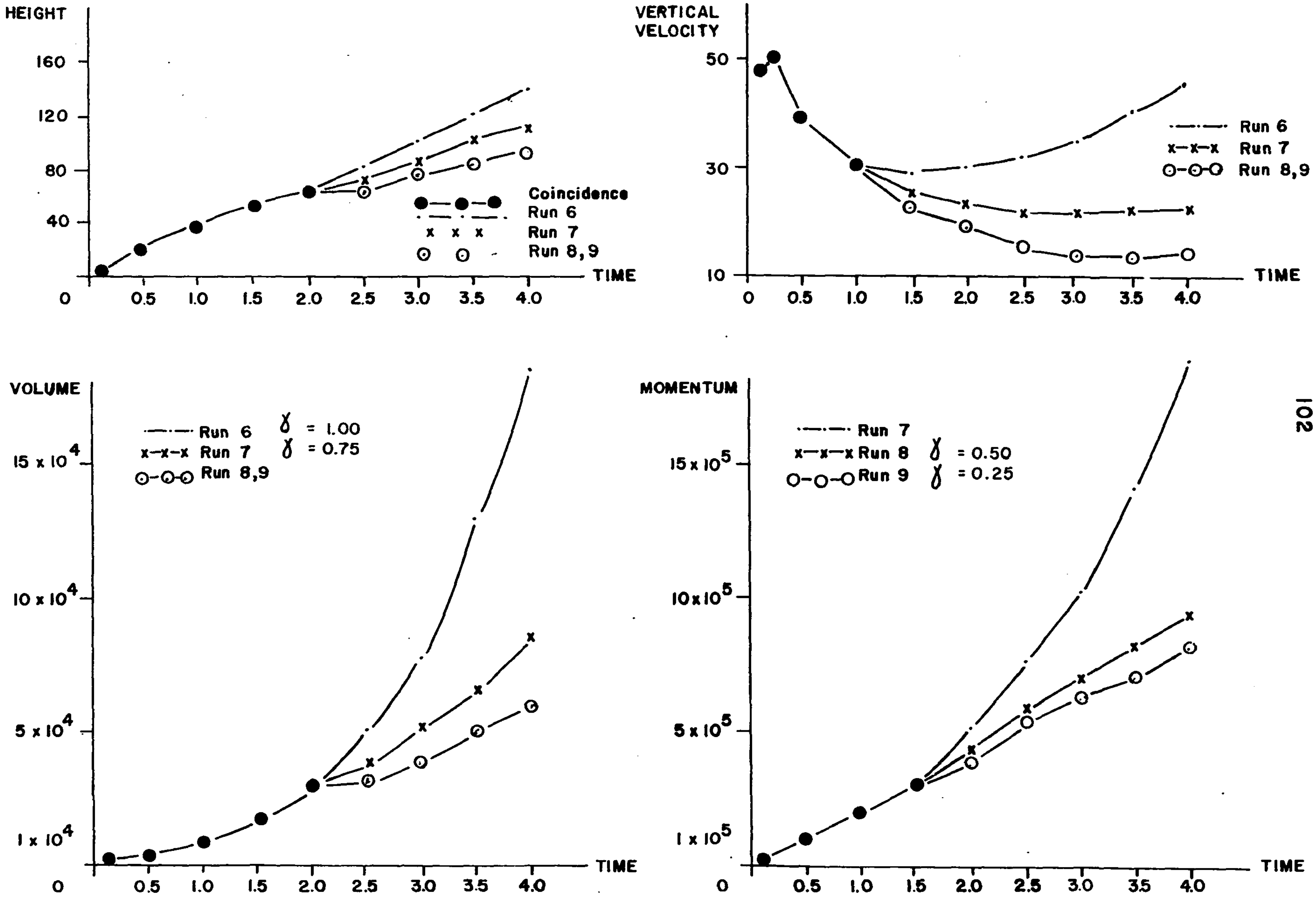

Figure 7. Adiabatic conservation equation model. Runs 6, 7, 8, and 9.

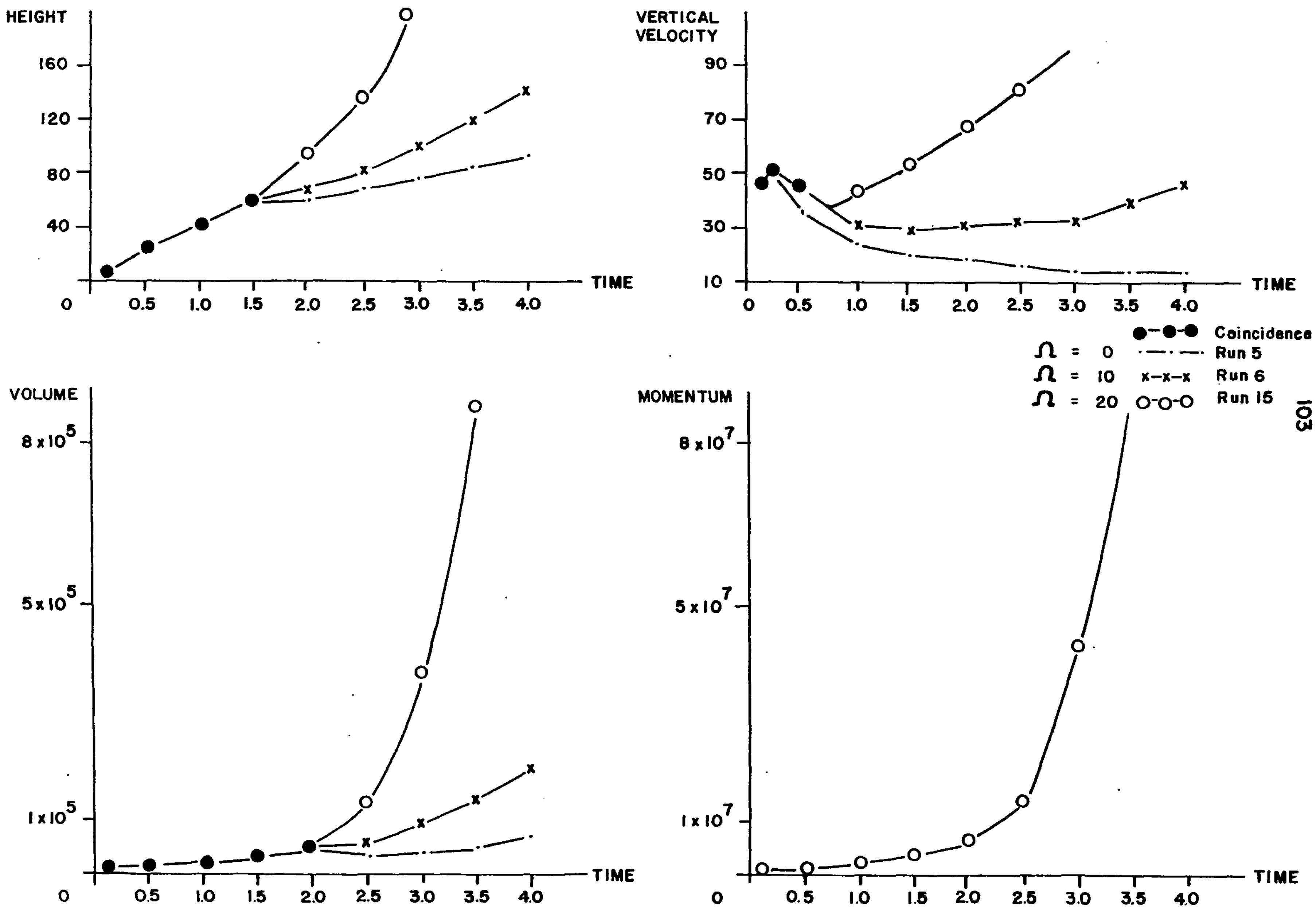

Figure 8. Adiabatic conservation equation model. Runs 5, 6, 15.

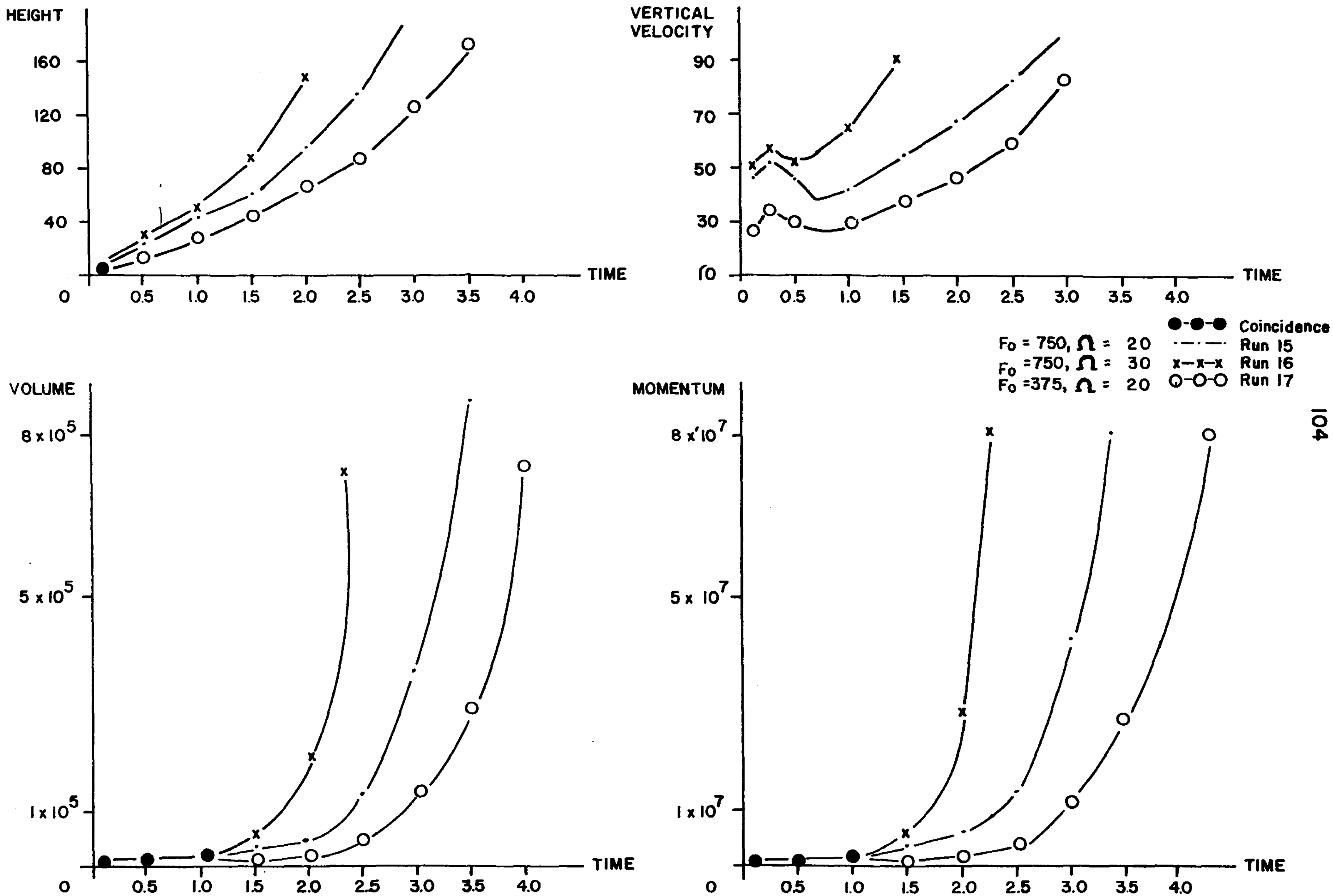

Figure 9. Adiabatic conservation equation model. Runs 15-17.

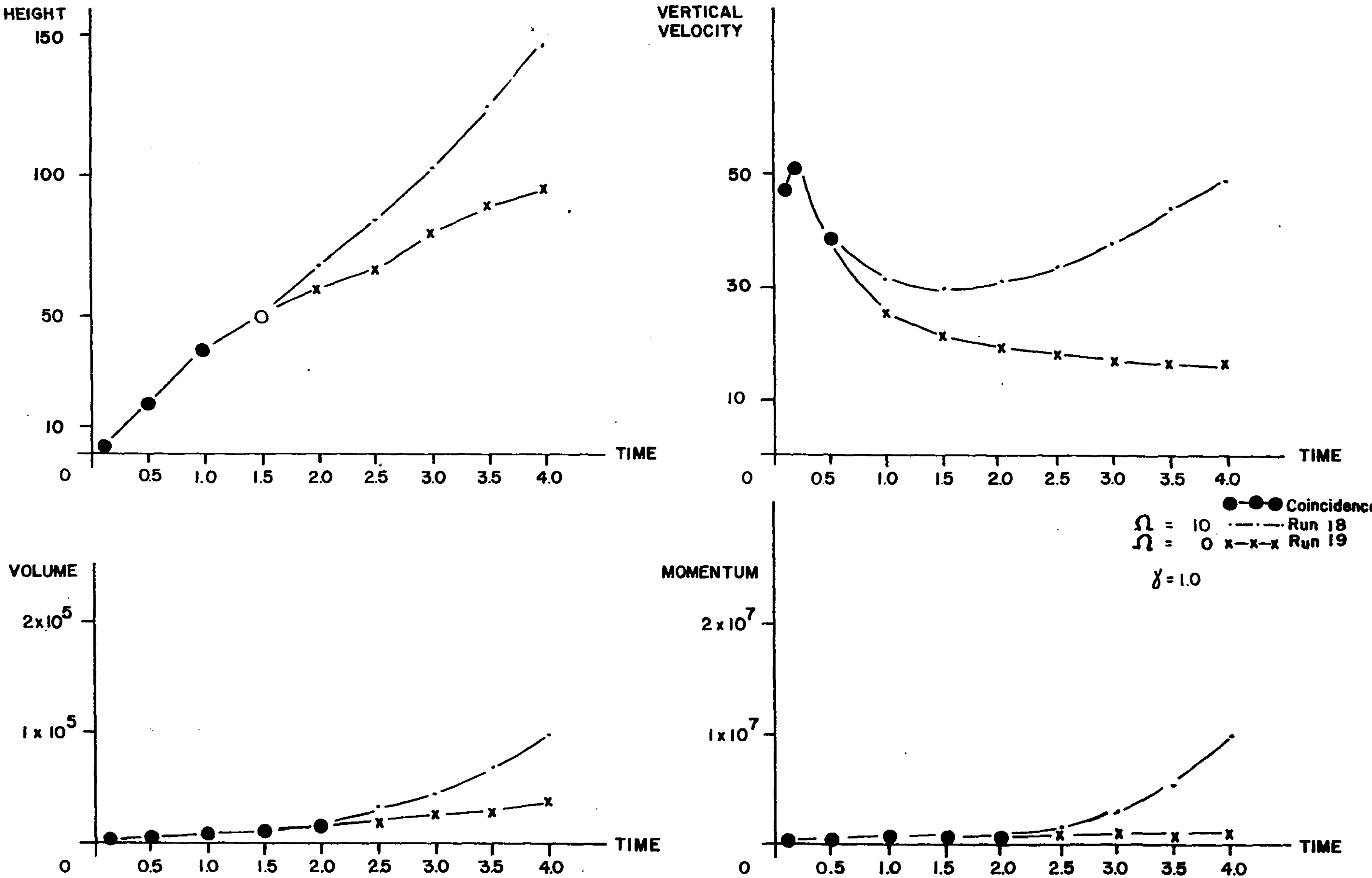

Figure 10. Adiabatic conservation equation model. Runs 18-19. Unstable stratification.

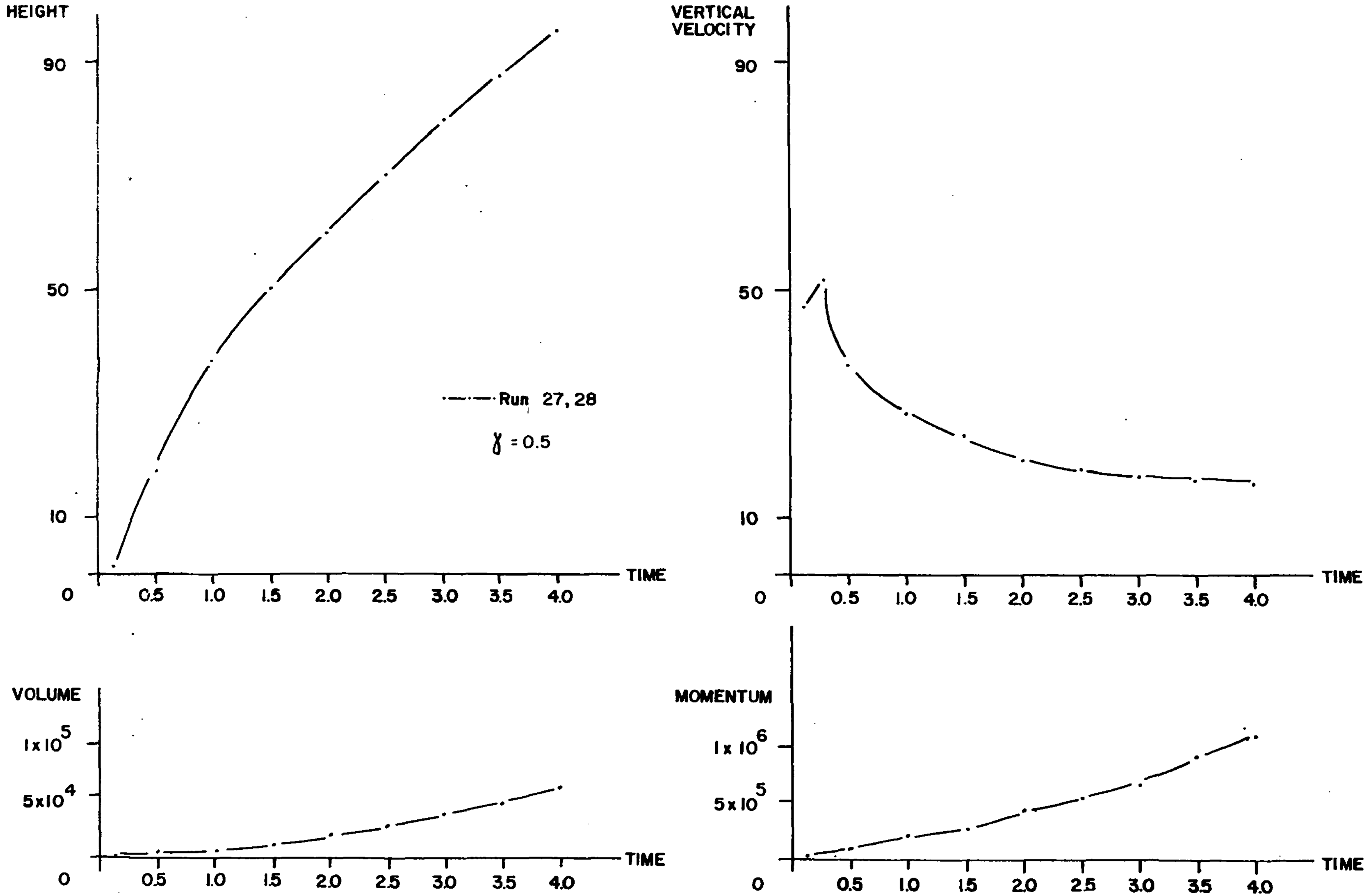

Figure 11. Adiabatic conservation equation model. Runs 27-28. Unstable stratification.

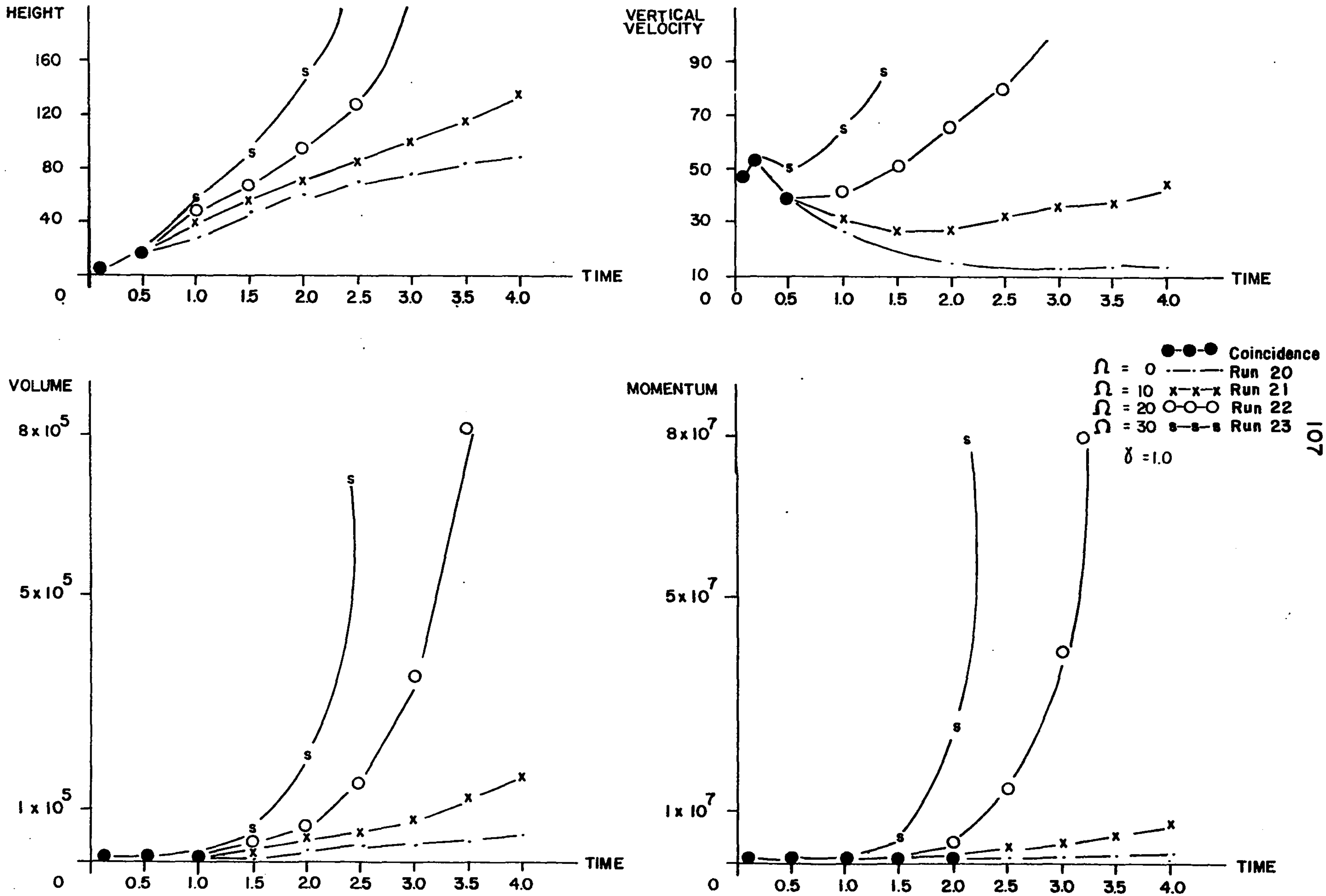

Figure 12. Adiabatic conservation equation model. Runs 20-24. Stable stratification.

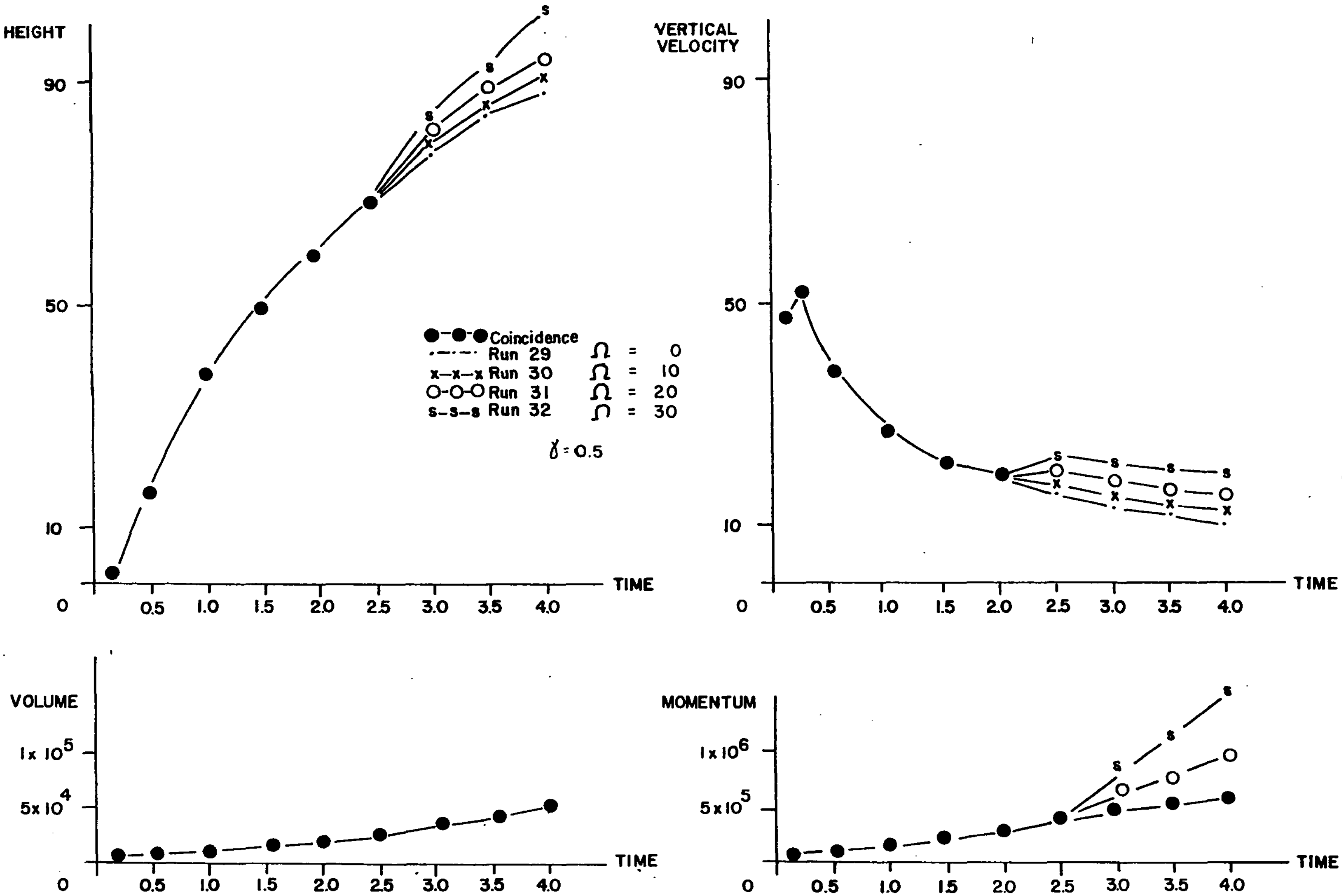

Figure 13. Adiabatic conservation equation model. Runs 29-32. Stable stratification.

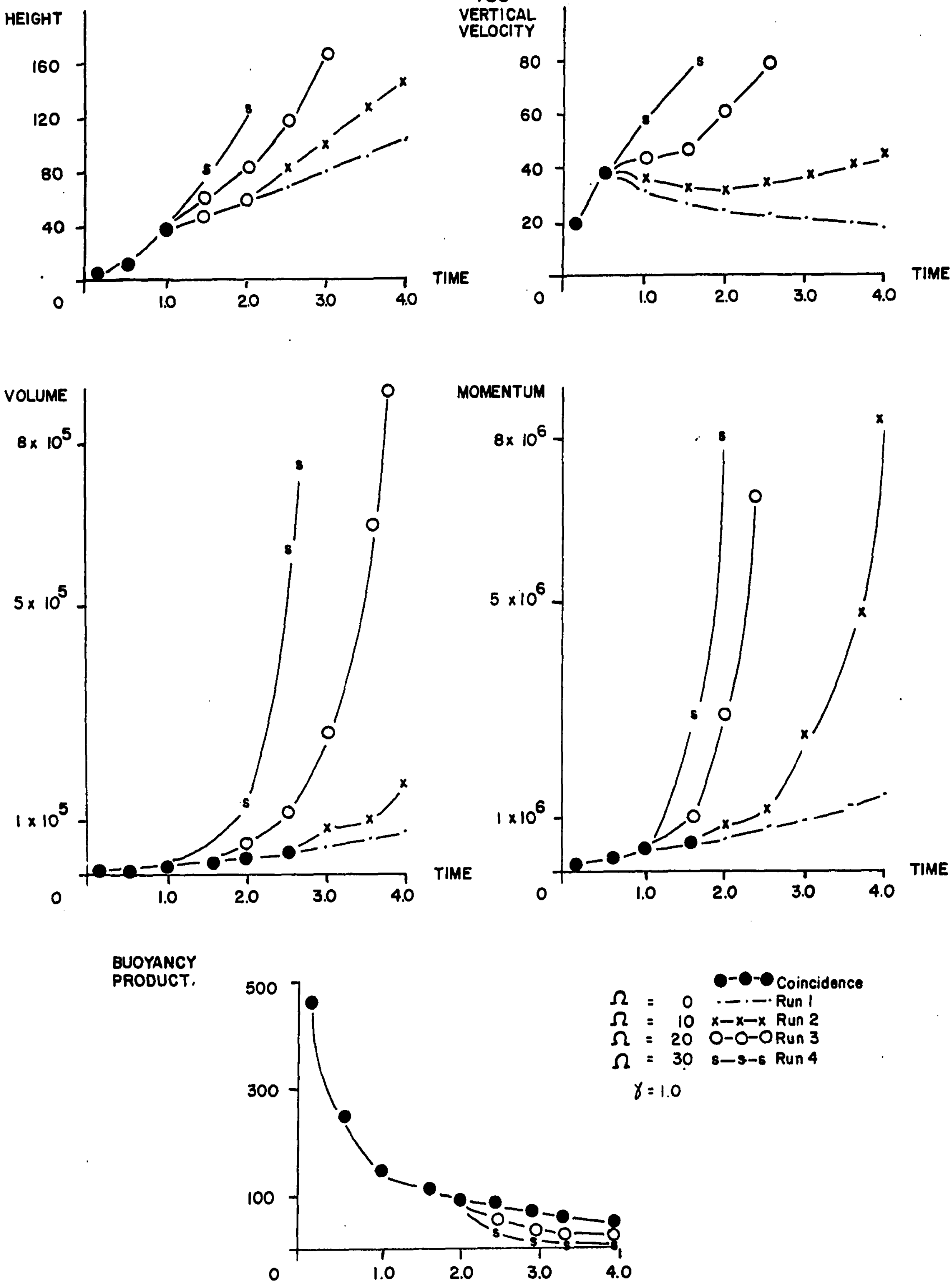

Figure 14. Non-adiabatic conservation equation model. Runs 1-4.

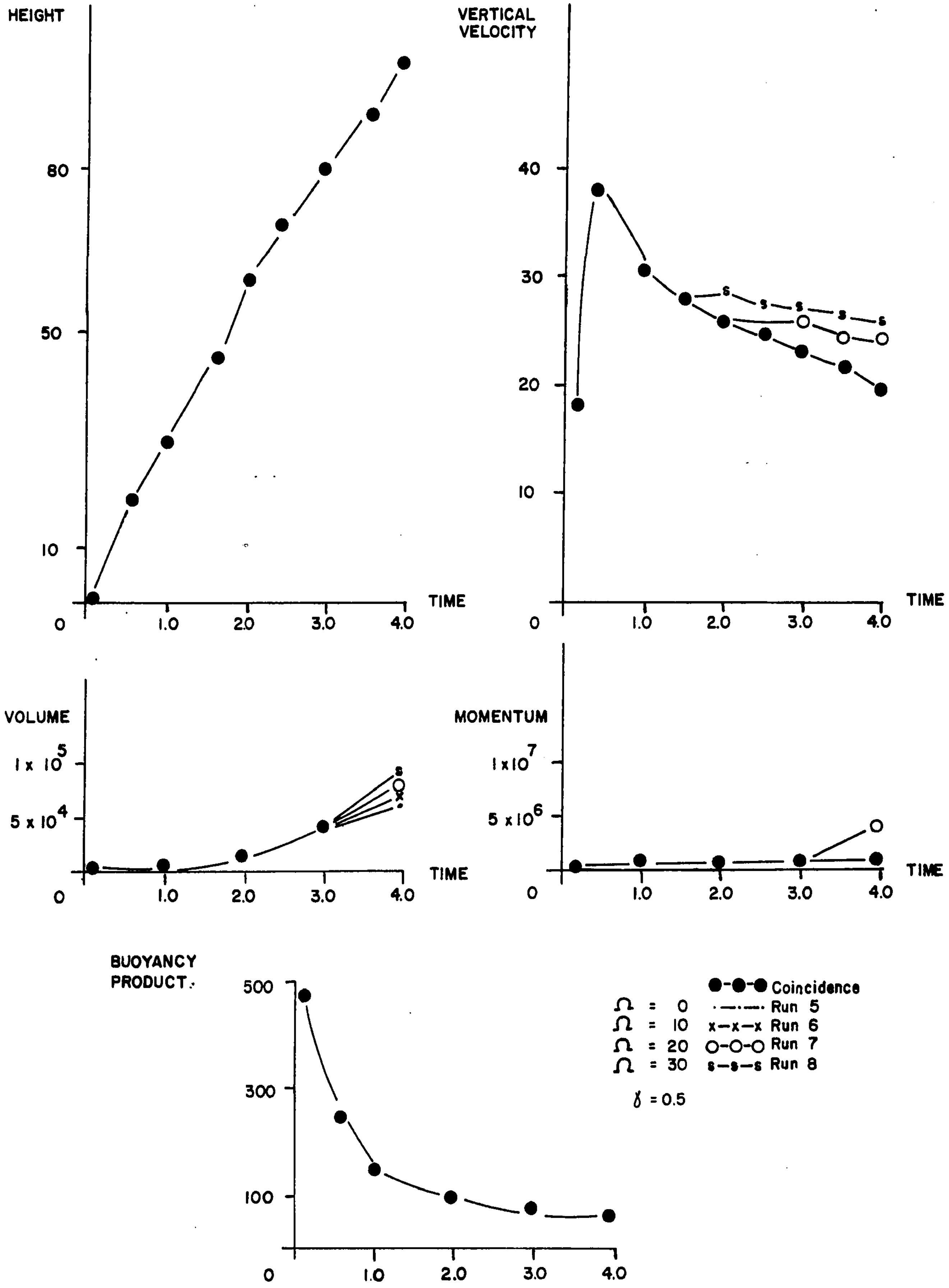

Figure 15. Non-adiabatic conservation equation model. Runs 5-8.

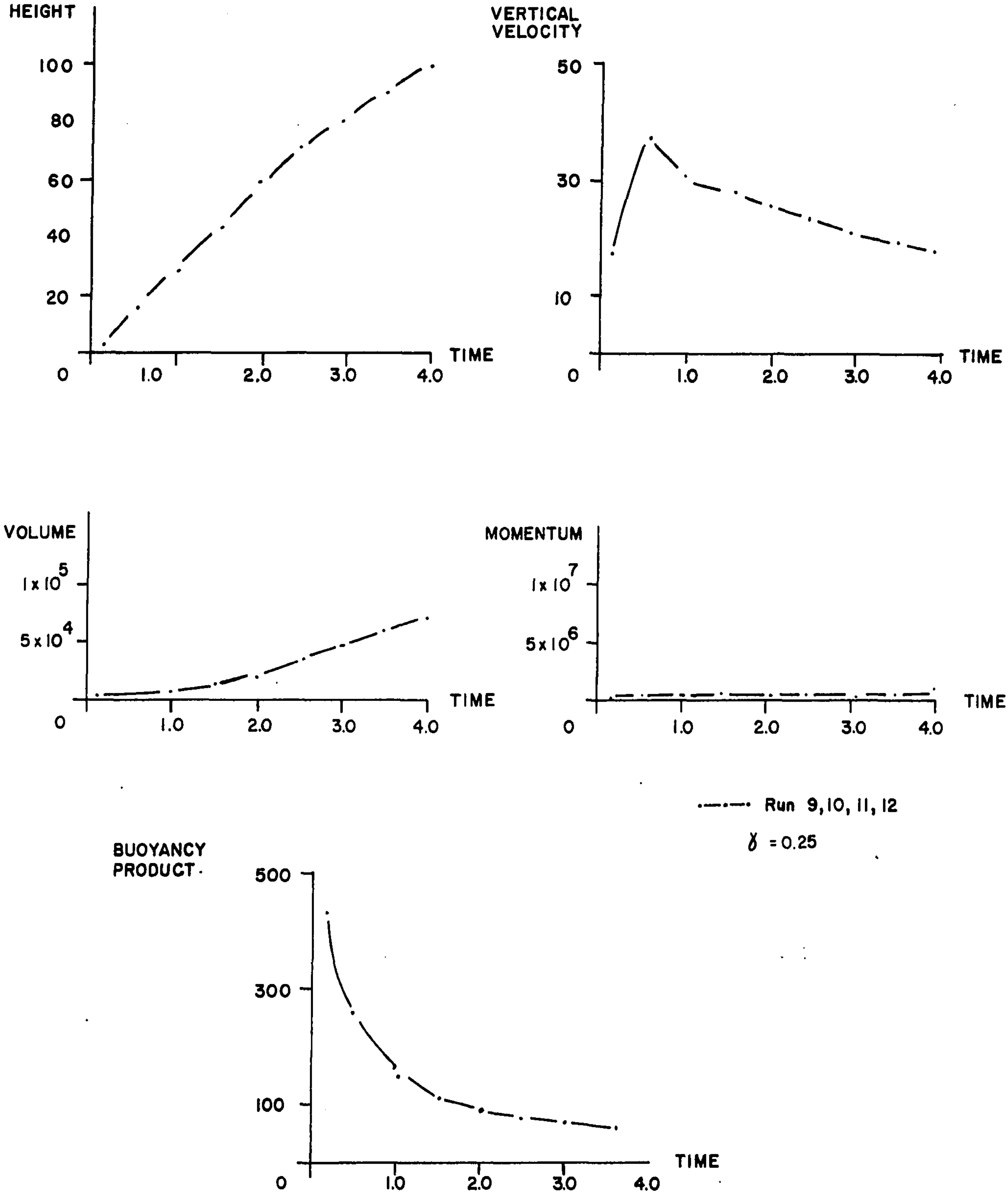

Figure 16. Non-adiabatic conservation equation model. Runs 9-12.

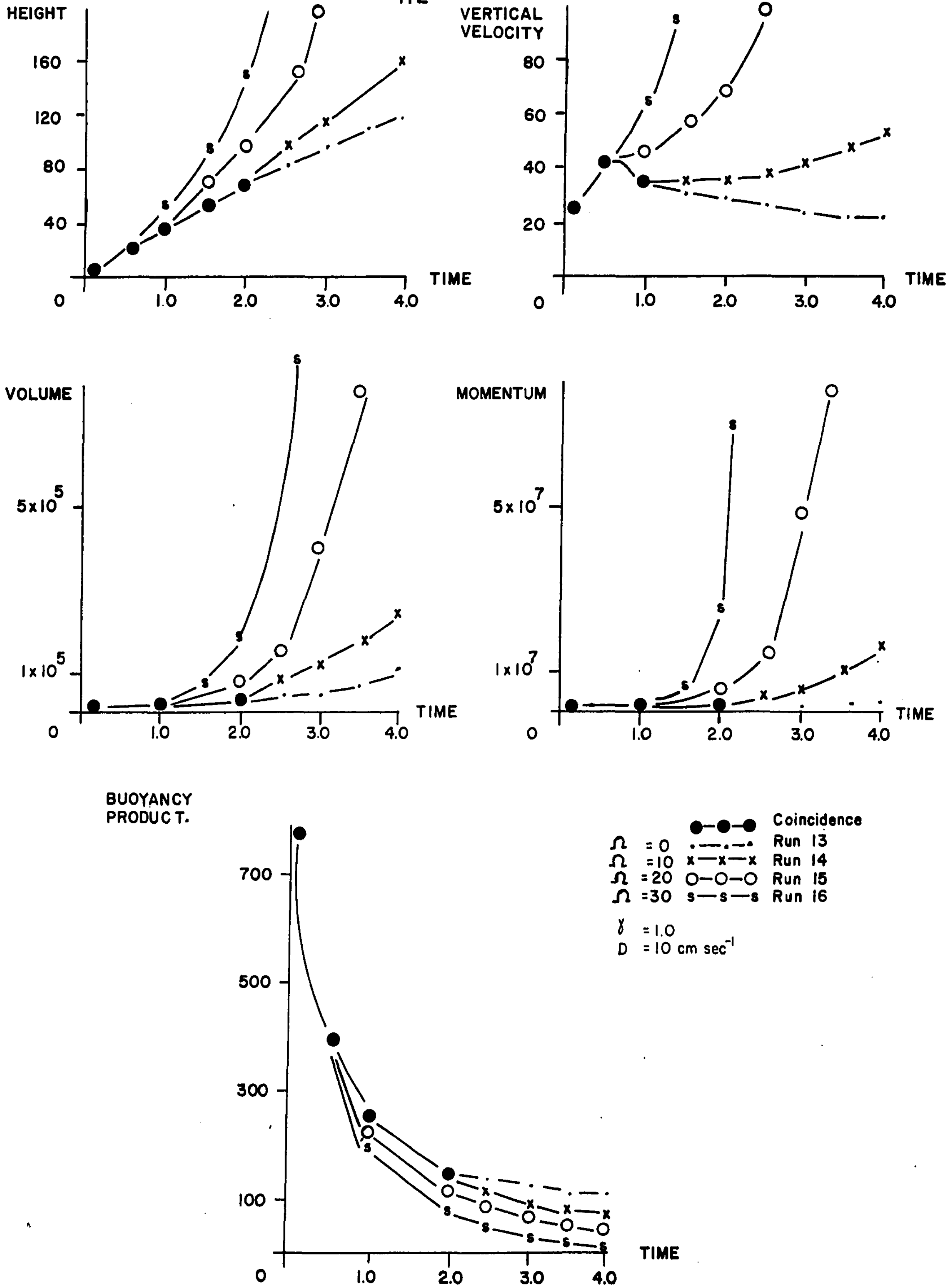

Figure 17. Non-adiabatic conservation equation model. Runs 13-16.

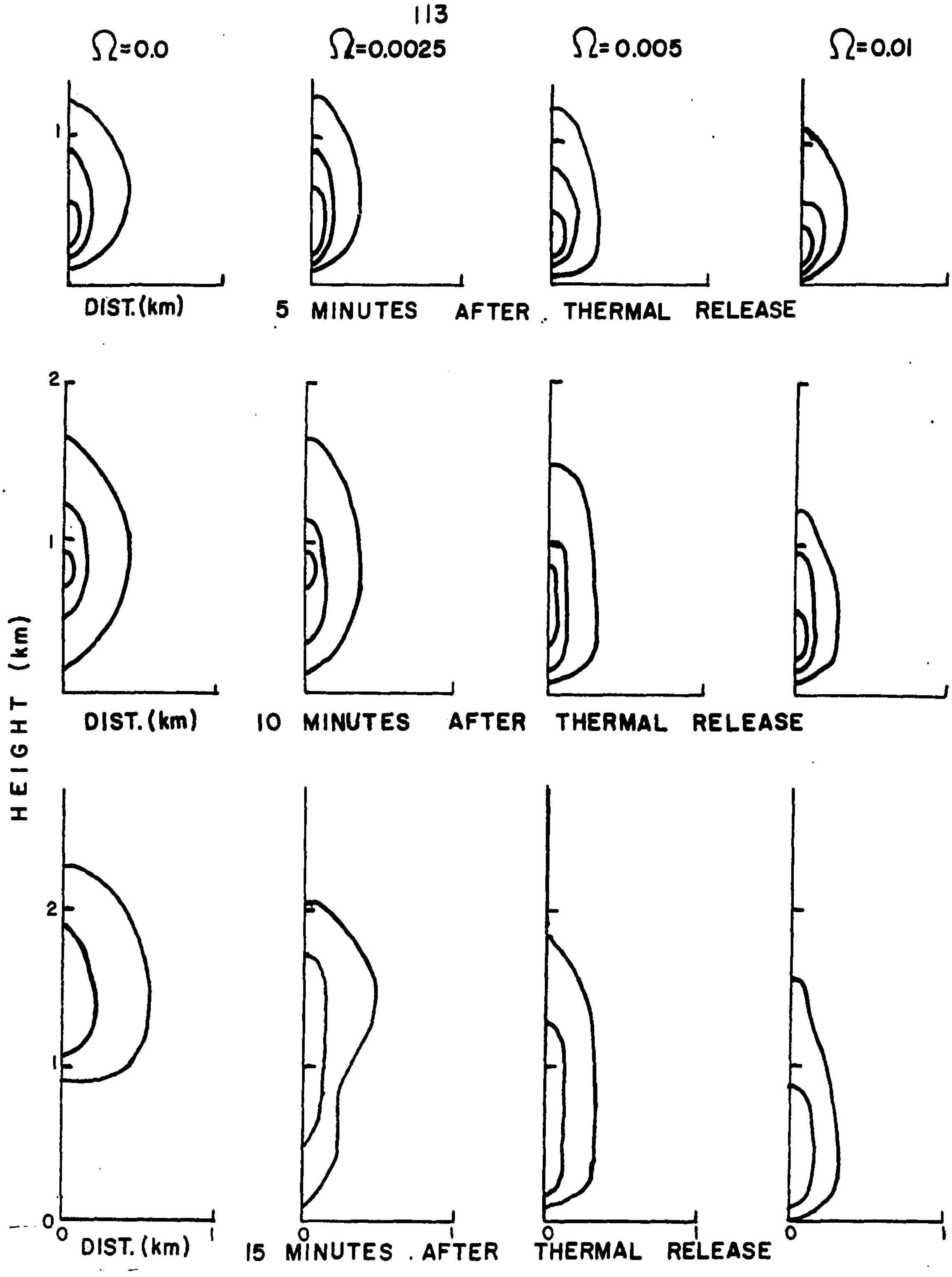

Figure 18. Temperature structure in the adiabatic thermal elements at 5, 10, and 15 minutes after thermal release, for 4 different rotation rates. Contours drawn for 0°, 1°, and 3° temperature excess.

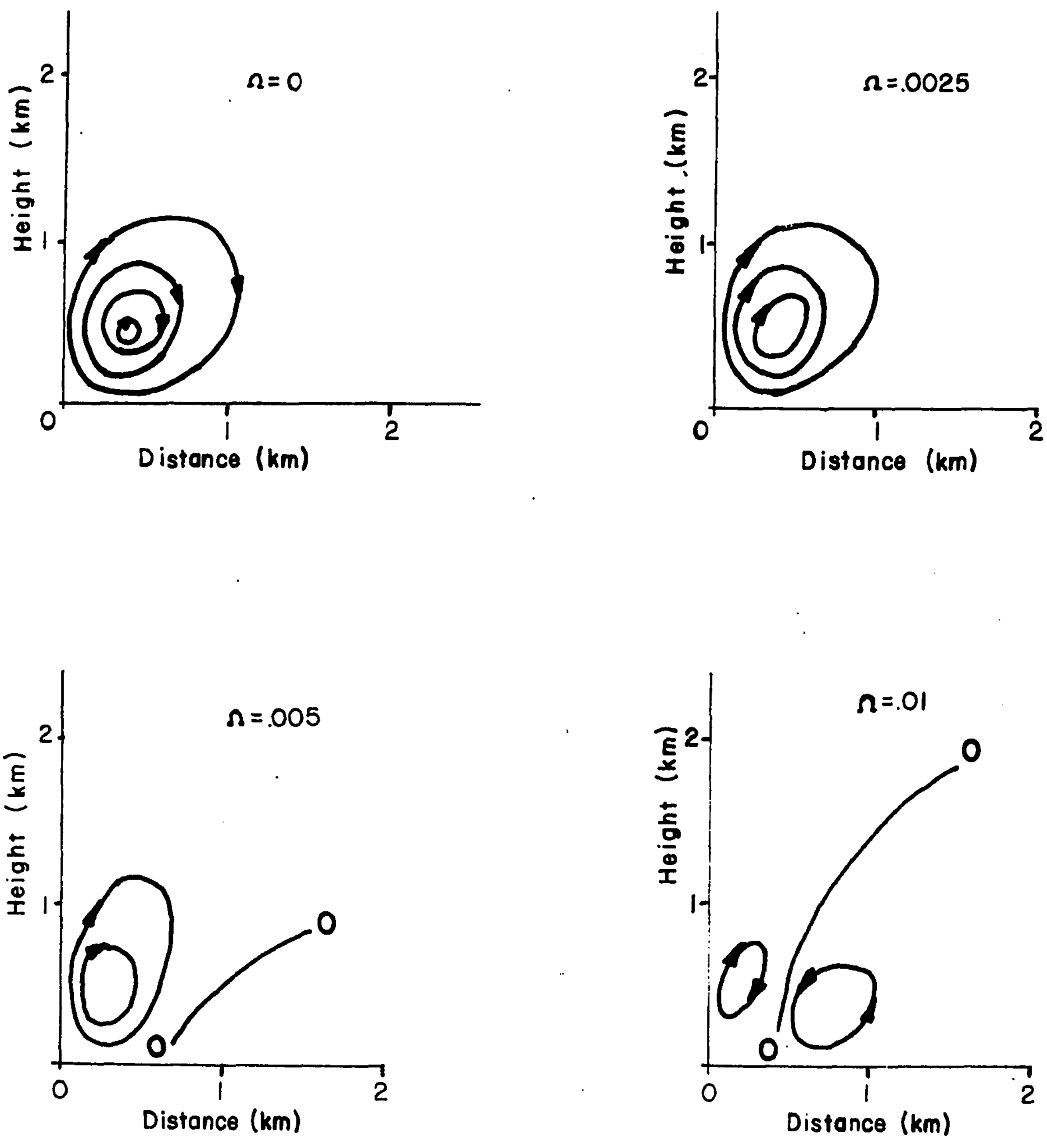

Figure 19a. Streampattern in the adiabatic thermals 5 minutes after thermal release for 4 different rotation rates. Contours drawn for 25 x 10^3 m^3 sec^{-1} intervals.

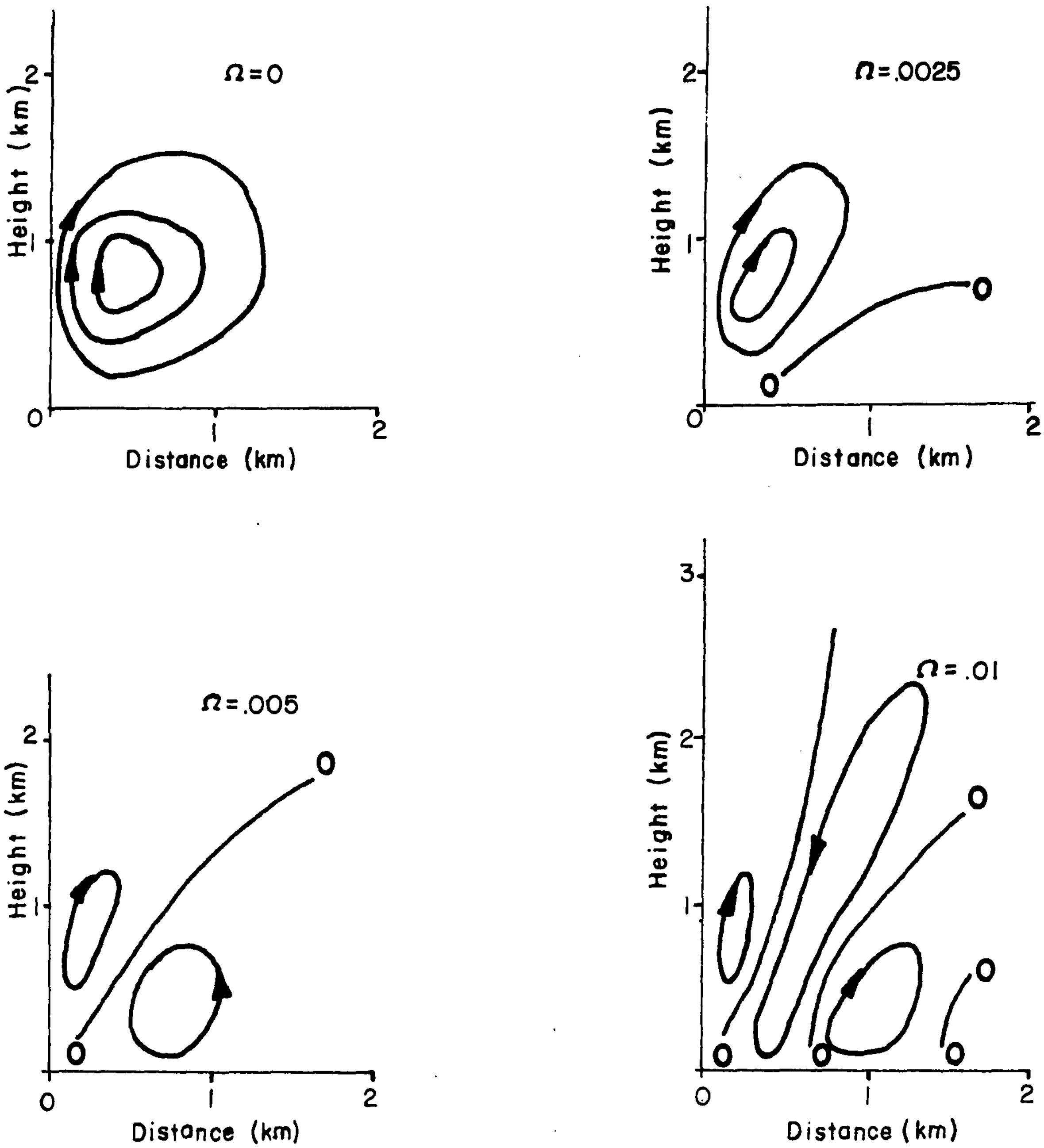

Figure 19b. Same as 19a, 10 minutes after thermal release. Contours drawn for $50 \times 10^3\ m^3\ sec^{-1}$ intervals.

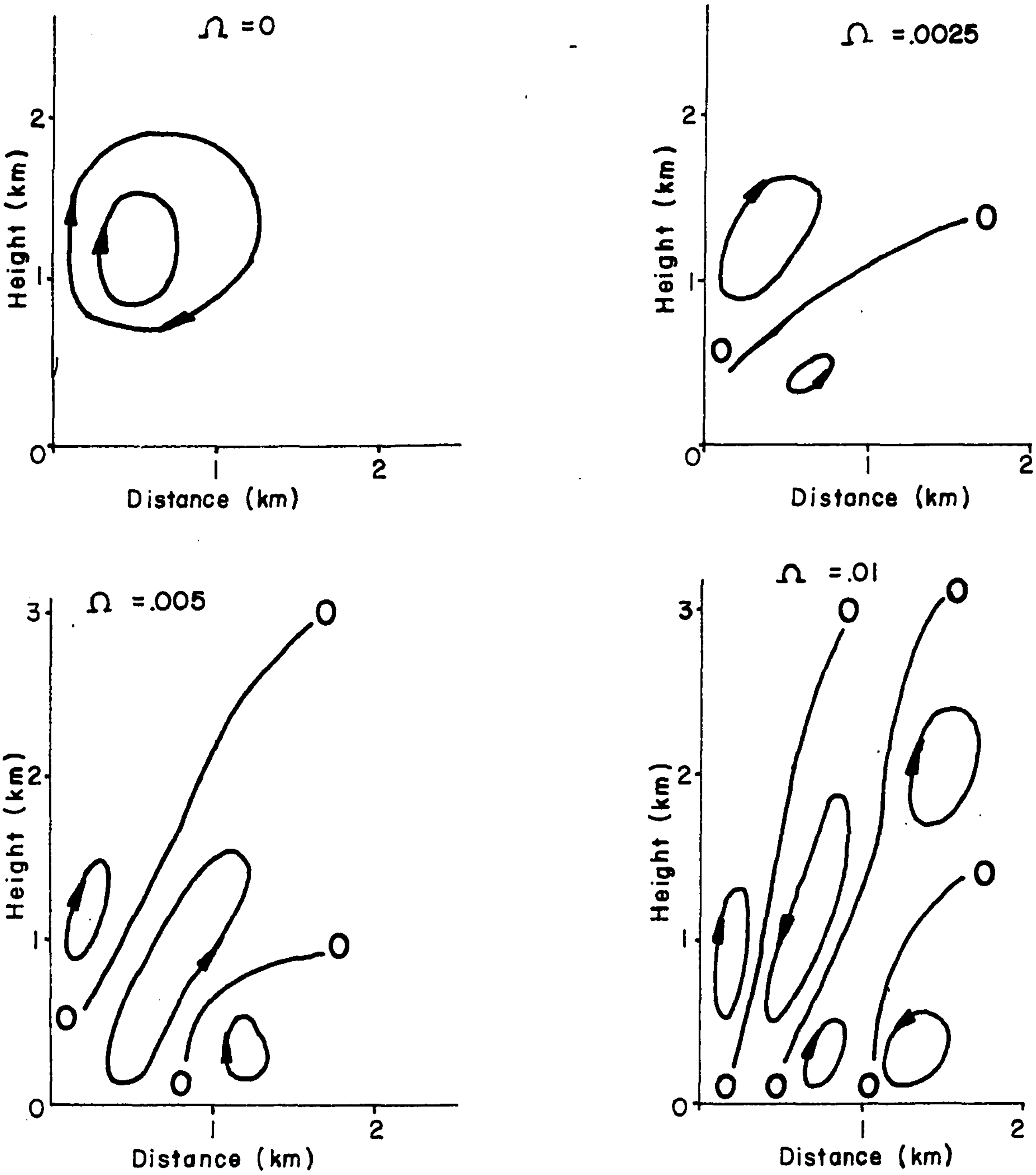

Figure 19c. Same as 19a, 15 minutes, 100 x 10^3 m^3 sec^{-1} intervals for top two patterns. 50 x 10^3 m^3 sec^{-1} for Ω = .005, 25 x 10^{-3} intervals for Ω = .01.

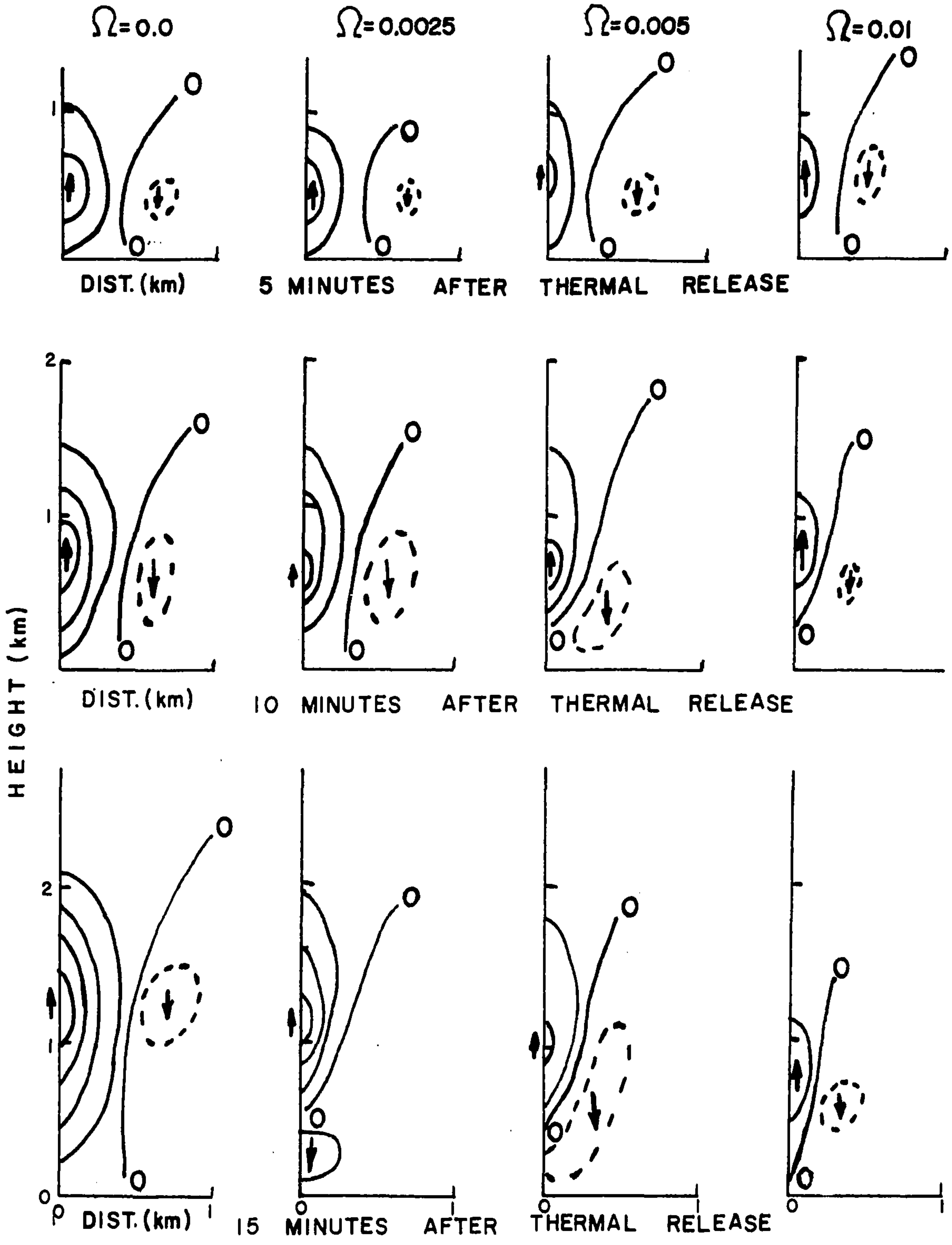

Figure 20. Vertical velocity patterns for adiabatic thermals. Solid contours drawn for 0, 1, 3, 5, 7 m sec^{-1}. Dashed contours drawn for 0.5 m sec^{-1}.

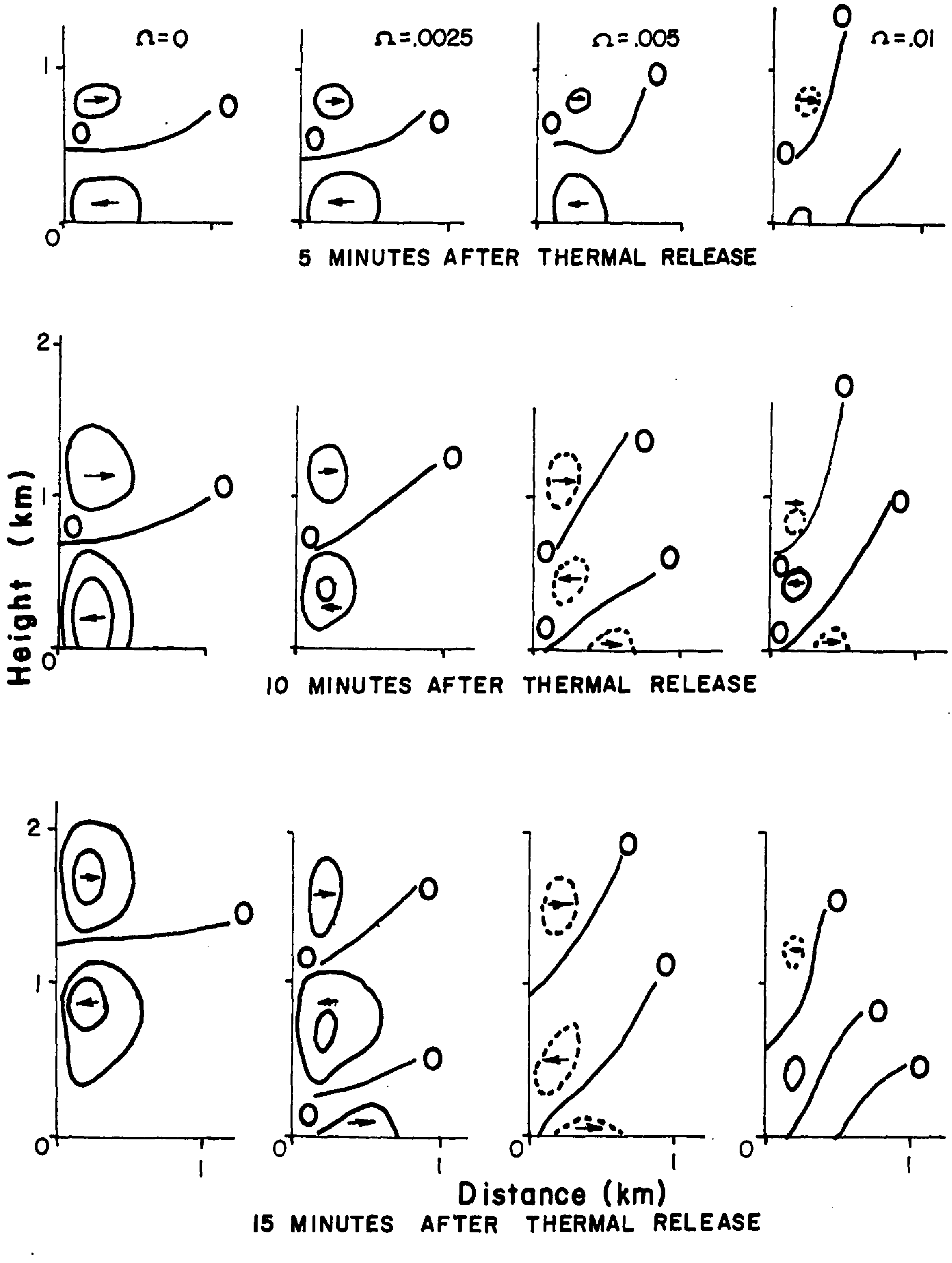

Figure 21. Radial velocity structure for adiabatic thermals. Solid contours drawn for 0, .5, 1.0 m sec^{-1}. Dashed contours drawn for 0.25 m sec^{-1}.

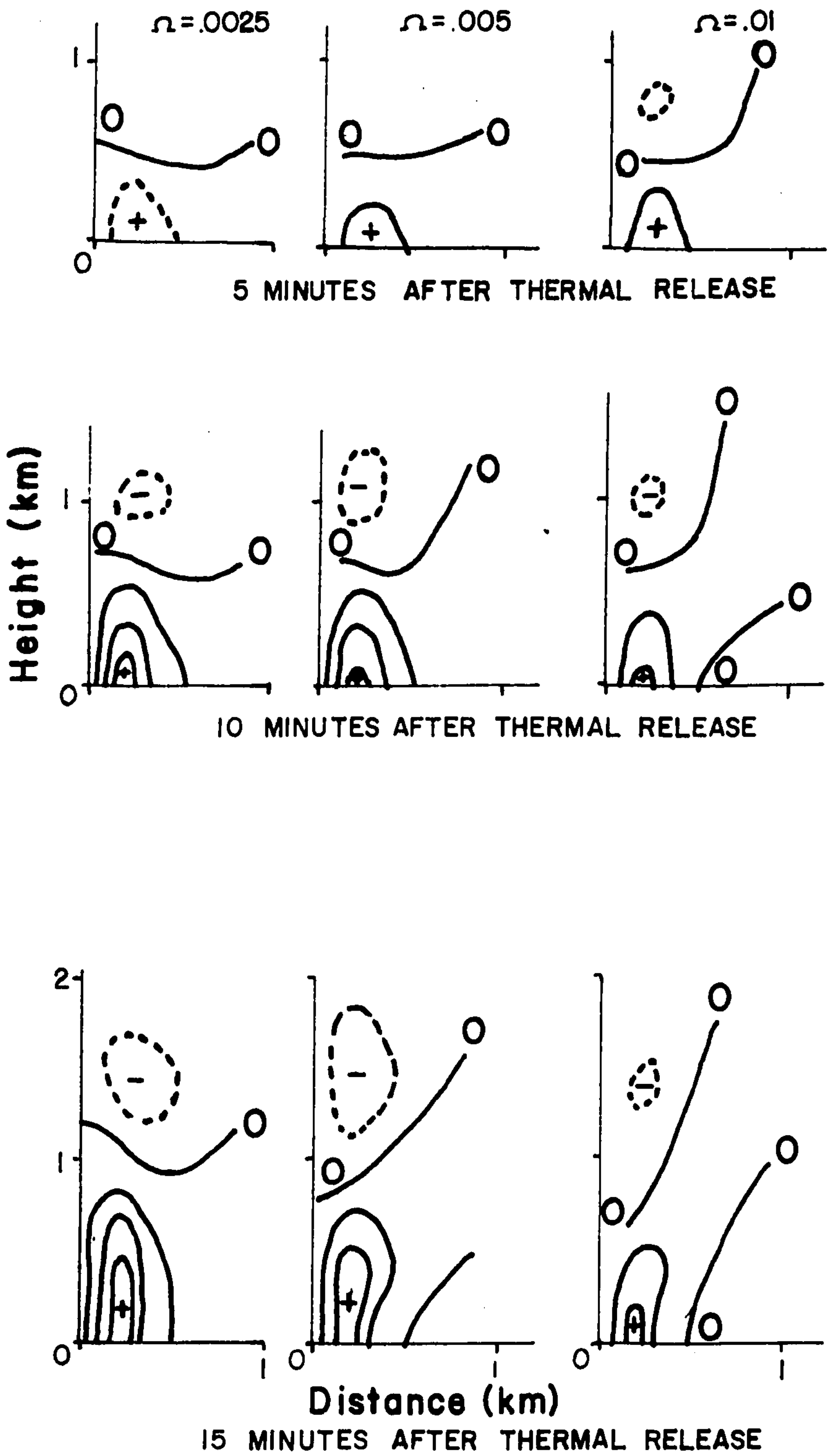

Figure 22. Tangential excess structure for adiabatic thermals. Solid contours drawn for 0, 1, 2, and 3 m sec^{-1}. Dashed contours drawn for 0.5 m sec^{-1}.

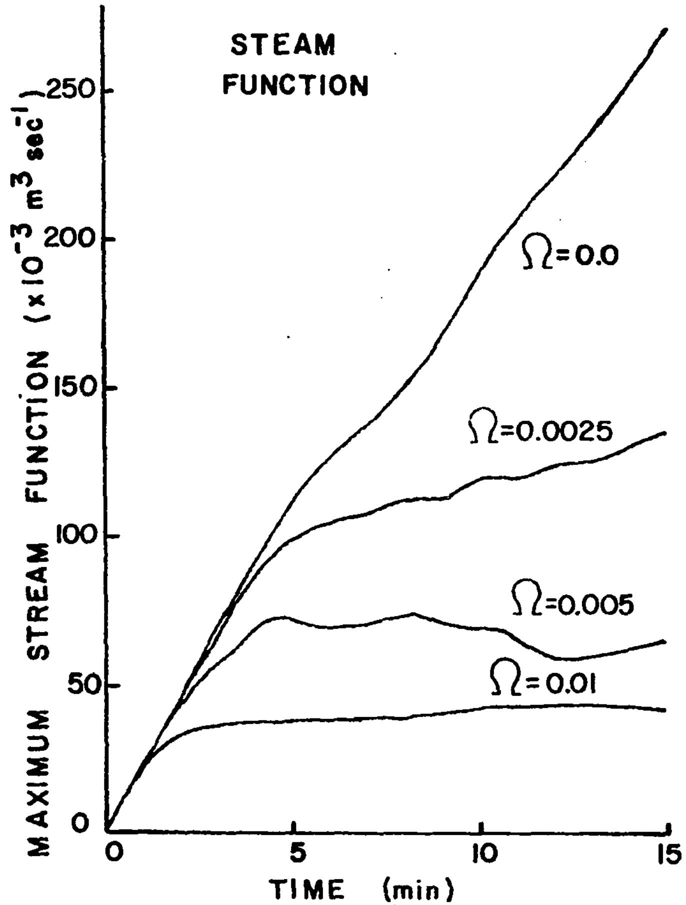

Figure 23. Maximum streamfunction for adiabatic thermals.

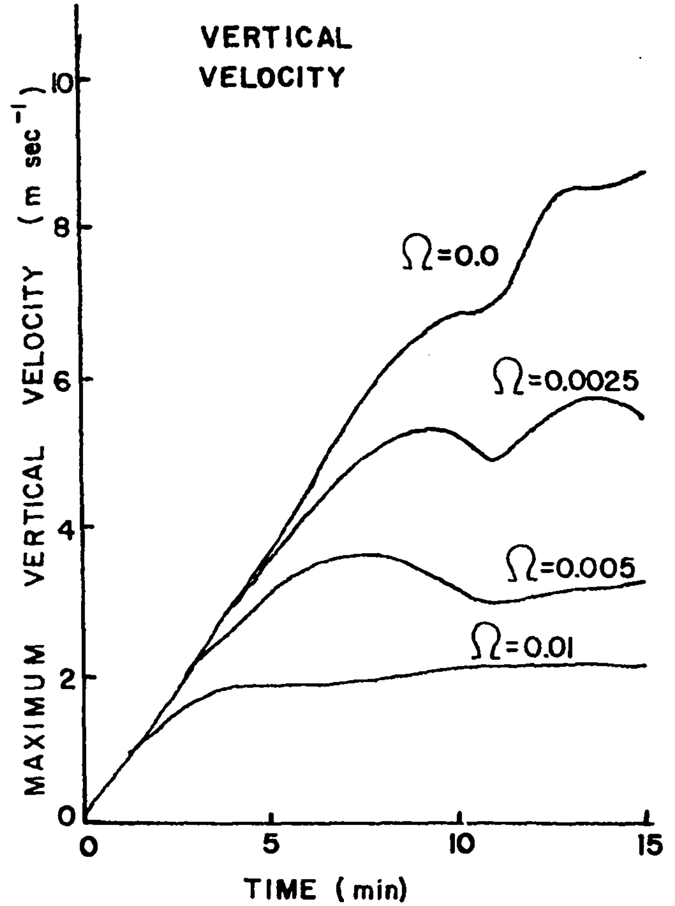

Figure 24. Maximum vertical velocity for adiabatic thermals.

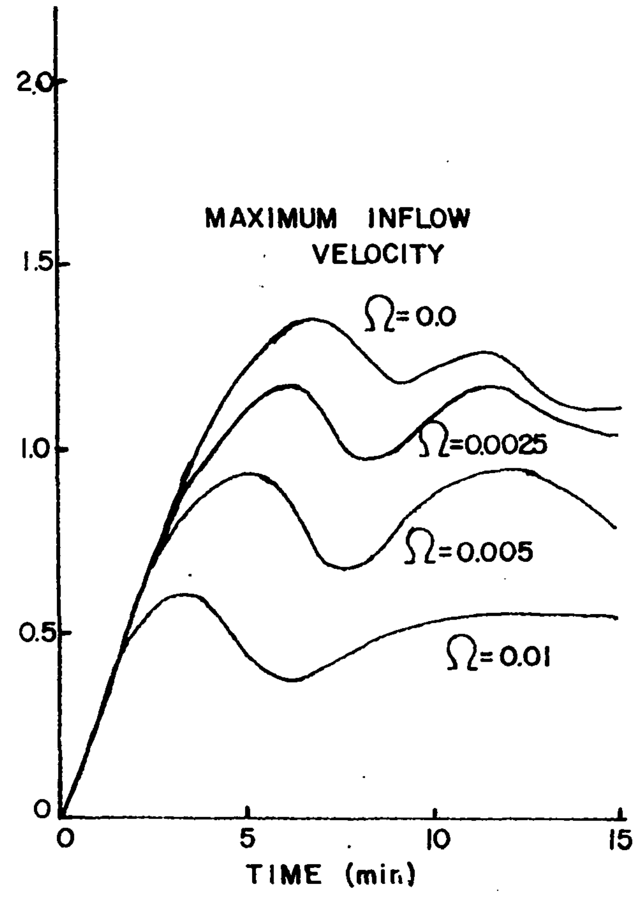

Figure 25. Maximum inflow velocity for adiabatic thermals.

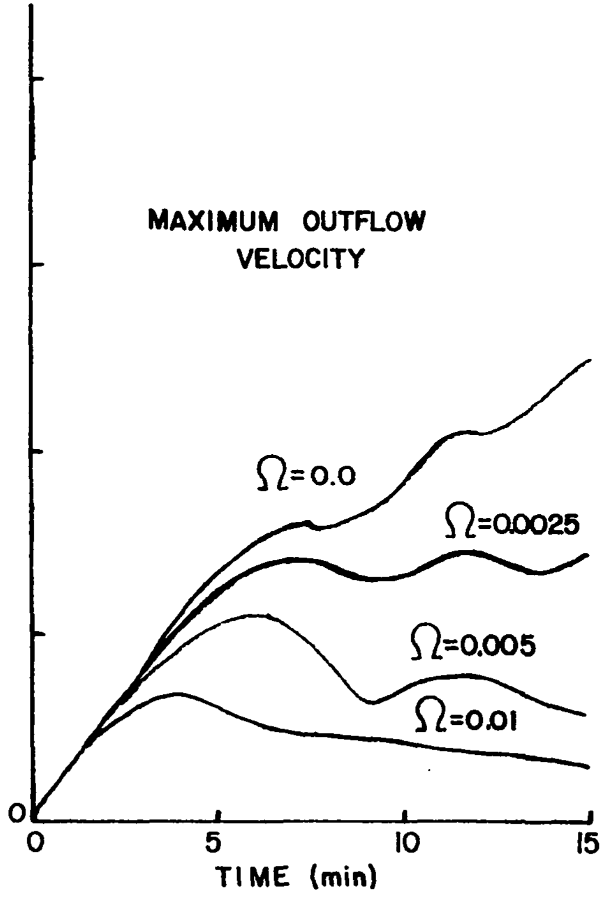

Figure 26. Maximum outflow velocity for adiabatic thermals.

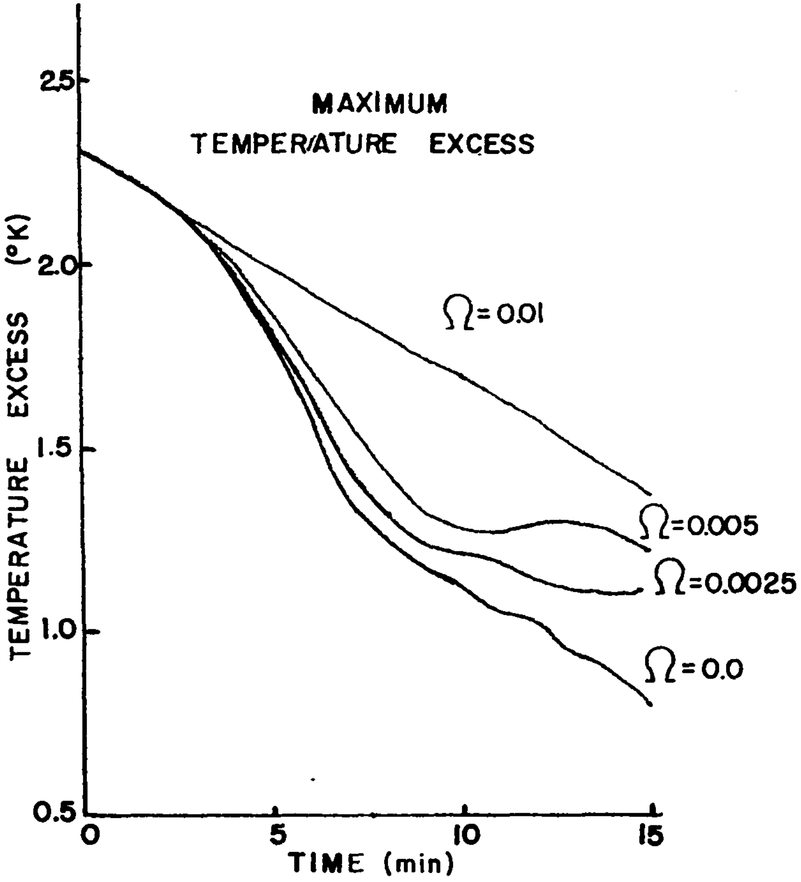

Figure 27. Maximum temperature excess for adiabatic thermals.

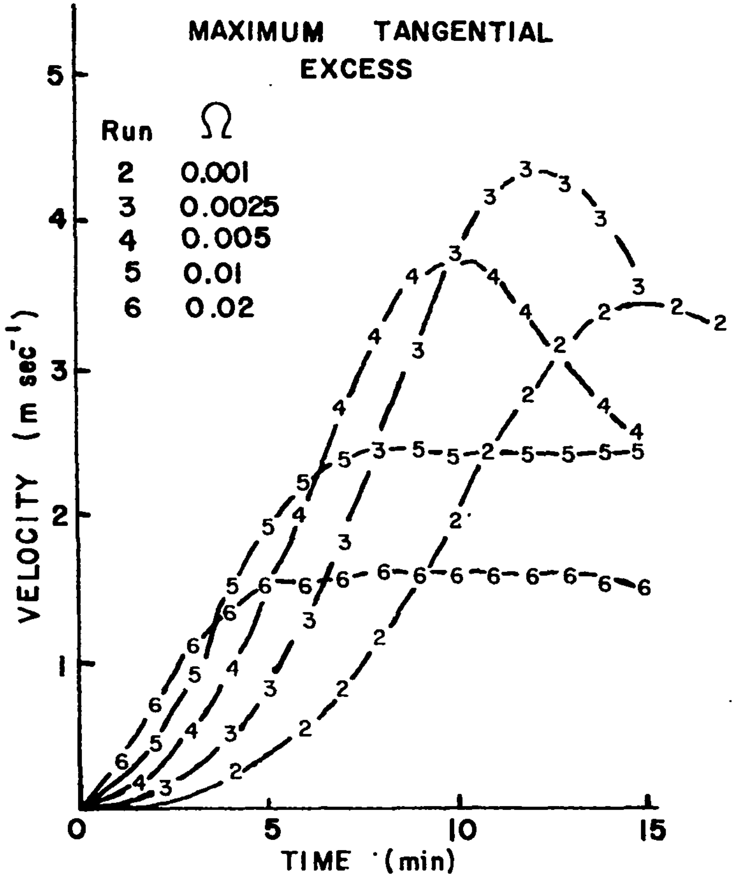

Figure 28. Maximum tangential excess for adiabatic thermals.

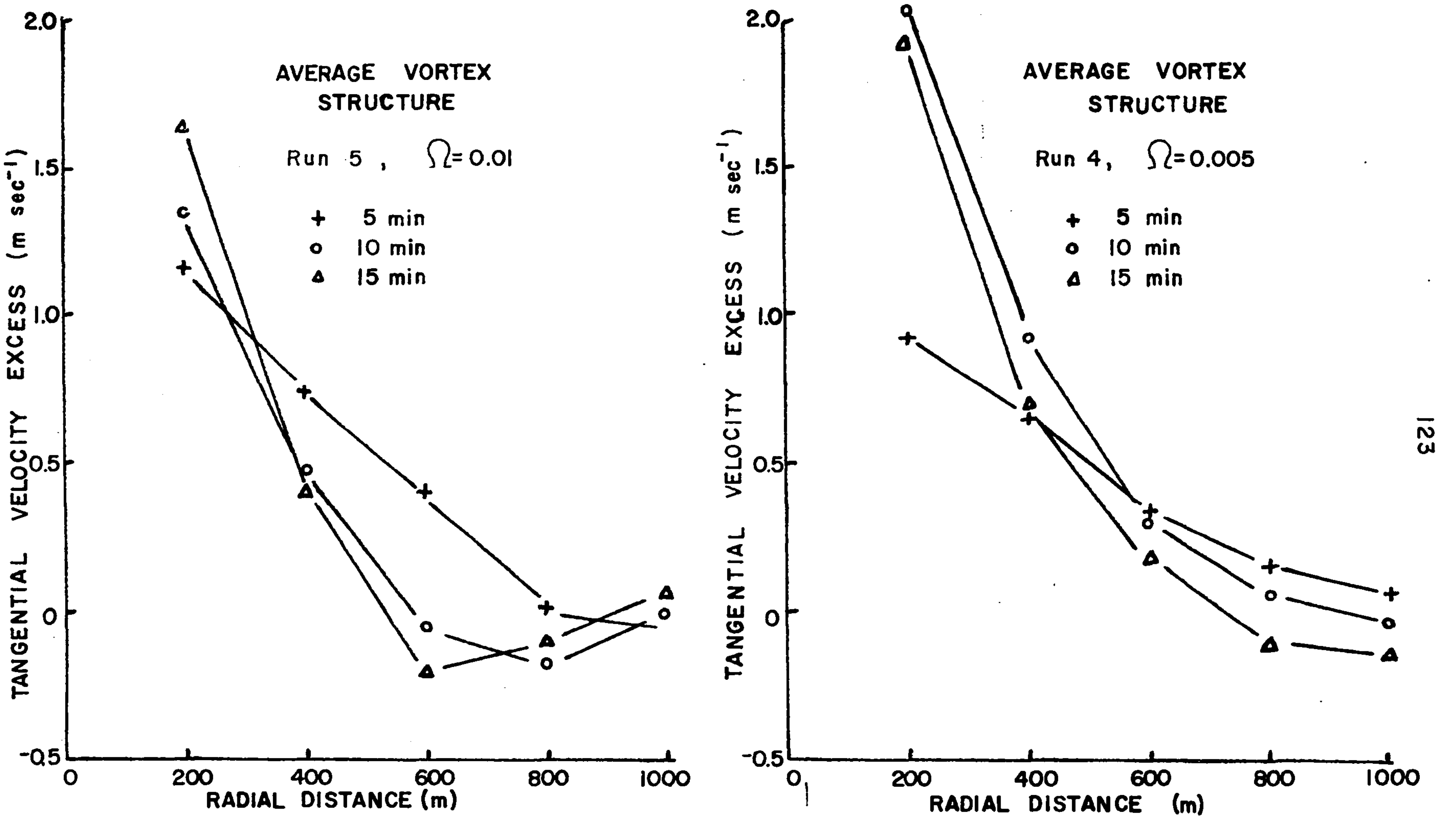

Figure 29. Structure of the vortex generated by the adiabatic thermals.

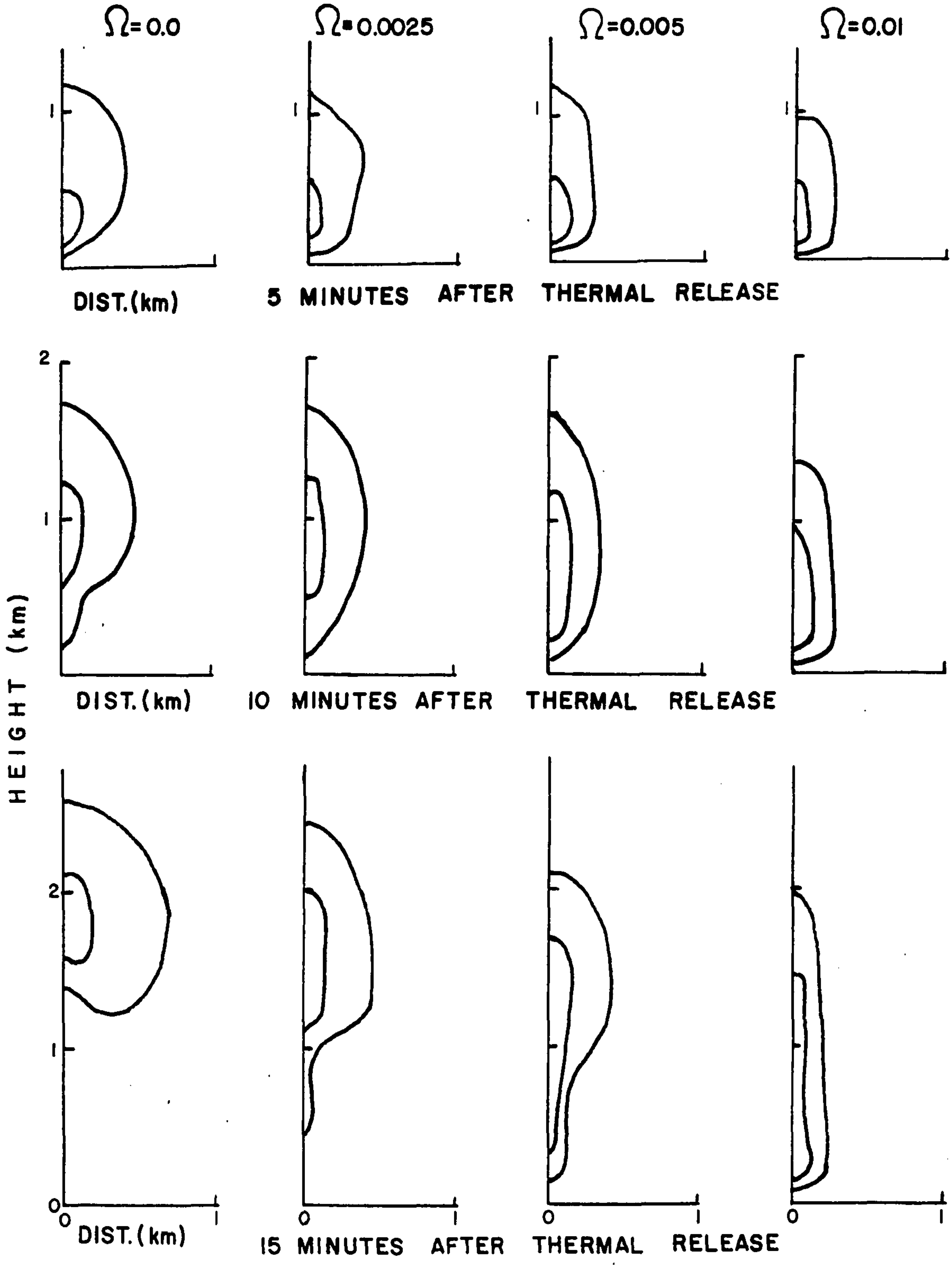

Figure 30. Temperature structure for non-adiabatic thermals, 5 percent per minute production rate. Contours drawn for 0, 2 degree excess.

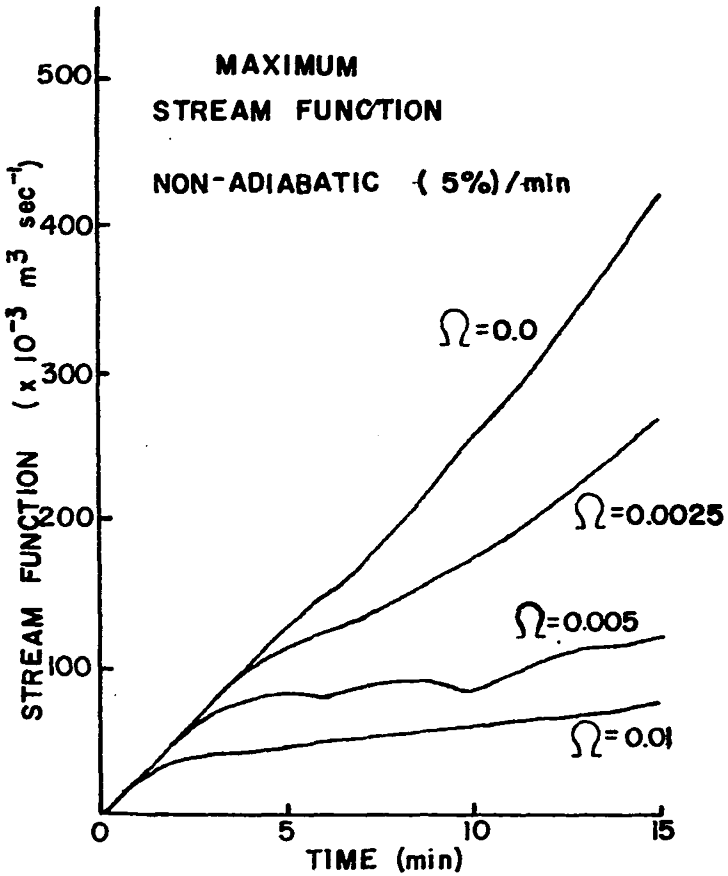

Figure 31. Maximum streamfunction for 5 percent per minute production rate.

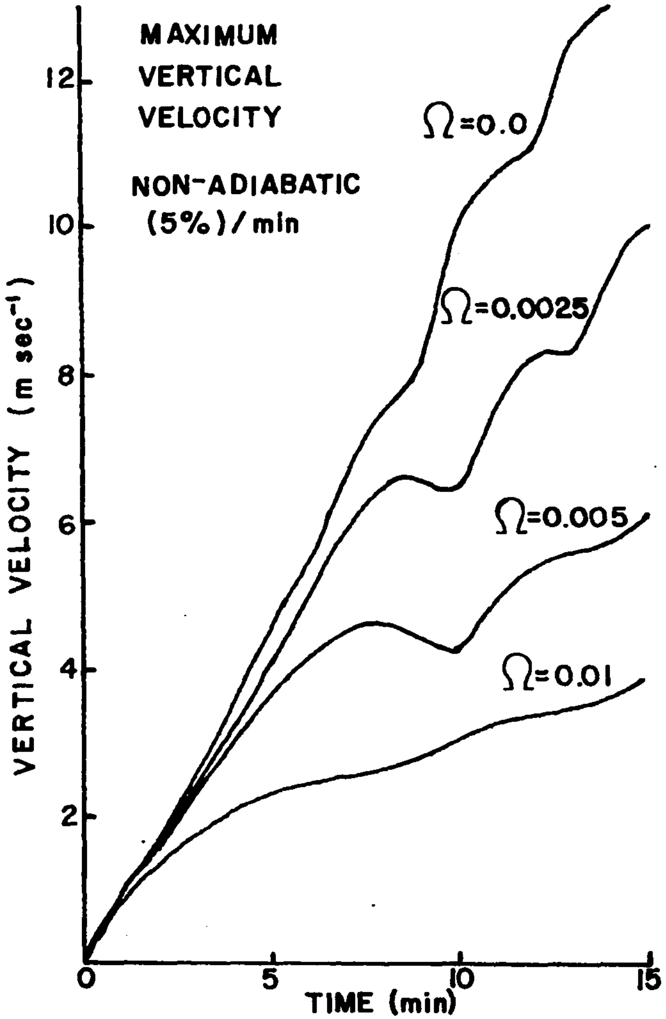

Figure 32. Maximum vertical velocities for 5 percent per minute production rate.

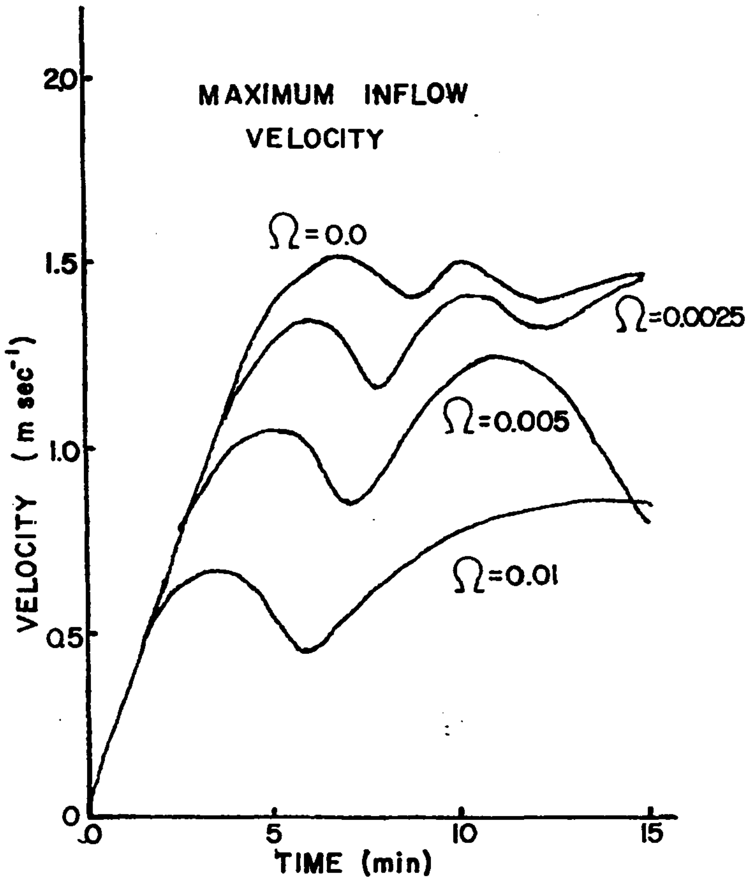

Figure 33. Maximum inflow velocity for 5 percent per minute production rate.

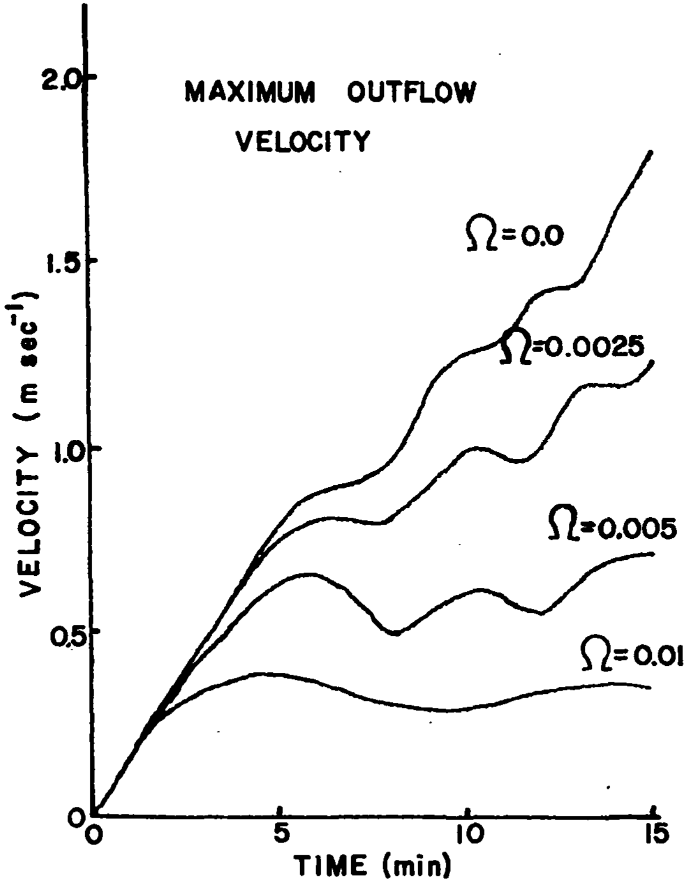

Figure 34. Maximum outflow velocity for 5 percent per minute production rate.

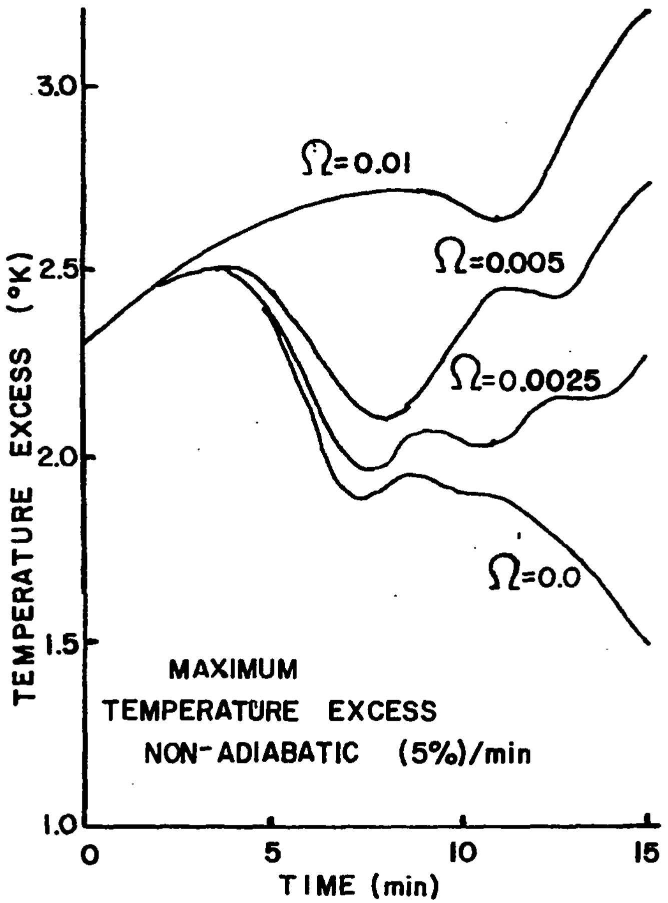

Figure 35. Maximum temperature excess for 5 percent per minute production rate.

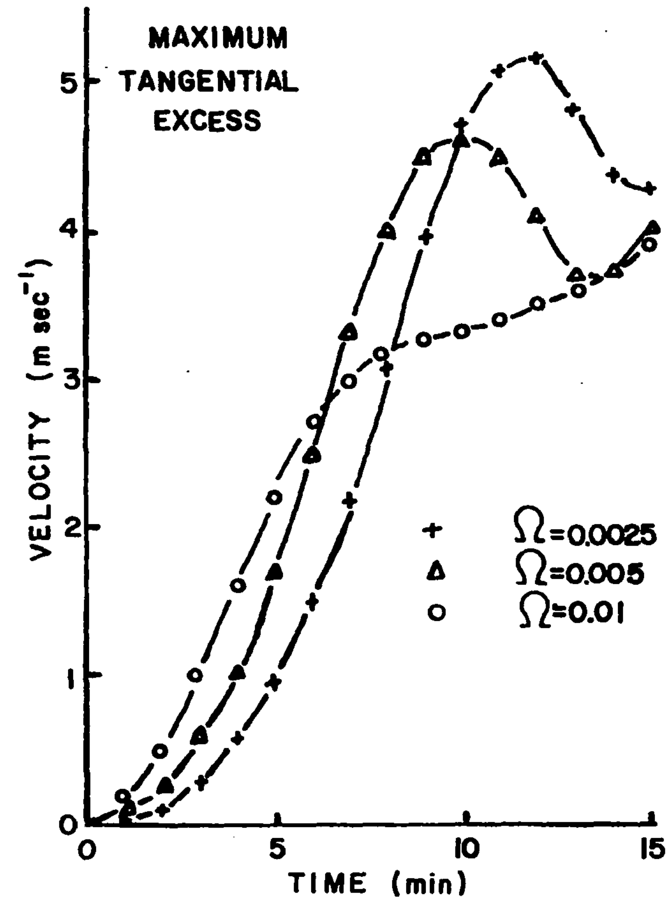

Figure 36. Maximum tangential excess for 5 percent per minute production rate.

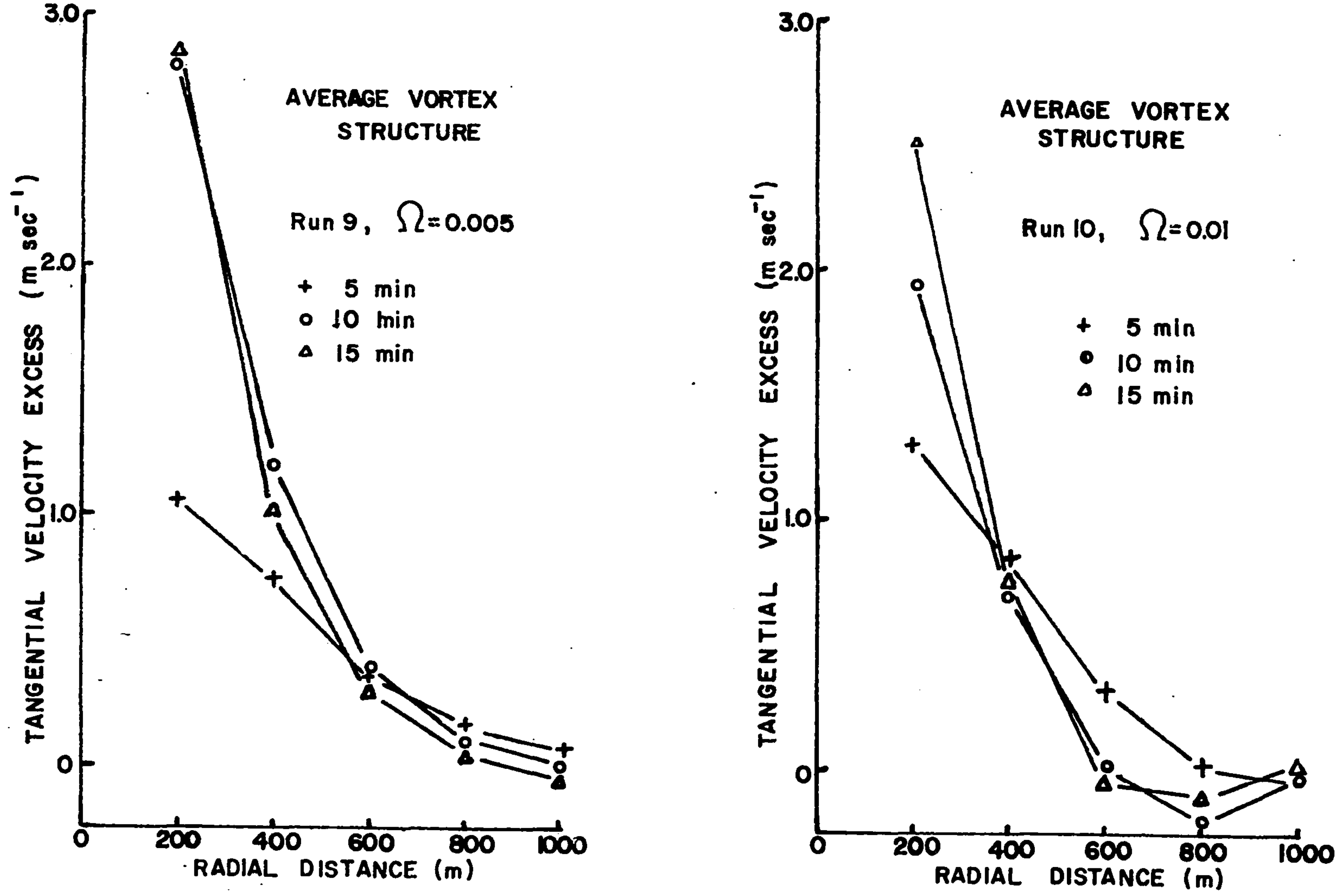

Figure 37. Vortex structure generated by 5 percent per minute production rate thermals.

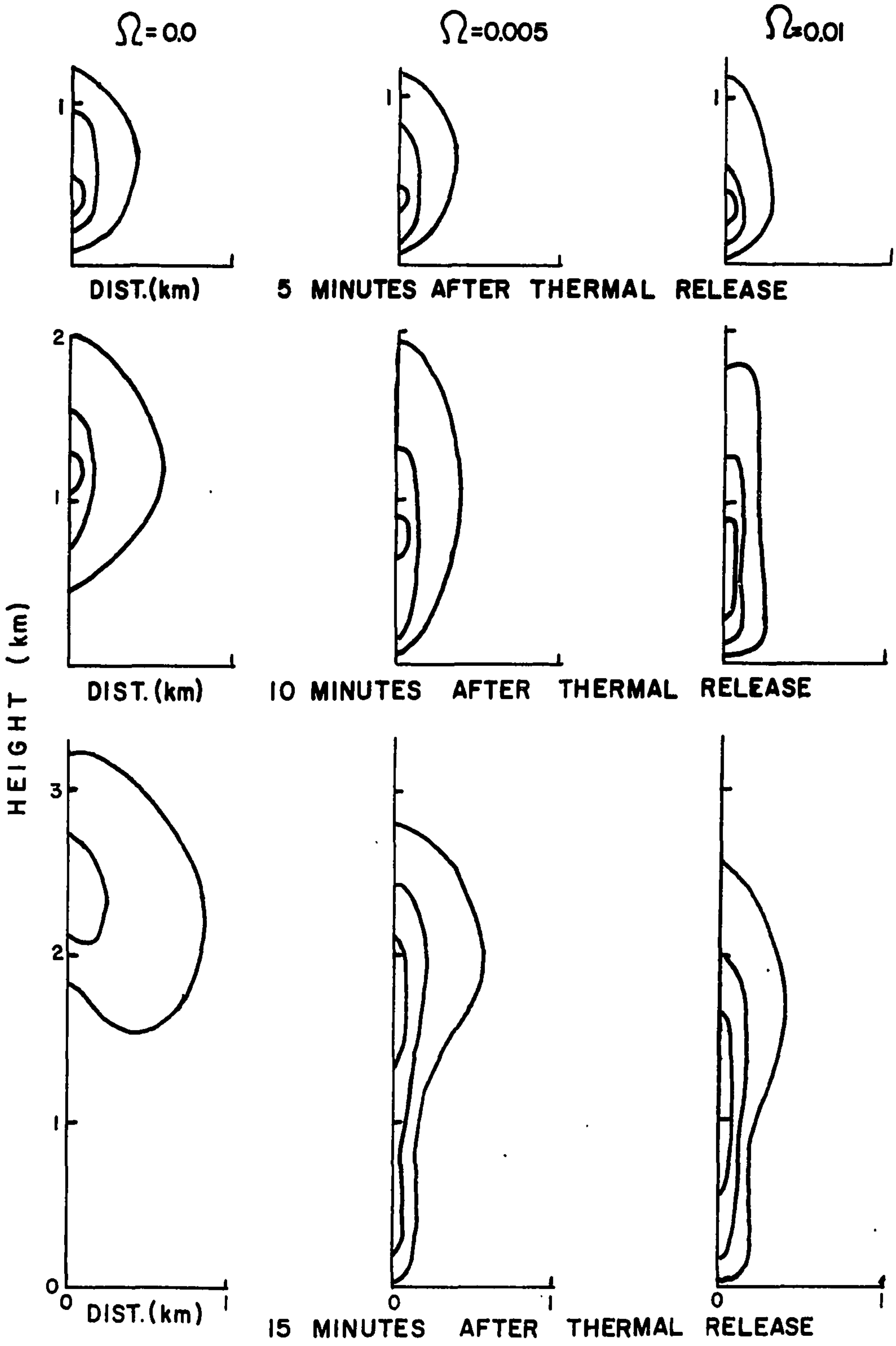

Figure 38. Temperature structure for non-adiabatic thermals, 10 percent per minute production. Contours drawn for 0°, 1°, 3° temperature excess.

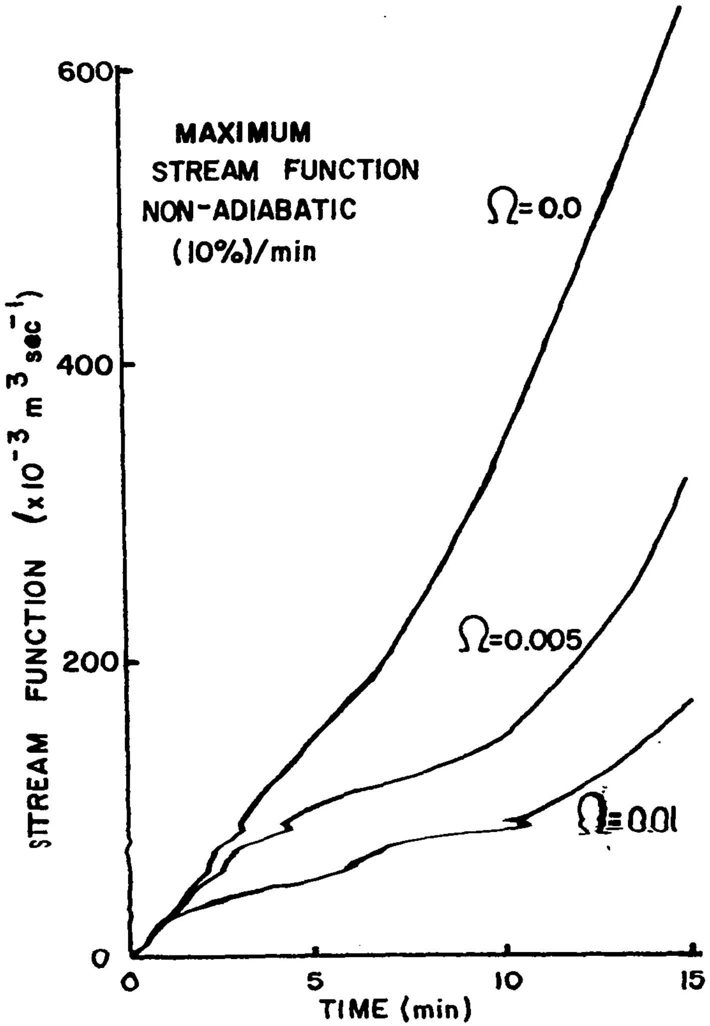

Figure 39. Maximum streamfunction for 10 percent per minute production rate.

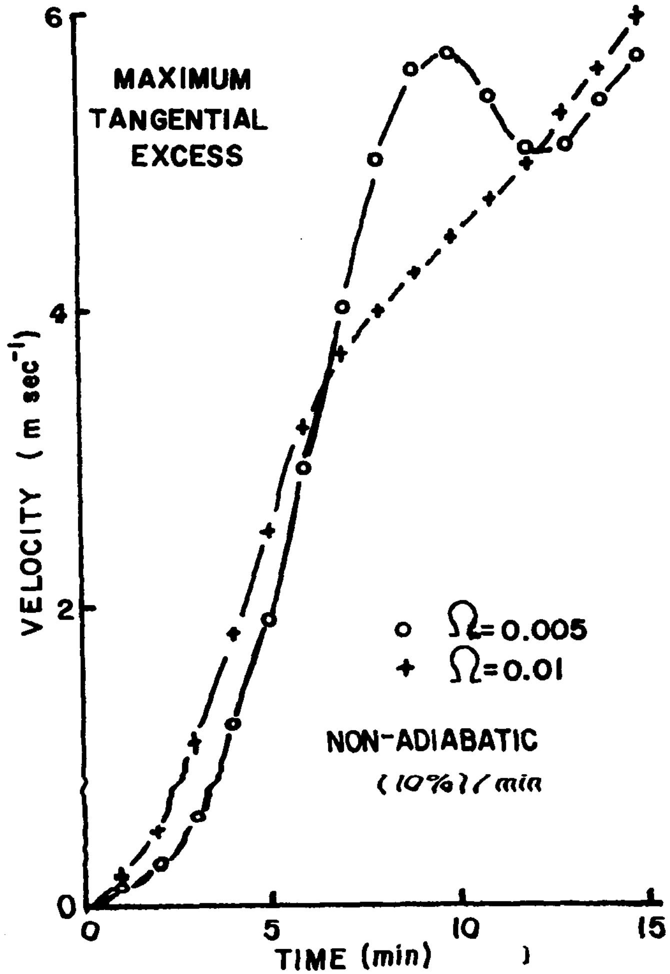

Figure 40. Maximum tangential excess for 10 percent per minute production rate.

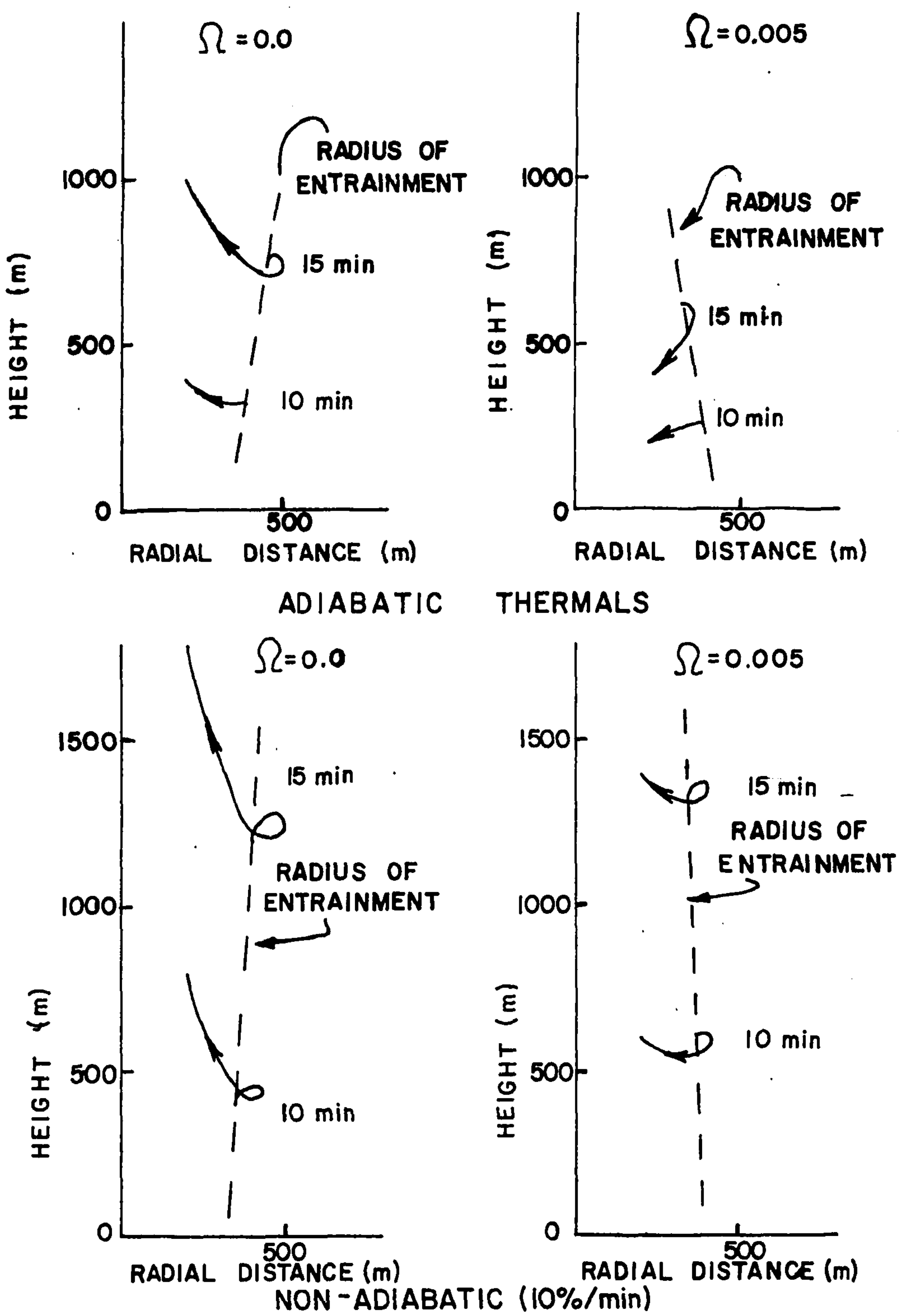

Figure 41. Radius of entrainment and trajectories of fluid particles in x-z plane within rotating and non-rotating convective elements.

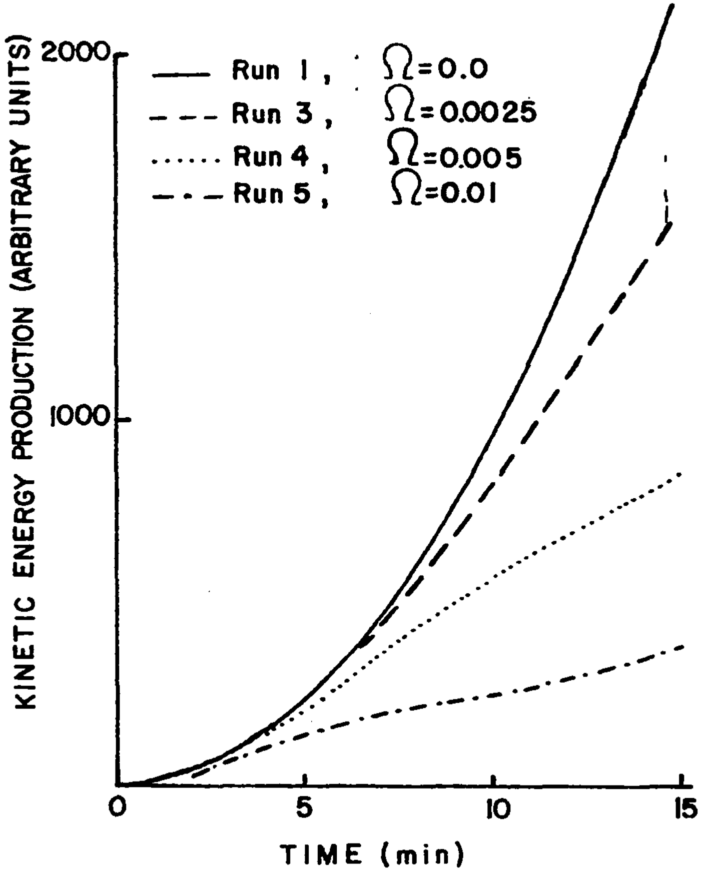

Figure 42. Potential to kinetic energy conversion for adiabatic thermals.

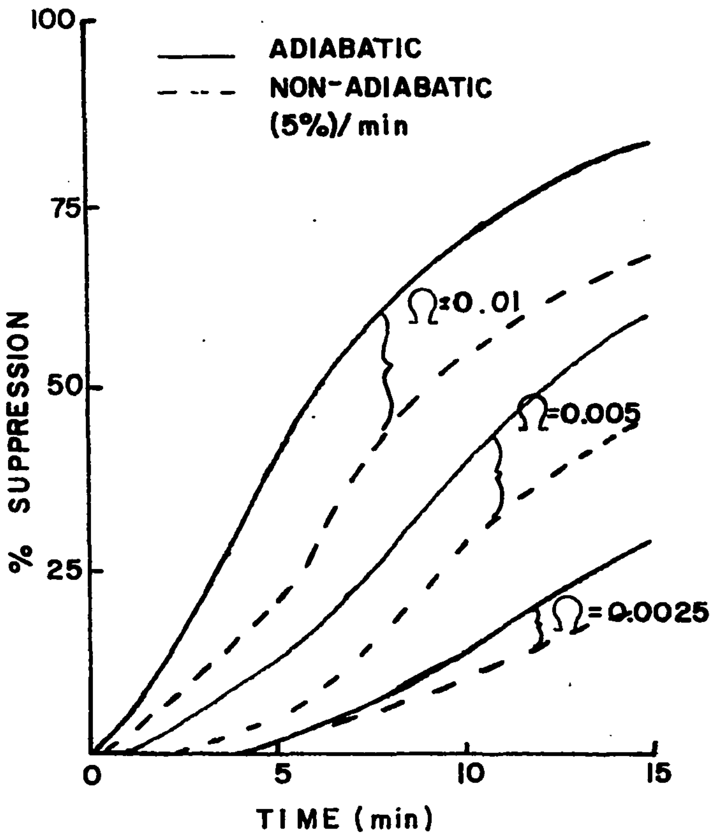

Figure 43. Suppression of kinetic energy production as a function of rotation and buoyancy production.

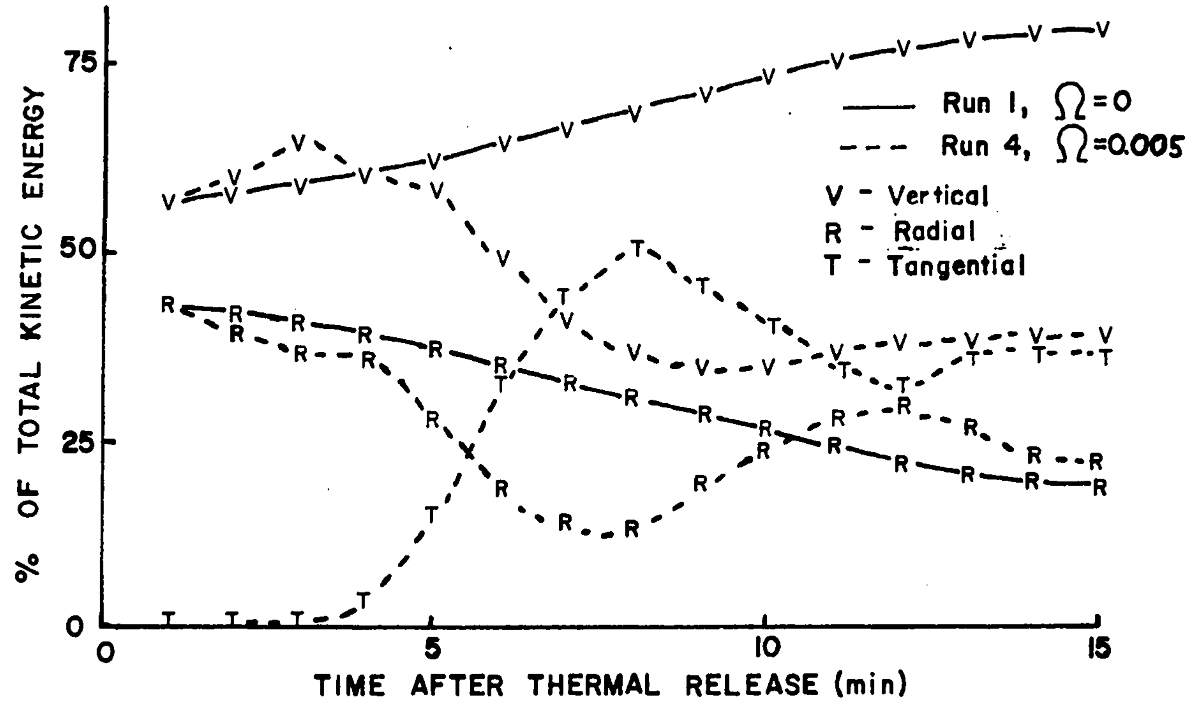

Figure 44. Energy budget for runs 1 and 4. Adiabatic thermals. Breakdown of total kinetic energy into vertical, radial and tangential component.

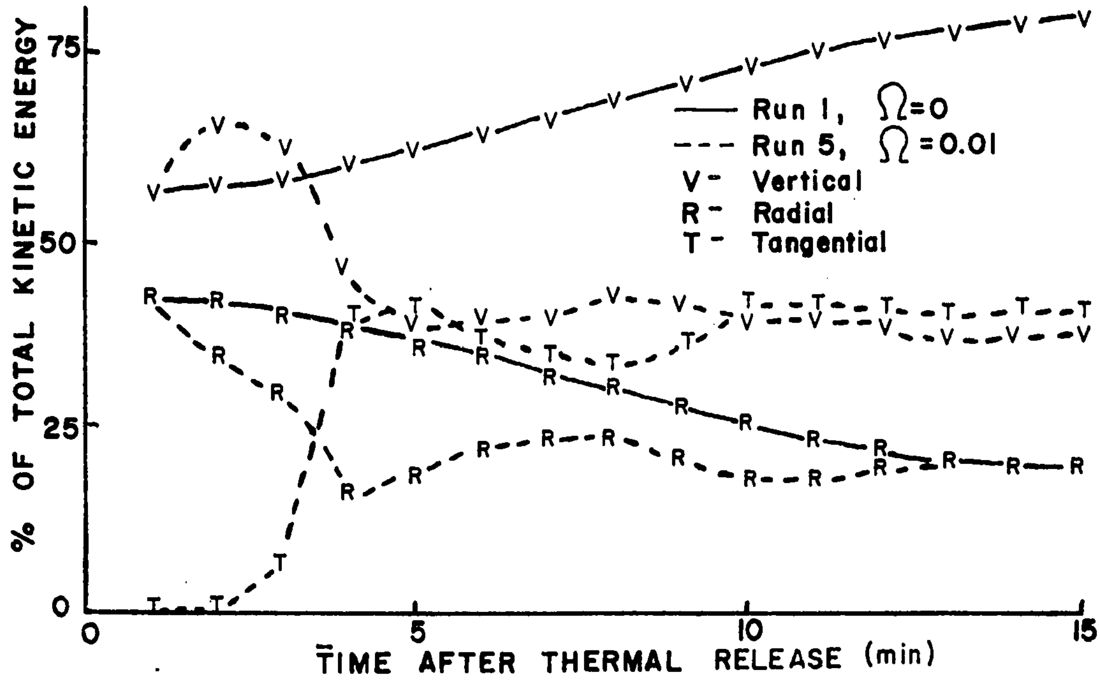

Figure 45. Same as 44 for runs 1 and 5.

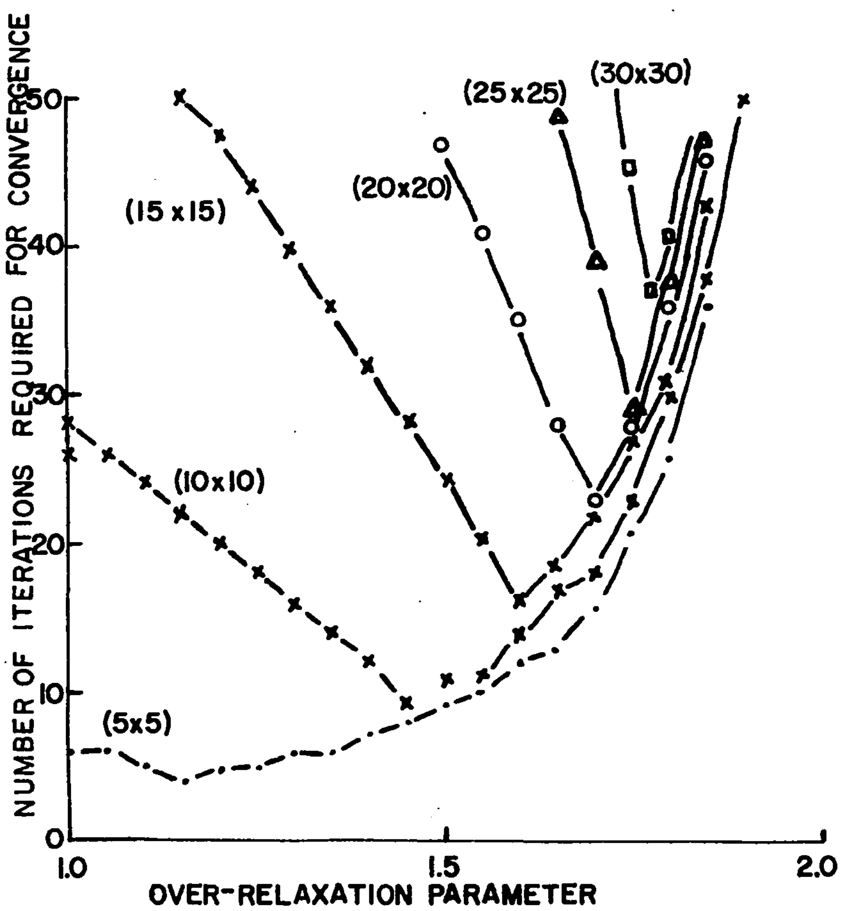

Figure 46. Number of iterations required for convergence of the vorticity equation as a function of the over-relaxation parameter.

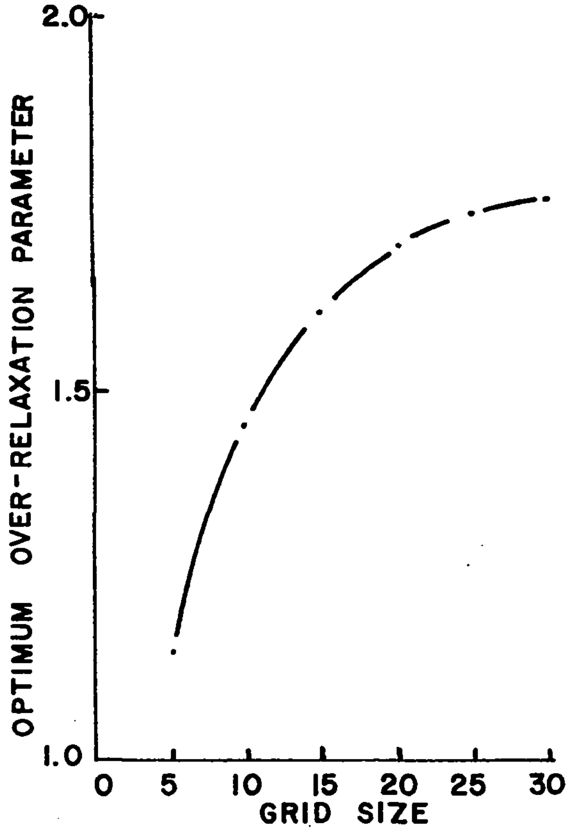

Figure 47. Optimum over-relaxation parameter for the solution of the vorticity equation on a square grid as a function of grid size.